Institute for Energy

NESC-IV PROJECT

An investigation of the transferability of Master Curve technology to shallow flaws in reactor pressure vessel applications

Final Report

NESC

Network for Evaluating Structural Components

September 2005

EUROPEAN COMMISSION
DIRECTORATE-GENERAL
Joint Research Centre
EUR 21846 EN

Mission of the Institute for Energy

The Institute for Energy provides scientific and technical support for the conception, development, implementation and monitoring of community policies related to energy.
Special emphasis is given to the security of energy supply and to sustainable and safe energy production.

European Commission
Directorate-General Joint Research Centre (DG JRC)
Institute for Energy (IE)

Contacts:
N.G. Taylor Tel.: +31 (0)224 565202
E-mail: nigel.taylor@cec.eu.int

http://ie.jrc.cec.eu.int/

Printed in the Netherlands, DG JRC, Institute for Energy, PR & Communication

NESC-IV Project
"An investigation of the transferability of Master Curve technology to shallow flaws in reactor pressure vessel applications"

Final Report, September 2005

EUR 21846 EN

Authors

N.G. Taylor, K.-F. Nilsson, P. Minnebo, European Commission Joint Research Centre, Institute for Energy, The Netherlands

B.R. Bass, W.J. McAfee, P.T. Williams, ORNL, USA

D.I. Swan, Rolls-Royce Ltd., UK

D. Siegele, Fraunhofer Institut für Werkstoffmechanik, Freiburg, Germany

Published by the

EUROPEAN COMMISSION

Directorate-General Joint Research Centre
Institute for Energy
1755 ZG Petten, The Netherlands

EXECUTIVE SUMMARY

The NESC-IV project has addressed the transferability of fracture toughness data from laboratory specimens to applications that assess the integrity of reactor pressure vessels subjected to upset and normal loading transients. The main focus was on two series of large-scale features tests:

- Six biaxial bend cruciform tests of surface-breaking semi-elliptic defects in a RPV longitudinal weld.
- Four uniaxial tests on extended sub-clad defects in RPV plate material, designed as a feasibility check for testing a simulated embedded flaw design, which if successful would be used a series of biaxial tests.

For both series the test temperatures were selected to achieve a fracture event in the brittle/ductile transition region, i.e. cleavage, but with sufficient contained yielding around the crack tip to have a constraint effect. The coordinated experimental/ analytical program drew from major elements of the biaxial features testing program conducted by the Heavy Section Steel Technology Program at the Oak Ridge National Laboratory. Extensive materials testing and fracture analyses were performed by a group of twenty European organizations, coordinated by the Network for Evaluating Structural Components (NESC). There has also been a close collaboration with the EC-sponsored VOCALIST project. The main conclusions are as follows:

- For the biaxial bend feature tests on weld material specimens containing a shallow semi-elliptical surface flaw the calculated K_{Jc} values are consistent with the standard Master Curve and no constraint loss effect is considered to have occurred; this is attributed to the out-of-plane loading.
- The embedded flaw beams produced a substantial constraint loss effect.
- The Master Curve provided an adequate description of the transition toughness under high constraint conditions for the materials used.
- While NESC-IV did not produce specific data to judge the validity of applying the Master Curve size correction long (>25 mm) crack lengths, it is noted the size-corrected assessments are in good agreement with standard test results.
- The data from shallow-flaw SE(B) specimens indicate effect of constraint loss in fracture toughness specimens can be described by a shift in $T_{o.}$
- Overall the T-stress parameter provided the most consistent representation of the constraint effects observed in both the NESC-IV test piece geometries, with the provisos that, when present, out-of-plane loading must be taken into consideration and that the T-stress variation over the full crack front needs to be checked to establish the most constrained location. The Q parameter provided reliable results for the uniaxial loaded beams.
- The application of the R6 constraint modified procedure and the Wallin T-stress model were verified for the embedded flaw beam tests. The prediction that the load carrying capacity of at temperatures in the range of T_0 is increased by over >30% is supported by the experiment results.
- Local approach Beremin models proved capable of predicting the constraint-loss effects observed in the uniaxial bend tests on embedded flaw beams and the effect of out-of-plane biaxial loading in suppressing constraint loss for the biaxial tests.

ACKNOWLEDGEMENTS

The NESC-IV feature tests were part of the Heavy Section Steel Technology (HSST) program funded by the US Nuclear Regulatory Commission (NRC). This support is gratefully acknowledged.

The project would not be possible without the contributions of organisations in the NESC network. These are (in alphabetical order):

- Bay Zoltan Foundation, Hungary
- British Energy, UK
- CEA, France
- DNV, Sweden
- EON Kernkraft, Germany
- Framatome ANP GmbH, Germany
- Fraunhofer Institut für Werkstoff-Mechanik, Germany
- KFKI, Hungary
- MPA Stuttgart, Germany
- NRI Rez, Czech Republic
- Prometey Institute, Russia
- Rolls-Royce plc, UK
- Serco Assurance, UK
- TWI Ltd., UK
- VTT, Finland

We thank the staff and management of all these organisations and look forward to further successful collaboration in NESC.

Finally, the support of the European Commission via the Joint Research Centre, Institute for Energy, which coordinates the NESC network and provides technical support to its projects, is gratefully acknowledged.

TABLE OF CONTENTS

1 INTRODUCTION

The Network for Evaluation of Structural Components (NESC) was launched in 1993 to undertake large-scale collaborative projects capable of serving as international benchmarks for validating the total structural integrity process [1, 2]. A 90-member network has been established, coordinated by the European Commission's Joint Research Centre, Petten, Netherlands, and including nuclear power plant operators, manufacturers, regulators, service companies, and R&D organizations. The NESC I and NESC II projects, involving simulations of pressurized-thermal-shock (PTS) events in nuclear reactor pressure vessels (RPVs) were completed in 2001 and 2003 respectively [3,4]. NESC-III, involving research into flaw assessment in dissimilar metal welds between piping components and NESC- Thermal Fatigue on high cycle fatigue evaluation under turbulent flow conditions, are currently ongoing. NESC-IV was formally approved at the NESC Steering Committee meeting held in Stockholm during September 2000.

The NESC IV project is a coordinated experimental/analytical program that draws from major elements of the biaxial cruciform testing program conducted by the Heavy Section Steel Technology (HSST) Program at the Oak Ridge National Laboratory, USA [5-13]. That program has focused on modelling of postulated shallow flaws in heavy-section nuclear RPVs that are subjected to realistic multi-axial loading states produced by credible upset events such as PTS transients and normal operational pressure-temperature (P-T) transients. The NESC IV project consists of two phases that are focused on fracture toughness testing and model development for both shallow surface flaws and embedded flaws. The project includes six biaxial bend cruciform tests of through-clad semi-elliptic defects in a longitudinal weld from an RPV (Part A), and four uniaxial tests of extended sub-clad defects in RPV plate material (Part B). These tests were conducted recently at ORNL as a cooperative effort between the HSST Program and NESC IV. Additional work packages conducted by the European partners of NESC-IV included extensive characterization of the RPV source material, design/fabrication of the embedded-flaw specimens, residual stress measurements, and structural/fracture mechanics analyses.

A major objective of NESC IV was to address the transferability of fracture toughness data from laboratory specimens to applications that assess the integrity of RPVs subjected to upset and normal loading transients. The "Master Curve" concept incorporated into ASTM E-1921 [14] provides standardized testing and data analysis techniques for characterizing fracture toughness of RPV steels in the ductile-to-brittle transition region. Specifically, the Master Curve provides the median fracture toughness for a 1T specimen under small-scale yielding (SSY) conditions as a function of temperature in the transition region, when a reference temperature T_o has been determined from SSY fracture toughness data. However, the deep-notch compact tension or bend specimens typically used to generate those small-scale yielding data provide a sharp contrast to crack-tip conditions potentially encountered in RPV assessments. Under PTS upset conditions, as well as normal P-T operational transients, the thermal, pressure and residual stresses in an RPV wall combine to form a complex nonlinear biaxial stress state. Included in this stress field are significant tensile out-of-plane stresses aligned parallel to postulated shallow surface or embedded flaw fronts, oriented in either the longitudinal or circumferential directions. The SSY fracture toughness data do not reflect the actual biaxial loading state, nor generally the constraint conditions and the flaw front lengths associated with postulated RPV flaws. The cruciform experiments performed within NESC IV were intended to challenge applications of Master Curve procedures to predict the behavior of shallow flaws in RPV clad materials subjected to biaxial loading conditions in the transition region.

In 2003 the project team produced an interim report [15], which described in detail the planning of the work, the materials characterisation programme, the fabrication of the test pieces, the pre-text fracture analyses and the results of the tests themselves. The present Final Report covers the post-test analyses and overall evaluation of the results. It describes in detail the major aachievements, which include:

- experimentally validated analysis methods needed to characterize fracture behavior in the lower-transition temperature region of shallow surface and embedded flaws located in RPV material and subjected to biaxial loading conditions;
- a material properties database, including appropriate test techniques and data-analysis methods, needed to experimentally validate the above analysis methods; and
- benchmark results that can be used to promote best practice and harmonization of international standards regarding the treatment of shallow flaws in RPV structural integrity assessments.

Finally, it is noted that NESC-IV was conducted in parallel with the VOCALIST (Validation of Constraint Based Methodology in Structural Integrity) project [16]. VOCALIST was a shared cost action project co-financed by the European Commission under the Fifth Framework of the European Atomic Energy Community. Its objective to develop validated models of the constraint effect and associated best practice advice was closely linked to that of NESC-IV and there was intense collaboration between the groups.

2 THE NESC-IV PROJECT

2.1 Background: the HSST Biaxial Testing Program

The fracture toughness of shallow surface flaws subjected to biaxial far-field stresses represents an active area of research in the field of structural integrity safety assessments of nuclear RPVs. In the lower-transition temperature region, uniaxial shallow-flaw fracture toughness data for RPV steels exhibit higher mean values and broader scatter bands than are measured for deep flaws under the same loading conditions. That increase in mean fracture toughness has been attributed to a loss of crack-tip constraint due to the close proximity of the crack tip to a free surface of the test specimen. Any increase in crack-tip constraint, for example due to out-of-plane near-surface biaxial stresses, could partially offset this observed trend of shallow-flaw fracture toughness enhancement.

Under pressurized-thermal-shock (PTS) conditions, as well as normal pressure-temperature (P-T) operational transients, the thermal, pressure, and residual stresses in an RPV wall are all biaxial (see Figure 2.1) and combine to form a complex nonlinear biaxial state of stress. Included in this stress field are significant tensile out-of-plane stresses aligned parallel to possible surface or embedded flaws oriented in either the longitudinal or circumferential directions. Standardized fracture toughness testing procedures typically employ specimens such as compact tension, C(T), or single-edge notched bend, SE(B), specimens, that are loaded under a uniaxial state of stress (either tension or bending). Therefore, the resulting fracture toughness data do not reflect the actual biaxial loading state that the postulated RPV flaw will be subjected to in a PTS or P-T transient.

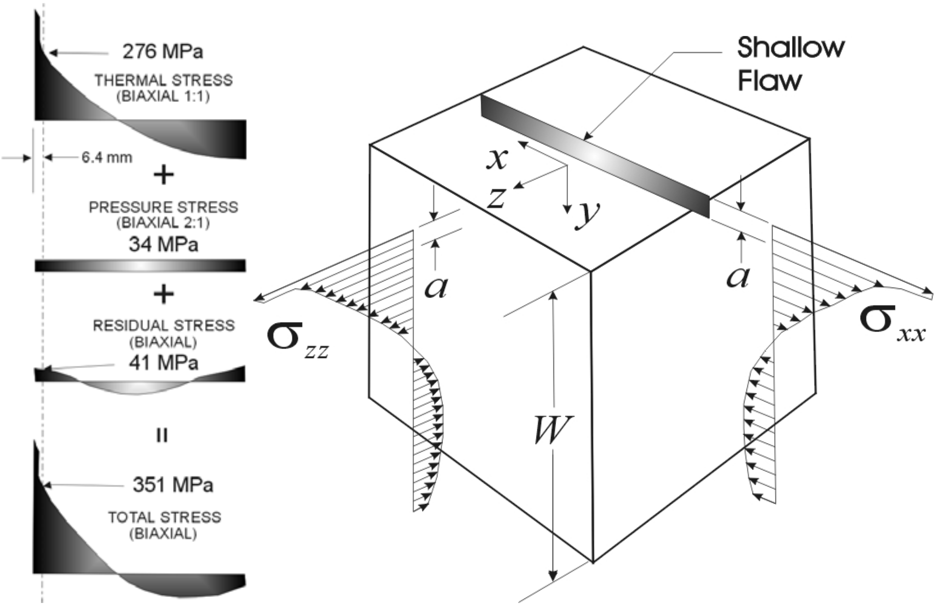

Figure 2.1: PTS loading produces a nonlinear biaxial stress state in a pressure vessel wall: (a) typical contributions of thermal, pressure, and residual stresses and (b) the total complex state of stress applied to a shallow surface flaw.

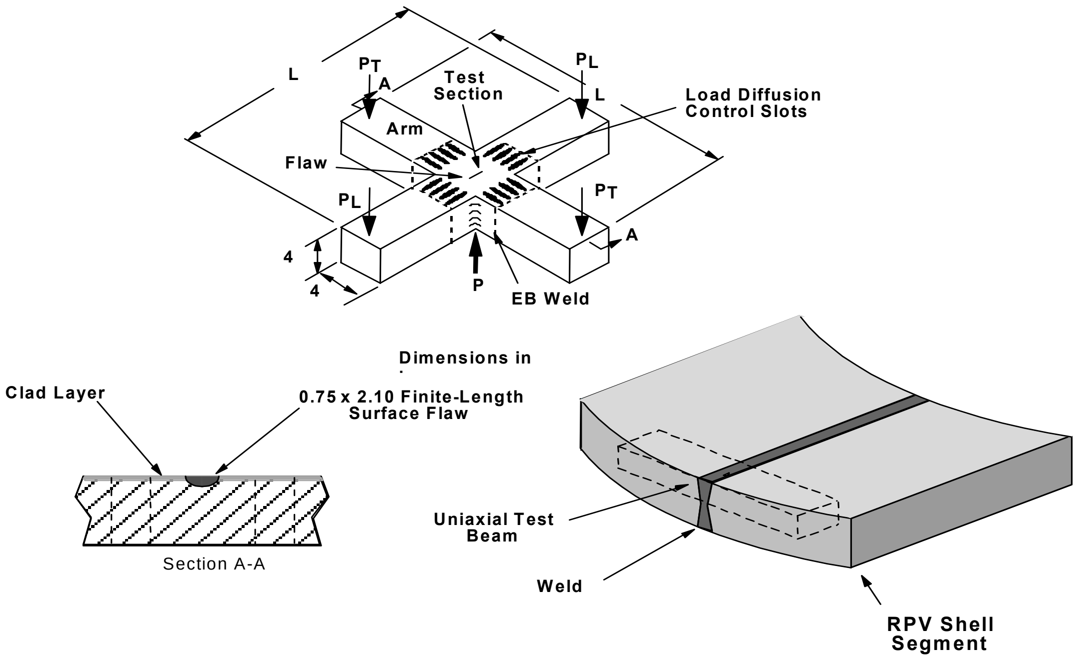

Figure 2.2: Cruciform test pieces with simulated planar flaws are cut from an RPV shell segment to investigate initiation behavior of RPV welds.

A special cruciform bend specimen (Figure 2.2) was developed by the HSST Program at ORNL to introduce a linear, far-field, out-of-plane biaxial bending stress component in the test section that approximates the nonlinear stresses of PTS or P-T loading. The cruciform specimen permits the application of biaxial loading ratios resulting in controlled variations of crack-tip constraint for shallow surface flaws. The biaxial load ratio is defined as P_T / P_L, where P_T is the load applied to the transverse beam arms and P_L is the load applied to the longitudinal arms. A special test fixture was also designed and fabricated permitting testing under a uniaxial (4-point bending) loading, P_T / P_L ratio of (0:1), and two biaxial (8-point bending) loading ratios, P_T / P_L ratios of (0.6:1) and (1:1). The specimen and test fixture have been described extensively in publications [5-13]. Extensive test data has been reported for several RPV steels, including A533 B plate (HSST-14 plate and submerged-arc welds with A 533 B Class 1 filler metal.

In parallel ORNL have also developed a local approach fracture mechanics methodology based on a three-parameter Weibull model to correlate the experimentally observed biaxial effects on fracture toughness [17, 18]. The Weibull model, combined with a hydrostatic stress criterion in place of the more commonly used maximum principal stress in the kernel of the Weibull stress integral definition, has been shown to provide a scaling mechanism between uniaxial and biaxial loading states for 2-D (i.e., straight) surface flaws located in an A533 B plate. More recently, the *Weibull stress density* was employed in the Weibull cleavage fracture model as a metric for identifying regions along a semi-elliptical (3-D) flaw front that have a higher probability of cleavage initiation [17,18].

Figure 2.3: PVRUF reactor vessel that provided source material for the NESC IV testing program.

2.2 NESC IV Work Programme

The NESC-IV project work programme [19] was released in 2001 and foresaw two distinct parts, A and B, that are focused on fracture toughness testing and model development for shallow surface flaws and for embedded flaws, respectively. The steel selected for the project was sourced from RPV shell segments from a pressurized-water RPV that was never in service; in the following it is referred to as the PV-RUF vessel (Fig. 2.3)

2.2.1 Part A: Clad Cruciform Biaxial Testing – Semi-elliptic Surface Flaw

In this part of the project it was foreseen to test a series of six clad cruciform specimens containing shallow semi-ellipitical surface flaws. The specimens were fabricated by ORNL from the PVRUF longitudinal welds (Fig. 2.2), using the same design as that employed previously in the HSST program, i.e., the intermediate-scale specimen with a test-section thickness of 102 mm (4 in.). During fatigue pre-cracking, the initial machined flaw was extended an additional 1.3 mm (0.050 in.) along the full length of the flaw. The final dimensions of the flaw were, nominally, 53.3 mm (2.10 in.) long and 19.1 mm (0.75 in.) deep.

2.2.2 Part B: Embedded Flaw Testing

An understanding and quantification of the fracture toughness associated with embedded flaws is important in the further refinement of RPV integrity assessment procedures. It has been shown that fracture toughness of RPV materials is a function of flaw tip constraint. Deeper flaws have higher constraint than shallow flaws with a resultant lower median toughness and smaller scatter (deep-flaw behavior compared to shallow-flaw behavior). Applying multiaxial loading to shallow-flaws increases constraint and tends to reduce median toughness and scatter for shallow flaws, although the reduction in median fracture toughness does not necessarily eliminate all of the shallow-flaw effect. It is hypothesized (and has been supported by preliminary analyses), that small, embedded flaws will exhibit a higher median fracture toughness than comparable-sized surface flaws even under multiaxial loading.

The objective of Part B was therefore to evaluate fracture toughness in the lower transition region associated with small, embedded flaws. The intent was to develop and validate a viable fracture toughness specimen for use in the study of embedded flaws, and to execute a test matrix to obtain a limited amount of embedded flaw toughness data. The test program therefore concentrated on uniaxial (configuration and loading) beam bend specimens using A533 B steel with a stainless steel clad overlay (Fig. 2.4). That material was removed from the same shell as the clad cruciform specimens. For the embedded flaw development, use of the clad A533 B base material simplifies metallurgical considerations as well as preserving for future use the very limited amount of RPV weld material. Technology was developed for fabricating embedded flaws into the test sections. A total of four uniaxial specimens containing embedded flaws were planned for the program to demonstrate that a viable fracture toughness specimen had been achieved. The target temperature for the testing program was the lower transition temperature range for the selected material.

The general fabrication sequence proposed for the embedded flaws followed the experience gained in fabricating the clad cruciform specimens. The fabrication procedure involved machining of the test section to final dimensions, and then using a wire EDM technique to machine the embedded flaw from the sides of the test section. The major advantage of this procedure is that the flaw tip can be located anywhere through the specimen thickness without metallurgically altering the material between the flaw tip and the clad surface. Also, the approach provided control of the thickness of the remaining ligament over the flaw.

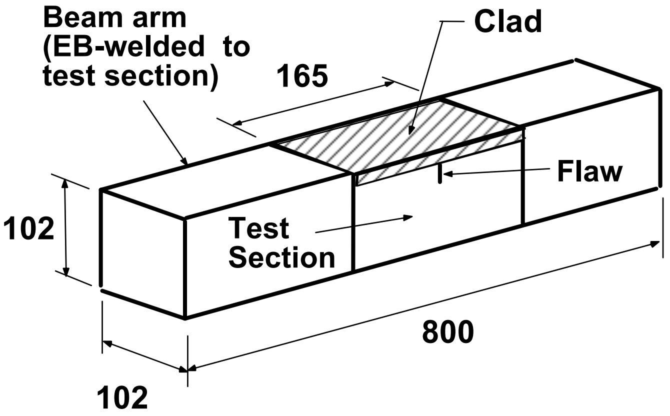

Figure 2.4: Schematic of the uniaxial bend beam test piece with a through thickness slot to simulate an embedded flaw.

2.2.3 Materials Characterisation Requirements

The RPV material is an A533 B pressure vessel steel with a single-layer stainless-steel strip-clad (4 in.-wide and ~5 mm thick) overlay on the inner surface. The longitudinal weld geometry is of the *double-J* configuration requiring that the weld be essentially symmetric about the mid-plane of the vessel wall. The welds were submerged-arc welds (SAWs) with A533 B Class 1 filler metal. The plate material[1], clad overlay, and weldment are typical of a production-quality RPV. The shell had a nominal inner radius of 2210 mm (87 in.) and a thickness of 232 mm (9.125 in), which includes the ~5 mm clad overlay.

---

[1] Records obtained from the fabricator of the RPV indicate that the vendor for the vessel plate material was Marrel Freres, France.

For the planned stress and fracture mechanics analyses an extensive range of material characterization tests was required. These included:

a) tensile tests
b) Charpy impact tests
c) Pellini drop-weight tests
d) Fracture toughness tests on both deep and shallow notched specimens to calibrate the Master Curve

Furthermore, a range of material zones on the RPV shell had to be considered:

a) the longitudinal weld
b) the clad-overlay
c) the plate
d) the heat-affected zone on the plate under the clad

2.2.4 Stress and Fracture Analysis Requirements

Analysis requirements included the following:

- analytical support for selection of test temperatures
- computational modeling and simulation of the experiments to gain insight into the physical processes involved;
- development and experimental validation of analysis methods needed to characterize fracture behavior in the lower transition region of shallow surface flaws in RPV material subjected to multiaxial loading conditions.

Due to the complexity of the geometry and loading conditions, detailed multi-dimensional structural models of the test specimens were planned. It was anticipated that the influence of constraint on fracture toughness will also need to be addressed with analytical models that are responsive to the complete state of stress near the flaw tip. Under both uniaxial and multiaxial loading conditions, stress and strain fields will vary along the crack tip producing a positional dependence for the resulting applied stress intensity factors (or J-integrals) that must be investigated. The influence of property variations resulting from the presence of material interfaces (both sharp and diffuse) such as the HAZ/base interface and the clad/HAZ interface had to be considered.

2.3 Project Organization

The work was organized following the NESC Task Group scheme:

Task Group 1 – Non-Destructive Testing
This aspect was not considered in the NESC-IV project.

Task Group 2 - Materials Characterization
TG2 arranged for the execution and evaluation of the materials characterization tests foreseen in the work program as well as additional testing decided in collaboration with the TG3 group. For these tests appropriate PVRUF segments were sent from ORNL to the JRC who saw-cut these into the appropriate sub-blocks and distributed them to designated TG2 participants.

Task Group 3 Stress and Fracture Analysis
TG3 performed extensive pre-test and post-test analyses. The pre-tests analyses were essentially focused on determining appropriate test conditions, in particular selection of

the test temperature. The post-test analyses addressed the main objectives of the project itself.

Task Group 4 Large-Scale Tests
As Test Manager, ORNL took overall responsibility for the test piece fabrication and for the bend beam tests. For the embedded flaw test pieces the JRC contributed to the fabrication of the specimens by machining the test blocks, inserting the simulated defects and arranging for the extension arms to be welded on. Together ORNL and JRC were also responsible for preparation of the work program and for pre-test and post-test problem definition documents, which provided a basis for the TG3 analyses.

Task Group 5 Evaluation
An *ad hoc* group comprising representatives of the Test Manager (ORNL) the Operating Agent (JRC) and the Chairmen of the TG2 and TG3 Task Groups performed this task.

Task Group 6 Residual Stresses
For NESC-IV this activity was limited to measurement of the residual stress in the weld beneath the cladding. Framatome ANP GmbH performed this task.

As the network operating agent, the JRC provided the overall coordination of the project work (in addition to its technical contributions in several areas). This included organization of meetings, preparation of minutes and preparation and distribution of reports. The progress of the project was reported to the regular six-monthly meetings of the NESC Steering Committee, who are also charged with approving all documents released by the network. The main milestones in the execution of the project were listed in Table 2.1.

The project documentation including minutes of meetings, test results, analyses and the main reports are stored in the NESC archive and are available electronically via the JRC's DOMA site: http://odin.jrc.nl/ne. A NESC-IV CD has also been prepared for the project participants, which contains a complete record of all documents and datasheets.

Table 2.1: Milestones in the NESC-IV Project

Date		Action
2000	September	NESC Steering Committee approves the NESC-IV project
	October	Project work program released; materials testing and pre-test fracture analyses begin
2001	March	Pre-Test Problem Definition Document [20] released
	April	2nd Project Meeting, Lyon, France
	May	PVRUF materials database version 1 (Charpy data)
	July	PVRUF materials database versions 2 & 3 released
		3rd Project meeting, Oak Ridge, USA
	Aug – Sept.	Biaxial tests on beams with surface breaking flaws
	October	PVRUF materials database version 3 released
	Oct. - Nov.	Uniaxial tests on beams with an embedded defect
	November	4th Project Meeting, Schiphol, The Netherlands
2002	February	PVRUF materials database version 5 released
	April	5th Project Meeting, Warrington, UK
	June	NESC-IV Interim Report published
		PVRUF materials database version 6 released
	July	Post-test problem definition [21] document released
		PVP conference paper on the NESC-IV test results
	November	6th Project Meeting, Erlangen, Germany
2003	May	7th Project Meeting, Stuttgart, Germany
	June	PVRUF materials database version 6 released
2004	January	8th Progress Meeting, Lymm, UK
	July	PVP conference paper on the biaxial tests on beams with a surface breaking flaw
	August	Collation of NESC-IV Post-test analyses
	September	PVRUF materials database version 7 released
	November	Vocalist-NESC Seminar “Transferability of Fracture Toughness Data for Integrity Assessment of Ferritic Steel Components”, Petten, The Netherlands
	December	Fabrication of 2nd series of embedded flaw beams completed
2005	April	Draft Final Report
	September	NESC-IV Final Report

3 MATERIALS CHARACTERIZATION

3.1 PVRUF Plate, Weld and Clad Materials

The PVRUF RPV consists of an A533 B pressure vessel steel with a single-layer stainless steel strip-clad overlay (100 mm wide and ~5 mm thick) on the inner surface. The longitudinal welds present in the vessel are of the double-J configuration with the weld root located at approximately 1/3 of the wall thickness, starting from the inner surface. They are submerged-arc welds (SAWs) with A533 B Class 1 filler metal. The shell has a nominal inner radius of 2210 mm and a thickness of 232 mm (including the clad overlay).

The vessel wall in an RPV is a composite of several materials. Some of these, such as the A533 B plate, are relatively homogeneous, although e.g. quench rate effects could result in through-wall variations of material properties. Others, such as welds or heat-affected zone (HAZ) regions tend to be highly inhomogeneous on a local scale. In characterising these materials, specific regions that may dominate flaw behaviour must be considered. The different materials to be characterised included the following:

- A533 B plate,
- longitudinal weld,
- clad overlay,
- clad/plate HAZ, and
- clad/weld HAZ.

A total of 5 beam segments from the PVRUF vessel were used, both for the first series of large-scale benchmark experiments as for the related materials test programme. The beam segment n^o 1 shown in Figure 3.1 is a circumferential cut from the inside surface of the RPV shell, and has the clad layer intact. Beam n^o 2 is similar to segment n^o 1. The beam n^o 3 segment presented in Figure 3.2 corresponds to the outside part of the RPV wall. This is also the case for segments n^o 4 and 5. With the exception of the material lost by saw cutting, the complete shell thickness is represented. Initially it was assumed that the plate material present in the segments at either side of the weld was comparable in composition and mechanical properties. However checks on Charpy properties performed as part of the test programme (see section 3.4 below) indicated some difference in fracture toughness. On the other hand room temperature tensile properties were found to be similar. For clarity the plates at either side of the weld were designated separately as Plate 100 and Plate 200. The majority of the specimens used in the testing programme were from Plate 100, whereas the large-scale test blocks were fabricated from Plate 200 material.

For a second series of large-scale tests, an additional part of PVRUF was made available. A limited materials test programme addressing the plate metal included in this block revealed Charpy and room temperature tensile properties that were comparable to those of Plate 200.

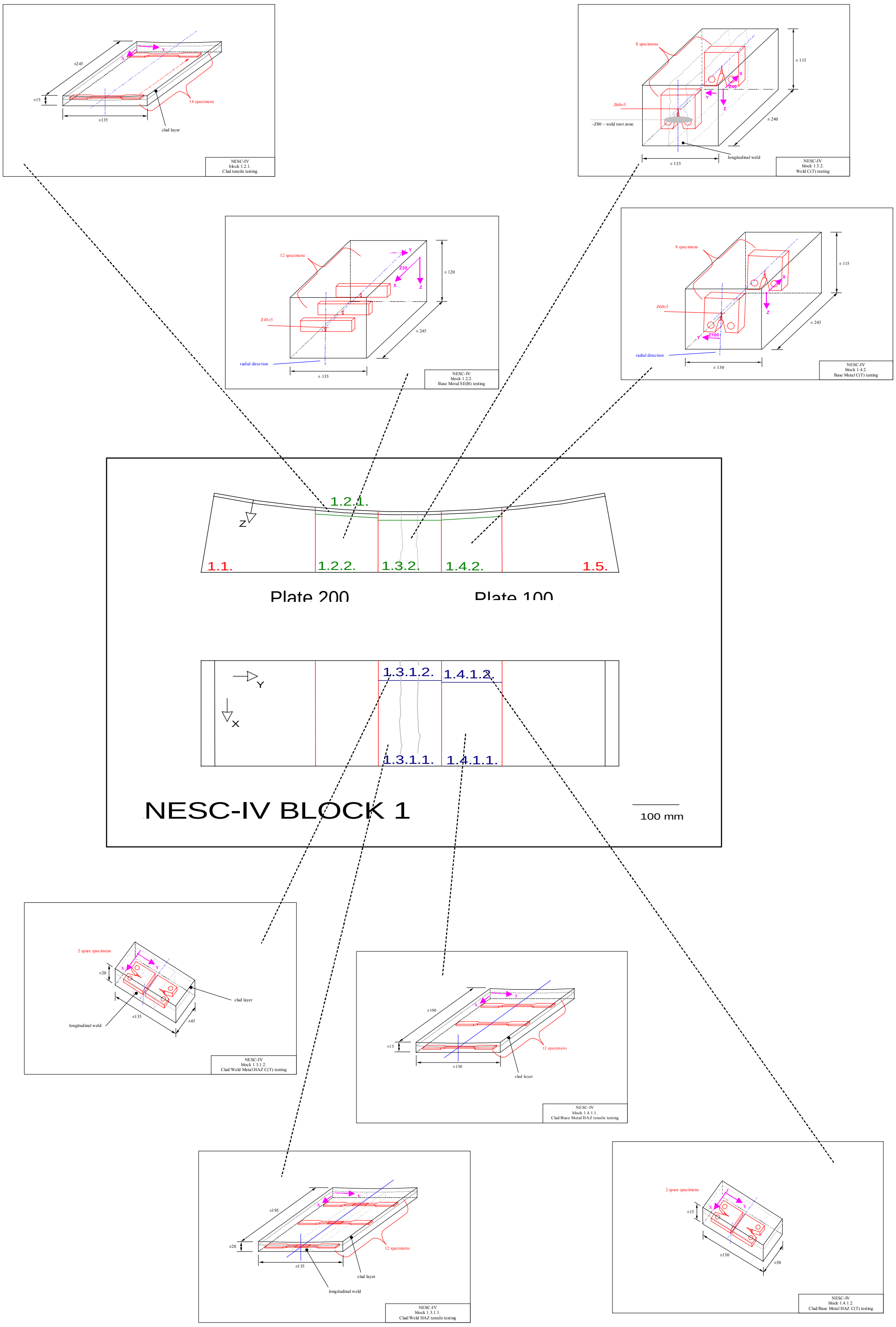

Figure. 3.1: Sampling plans for beam 1 from the PVRUF vessel supplied to the NESC-IV project (beam from the inner side of the vessel wall).

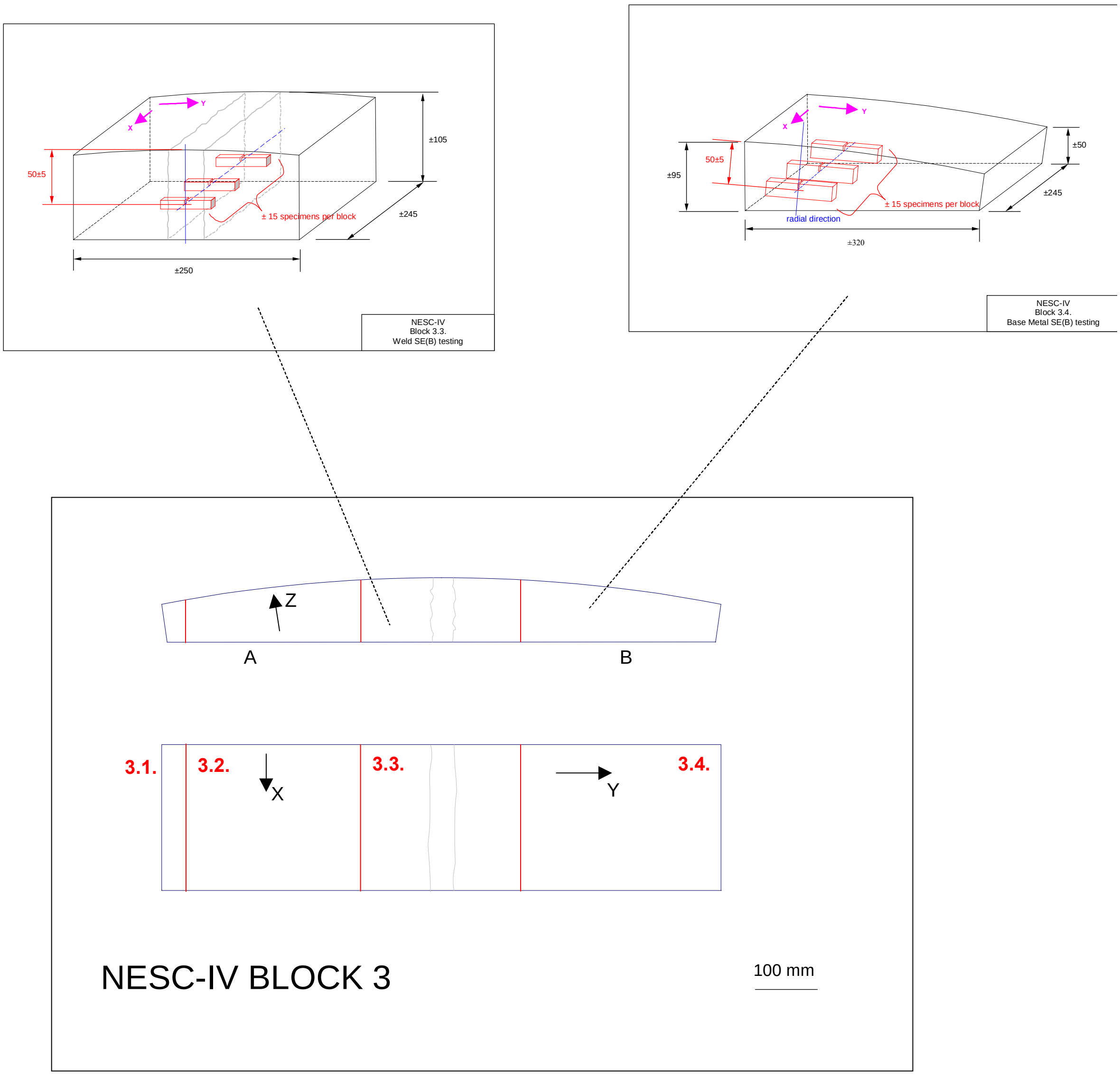

Figure 3.2: Sampling plan for beam 3 from the PV-RUF vessel supplied to the NESC –IV project (beam from the outer part of the vessel wall).

3.2 Testing Programme

The Materials Characterization Task Group (TG2) devised a detailed programme of testing in accordance with the rationale detailed in the Work Programme Document [19]. Tensile, Charpy, drop weight, single-edge notched bend (SE(B)) and compact tension (C(T)) tests were planned. A group of ten NESC-IV participants carried out this programme, for the most part thanks to contribution-in-kind, i.e. un-funded work. These organizations were:

Table 3.1: Test matrix for the PVRUF material, indicating the number of tests to be performed and the designated organizations.

Material ⇨ Test Type⇩	A533B Plate 100	A533B Plate 200	Clad Overlay	Weld	Clad/Plate HAZ	Clad/Weld HAZ
Tensile	5+1 AEKI+JRC	3+2 IWM+JRC	5+4 AEKI+IWM	5 JRC	10 FRAM	10 FRAM
Charpy Impact	18+18 BZF+JRC	35 JRC	-	18 JRC	-	-
Drop Weight	8 ORNL	8 ORNL	-	8 ORNL	-	-
SE(B) Deep Flaw	13+8 NRI+TWI	12 NRI	-	10 VTT	-	-
SE(B) Shallow Flaw	39 NRI	-	-	24 VTT	-	-
C(T)	8 IWM	-	-	8+7 IWM+ORNL	-	-

- Joint Research Centre of the European Commission (JRC),
- Rolls-Royce plc,
- Bay Zoltán Foundation for Applied Research (BZF),
- KFKI Atomic Energy Research Institute (AEKI),
- Nuclear Research Institute Řež plc (NRI),
- Fraunhofer Institut für Werkstoffmechanik (IWM),
- Framatome ANP GmbH (FRAM),
- Oak Ridge National Laboratory (ORNL),
- The Welding Institute (TWI),
- VTT Industrial Systems (VTT).

The activities encompassed programme co-ordination, experimental work and data analyses. Generally JRC saw-cut the test material segments into the appropriate sub-blocks (consistent with the TG2 characterization plan) and distributed them to the designated NESC partners who, in turn, fabricated and tested the specimens. A summary of the required characterization tests is shown in Table 3.1, indicating the type and amount of experiments, as well as the responsible organizations.

The testing results were reported centrally to the TG2 chairmanship of David I. Swan (Rolls-Royce) and Philip Minnebo (JRC), who compiled and analysed the data in spreadsheet format [22]. This database, which was updated on a regular basis, is available in electronic form to all participants of the NESC-IV project. Basically three files are provided:

- Explanatory notes, comments and references,
- Main database, comprising 25 sheets and containing all the material properties information and the large majority of the associated analyses, and
- Associated spreadsheet, containing information relating to constraint analyses of some of the toughness data.

Provision of these files fulfils one of the major objectives of the NESC IV project, i.e. the development of a material properties database, including appropriate testing techniques and data analysis methods, needed in the validation of the experimental and analytical methods used in the project.

3.3 Material and Mechanical Properties Data

3.3.1 Chemical Analyses

The weld metal composition was checked at two locations by ORNL (see Table 3.2) and found to be virtually identical.

3.3.2 Young's Modulus and Poisson Ratio

In the absence of specific Young's Modulus values covering a range of temperatures, an expression due to Oldfield [24] has been used for the ferritic plate material. Regarding the stainless steel clad the Young's Modulus data were based on the measurements made in the NESC-I project [1], where a similar filler metal and cladding process were used. Concerning the weld metal, the measured E values have been fitted. Poisson Ratio was assumed to be independent of temperature. The resulting relations for the plate, weld and clad materials are indicated in Table 3.3 below.

3.3.3 Tensile Tests

The scope of the tensile testing was to provide yield and tensile strength data as well as the full stress-strain curves for the various materials as input to the finite element fracture models. The following work has been undertaken:

- AEKI performed tensile tests on standard cylindrical specimens machined from Plate 100 and on flat section specimens machined from the clad.
- IWM carried out experiments on the Plate 200 material and partially repeated the cladding tests.
- JRC performed a series of tensile tests on round specimens machined from the weld. Further, JRC carried out room temperature experiments on the various plate materials, checking for possible differences in tensile properties. No significant variations were evident.
- Framatome ANP GmbH executed test series on flat section specimens machined from the clad heat affected zones in the weld and plate material.

All specimens were taken out in the circumferential direction. The temperature ranges covered by the tensile experiments are summarised in Table 3.4. The temperature dependence of the yield strength and the ultimate tensile strength values are shown for the plate, HAZ, weld and clad materials in Figures 3.3 to 3.6 respectivelyThe fits to these data are also shown. These were used to extrapolate to lower temperatures to encompass those used in the embedded flaw bend beam tests.

Table 3.2: Weld chemistry data (% wt)

location	C	Mn	P	S	Si	Ni	Cr	Mo	Nb	V
SN01 - 08*	0.12	1.62	0.011	0.009	0.40	0.14	0.19	0.51	0.002	0.003
SN09 - 16**	0.12	1.52	0.012	0.010	0.44	0.11	0.19	0.51	0.003	0.004

location	Ti	Co	Cu	Al	B	W	As	Sn	Zr	N	O
SN01 – 08*	0.003	0.009	0.03	0.008	0.001	< 0.01	0.008	0.002	0.001	0.010	0.039
SN09 – 16**	0.003	0.009	0.03	0.008	0.001	< 0.01	0.009	0.002	0.002	0.010	0.038

* Specimens taken out near the inner surface
** Specimens taken out near the outer surface

Table 3.3: Young’s Modulus and Poisson Ratio

Material	Young’s Modulus relation	Poisson Ratio
Weld and weld HAZ	E (MPa) = 211877 – 79.131 . T (°C)	0.3
Plate and plate HAZ	E (MPa) = 207200 – 57.1 . T (°C)	0.3
Clad	E (MPa) = 150200 – 86.2 . T (°C)	0.3

Table 3.4: Temperature range covered by the available tensile data.

Material	Temperature Range Investigated
Weld	– 70°C to RT
Plate 100	– 95°C to RT
Plate 200	– 90°C to RT
Weld HAZ	– 70°C to RT
Plate 100 HAZ	– 70°C to RT
Clad	– 95°C to RT

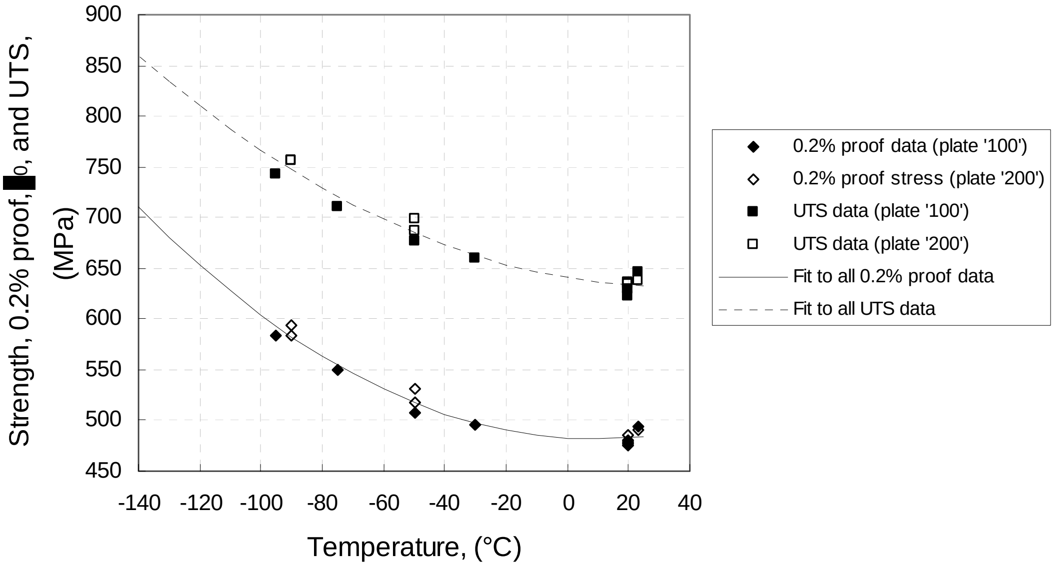

Figure 3.3: Tensile test data for the plate material.

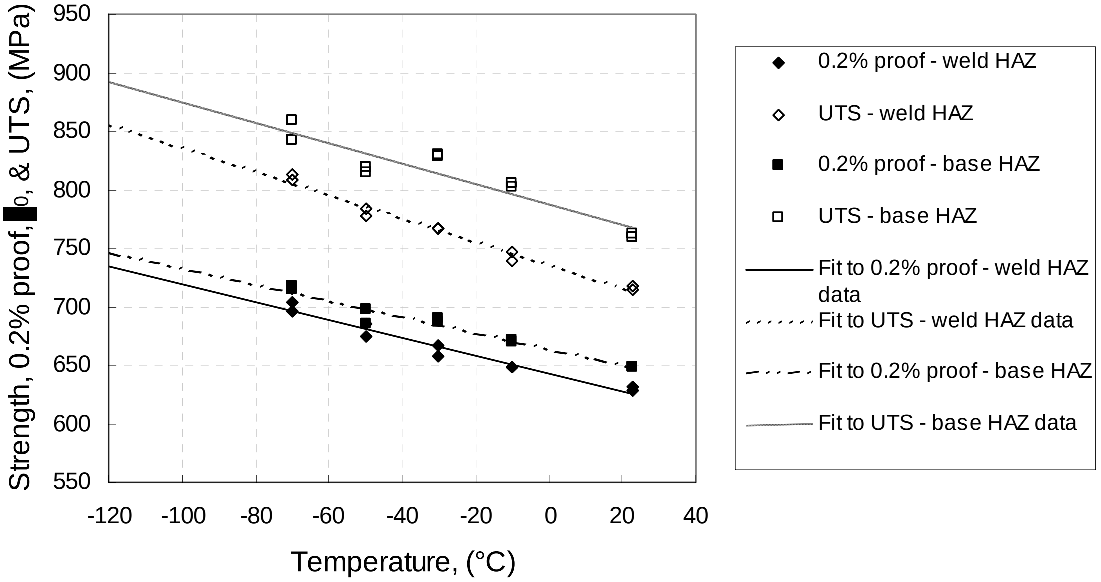

Figure 3.4: Tensile test data for the HAZ.

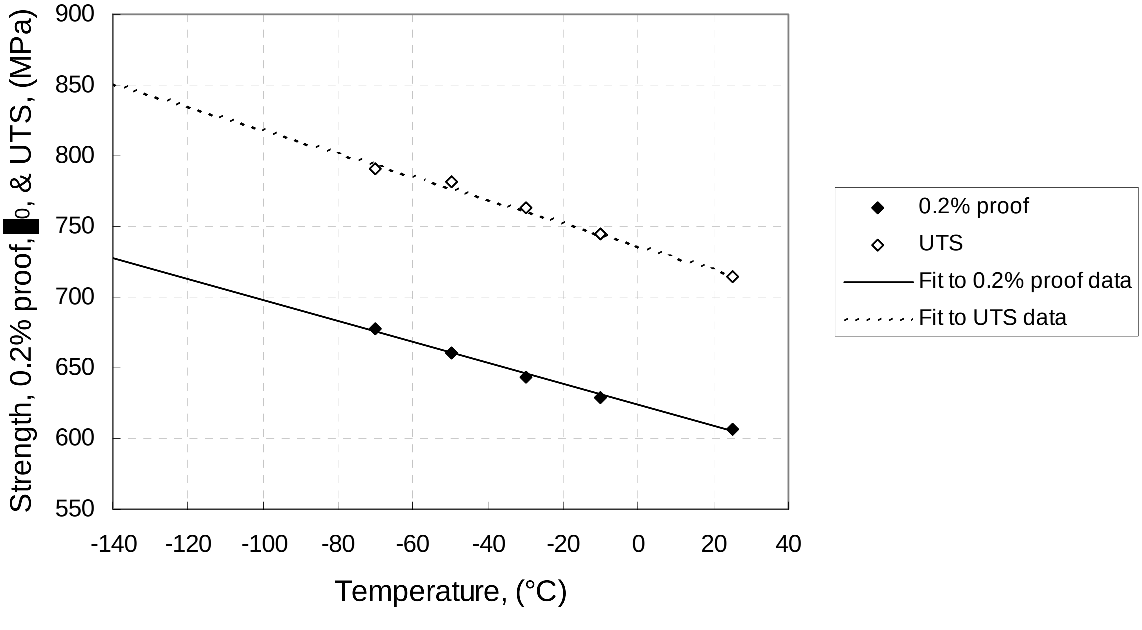

Figure 3.5: Tensile test data for the weld.

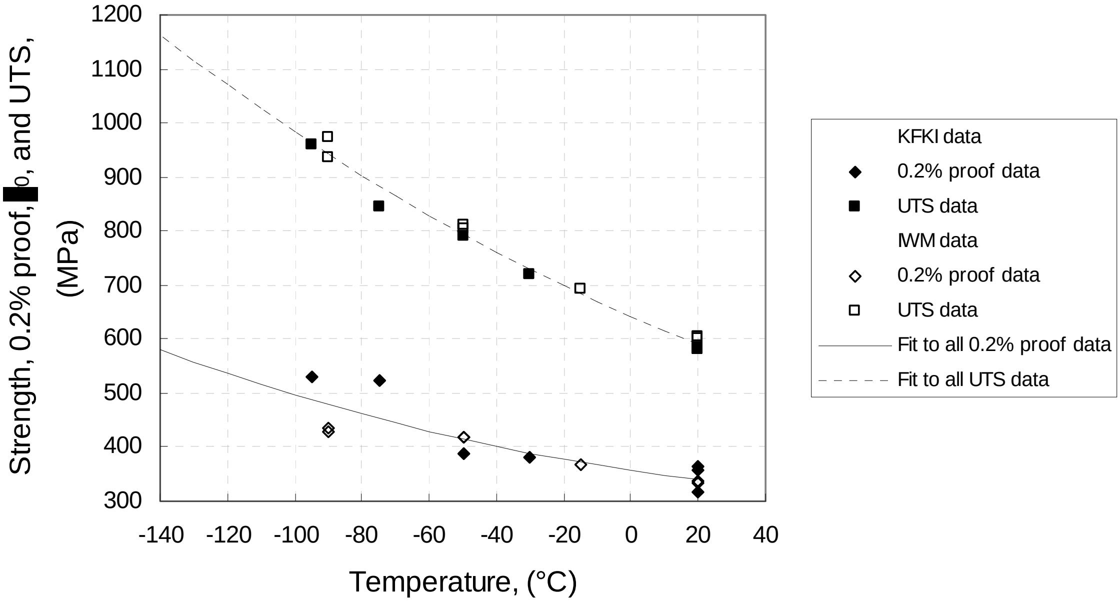

Figure 3.6: Tensile test data for the clad.

The second objective of the tension testing programme was to provide information for the finite element fracture analyses on the true stress – true strain characteristics of the various materials. Figure 3.7 shows the tensile curves measured for the weld metal at various temperatures. Analytically these curves were presented in two forms:

- Ramberg-Osgood type power law expressions:

  For $\varepsilon_{true} \leq \varepsilon_0$, $\varepsilon_{true} = \sigma_{true}/E$; ε_0 = reference strain = σ_0/E

  For $\varepsilon_{true} > \varepsilon_0$, $\varepsilon_{true}/\varepsilon_o = \alpha\times(\sigma_{true}/\sigma_0)^n$ and where $\sigma_0 = R_{p0.2}$

  (n is the strain hardening exponent)

- Piece-wise true stress – true strain data sets.

Table 3.5 shows the best-estimate values of the Ramberg-Osgood function parameters for the plate materials, the weld and the clad, taking the average estimates from the fitting of the tensile test results. It is noted that the form of the stress-strain curve is assumed to be temperature independent up to room temperature.

Table 3.5: Temperature independent estimates of the Ramberg-Osgood parameters.

Material	n	α	ε_o
Weld	8.97	3.430	0.0030
Plate 100 & 200	6.65	3.587	0.0025
Clad	5.48	2.279	0.0025

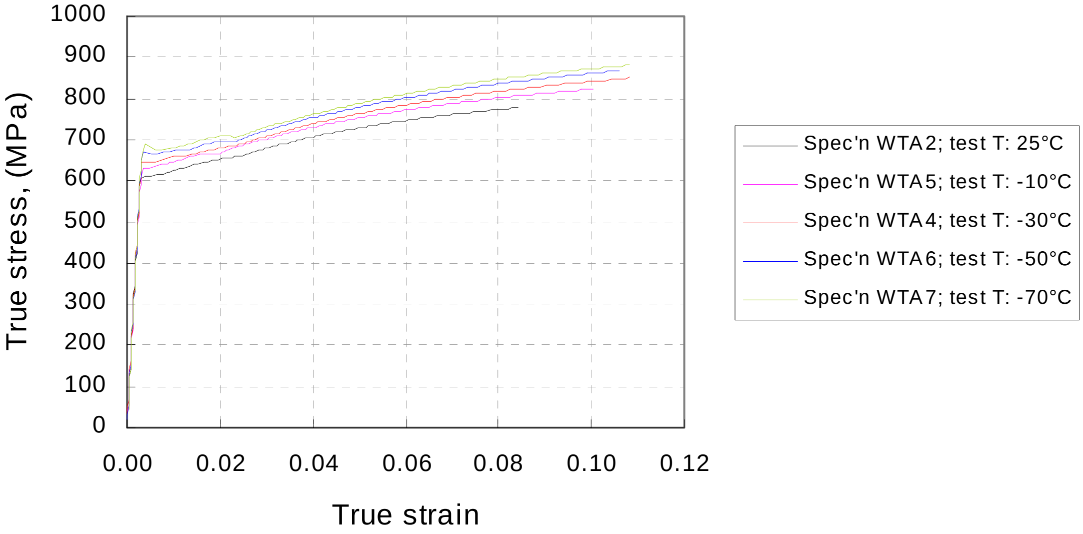

Figure 3.7: Stress-strain curves for the weld material.

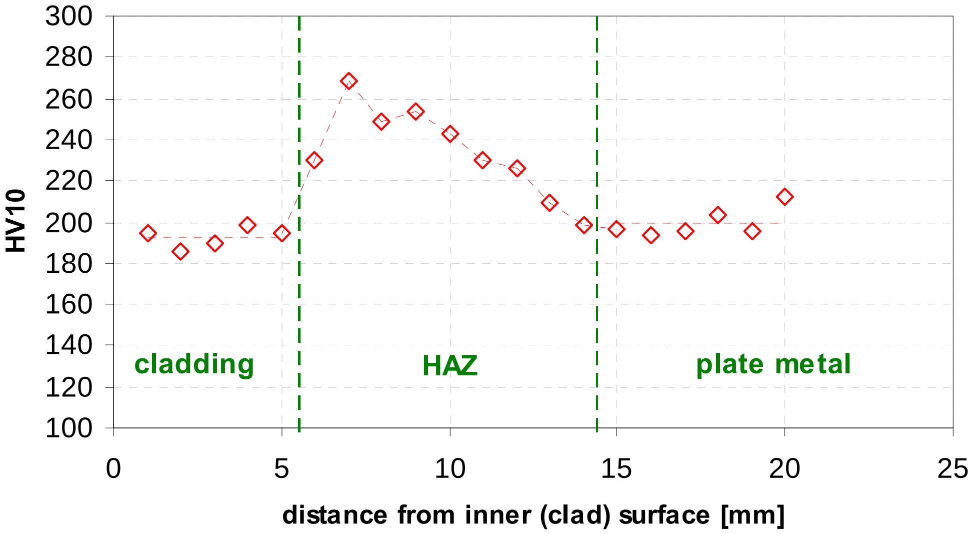

Figure 3.8: Hardness profile covering cladding, HAZ and plate base metal.

3.3.4 Hardness Measurements

In addition to the original test matrix a number of Vickers hardness measurements were performed by JRC addressing the various materials. An indentation force of 10 kgf was applied for each measurement. Figure 3.8 presents one of the resulting hardness profiles covering clad, plate base metal and the induced HAZ. The hardness variation in the HAZ is clearly visible, including a peak close to the fusion line (Coarse Grain HAZ). This peak could correspond to a local region with lower fracture toughness.

3.3.5 Impact Testing

Several series of Charpy tests have been performed as follows:

- for the weld, Plate 100 and Plate 200 materials by JRC,
- for the Plate 100 material by BZF.

All specimens were in the CR orientation i.e. oriented in circumferential direction with crack propagation in radial direction or through thickness direction. Impact energy transition curves measured by JRC are given in Figures 3.9 and 3.10 for the weld and plate specimens respectively. Drop-weight tests were performed by ORNL for the Plate 100, 200 and weld materials, resulting in T_{NDT} data. The reference nil-ductility transition temperature RT_{NDT} was not governed by the Charpy test results and was always equal to T_{NDT}. Table 3.6 summarizes the key parameters obtained from the data.

Table 3.6: Summary of the impact, drop weight and RT_{NDT} parameters

Material	Charpy T_{28J} (°C)	Charpy T_{41J} (°C)	Drop Weight T_{NDT}, (°C)	RT_{NDT} (°C)
Plate 100	-55.1	-45.3	-30	-30
Plate 200	-68.6	-59.0	-35	-35
Weld	-35.3	-24.9	-35	-35

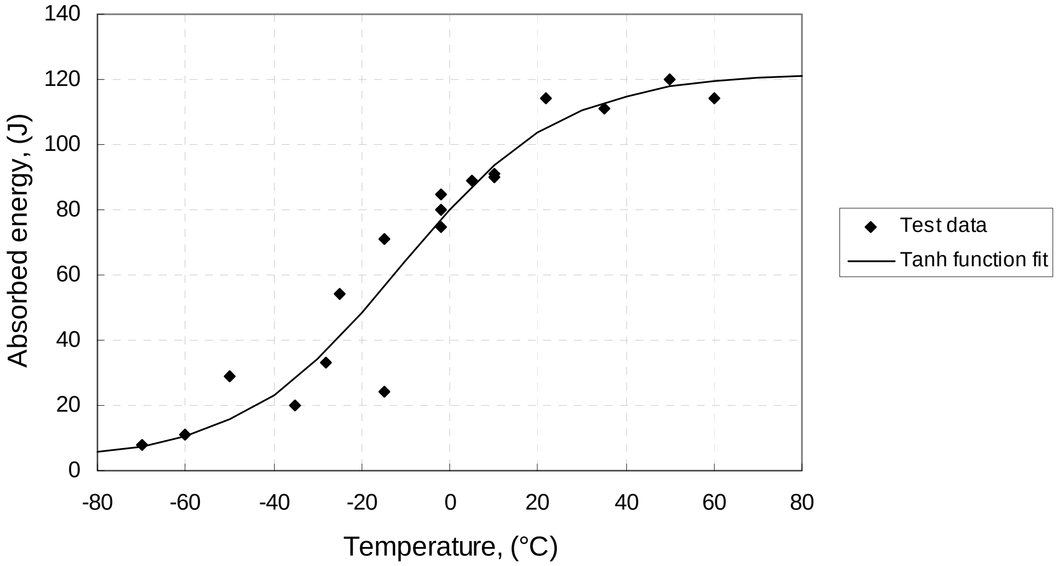

Figure 3.9: Charpy absorbed impact energy curves for the weld material.

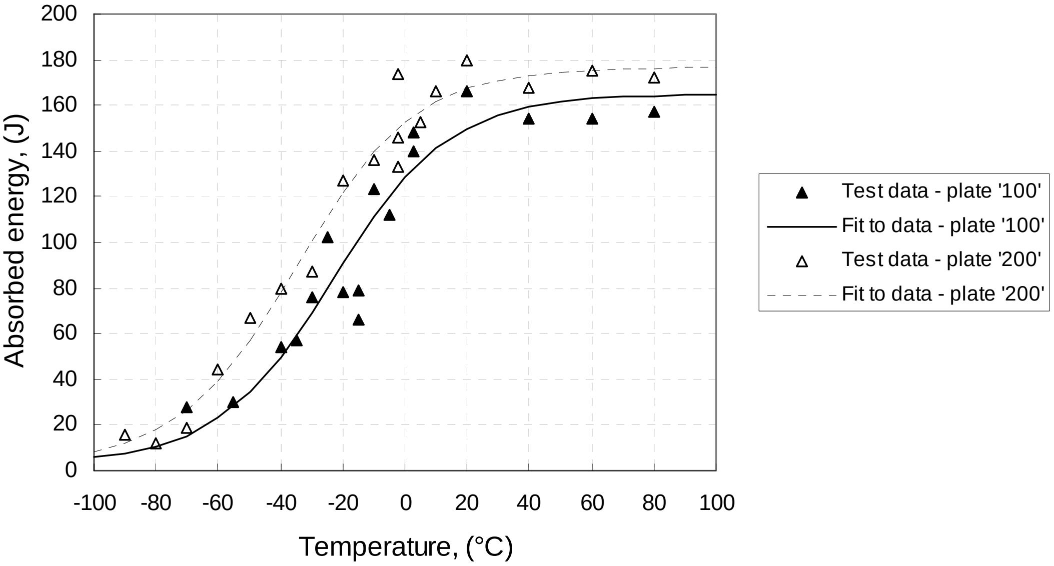

Figure 3.10: Charpy absorbed impact energy curves for the plate material.

3.4 Fracture Toughness Testing

3.4.1 Analysis Methods

The scope of the fracture testing on the PVRUF materials was twofold:

- to obtain a "standard" estimate of the Master Curve T_0 parameter using standard deep notch, i.e. a/W ≈ 0.5, (high constraint) specimens,
- to assess the shift in the transition curve for low constraint specimens.

For evaluation of the K_{Jc} parameter, the method used is essentially as set out in ASTM E1921, and assumes plane strain in the conversion of J_c to K_{Jc}, where:

$$K_{Jc} = \sqrt{[E \times J_c/(1 - \nu^2)]}$$

K_{Jc} values resulting from 10x10 and 10x20 SE(B) specimens were size corrected to the reference thickness dimension of 25 mm. The plastic eta (η) factors are from ASTM E1921 when load line displacement is used for calculating A_p and $a_0/W \geq 0.268$ ($\eta = 1.9$) and from Sumpter [25] for $a/W < 0.268$ ($\eta = 0.32 + 12\times a_0/W - 49.5\times(a_0/W)^2 + 99.8\times(a_0/W)^3$). The η expression when CMOD data are used is from an expression due to Kim & Schwalbe [26] ($\eta = 3.724 - 2.244\times a_0/W + 0.408\times(a_0/W)^2$), which is very close to that in ASTM E1290 (standard for CTOD Fracture Toughness Measurement). For the 25 mm C(T) specimens the evaluation of A_p was based on load-line displacement data and J_p was calculated using the ASTM E1921 expression $\eta = 2 + 0.522\ b_0/W$. The transition curve data were analysed by the Master Curve approach, where the temperature dependence of fracture toughness at different levels of fracture probability (e.g. 5%, 50% and 95%) is given in the form:

$$K_{Jc} = A + B\cdot\exp[C\cdot(T-T_0)] \qquad (1)$$

where T_0 corresponds to the mean fracture toughness level of 100 MPa√m.

Lastly, the representation of the fracture toughness transition curve using the ASME reference temperature parameters RT_{NDT} and RT_{T0} has also been considered. The relevant equation is:

$$K_{Ic} = 36.5 + 3.083 \exp[0.036(T\text{-}RT_{parameter} + 56)]$$

The values for the RT_{NDT} parameter, based on Charpy and drop weight test data, are given in Table 3.6 above. RT_{T0} is determined according to the relation RT_{T0} (°C) = $T_0 + 19.4$.

3.4.2 Plate Fracture Toughness Data

The following test series have been performed on specimens machined from the Plate 100 material:

- IWM undertook tests on 25mm compact tension, C(T), specimens ($a_0/W \sim 0.5$).
- NRI tested 10×20mm single-edge notch bend, SE(B), specimens having a_0/W ratios of ~ 0.5, ~ 0.2 and ~ 0.1.

TWI performed a series of experiments on 10×20mm SE(B) bars, with $a_0/W \sim 0.1$. In addition, NRI carried out tests on Plate 200 using 10×20, $a_0/W \sim 0.5$ SE(B) specimens. In all the experiments crack propagation took place in the radial (through-wall) direction.

The K_{Jc} vs. test temperature data for the $a_0/W \sim 0.5$ specimens from Plate 100 are shown in Figures 3.11 and 3.12 for the SE(B) and C(T) geometries respectively. These data were analysed separately because of the inherent difference in crack tip constraint between both types of specimens. Applying the Master Curve fitting procedure yielded to a T_0 value of -94.9°C for the SE(B) tests and -99.8°C for the C(T) experiments. This is in contradiction to what was expected, bearing in mind the higher constraint situation present in a C(T) specimen. Based on the above analysis, the estimate of the RT_{T0} parameter for the NRI SE(B) specimens is -75.5°C. The corresponding RT_{T0} and RT_{NDT} transition curves are shown in Fig. 3.13.

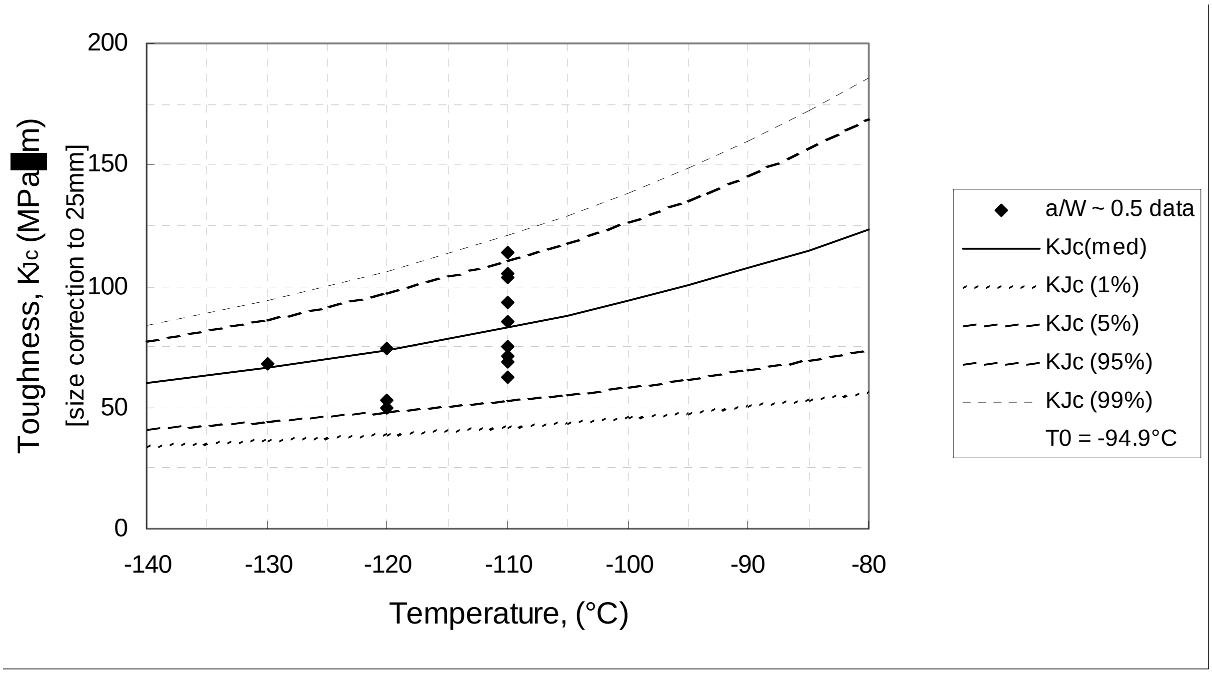

Figure 3.11: Fracture toughness data and Master Curve fit for the Plate 100 material, from tests on SE(B) specimens with a/W ~ 0.5.

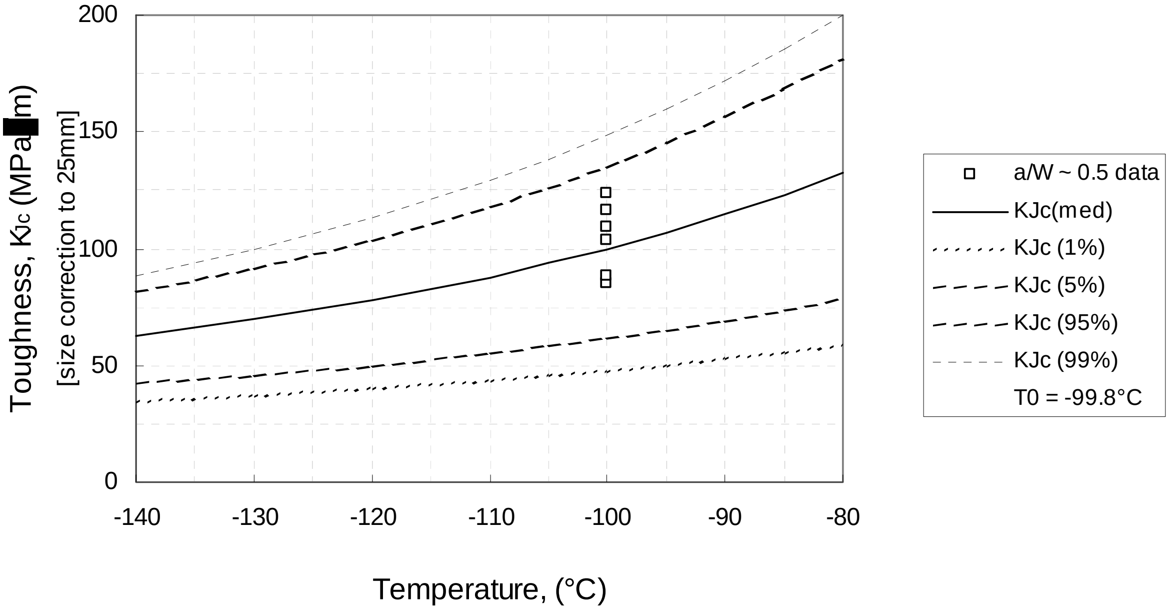

Figure 3.12: Fracture toughness data and Master Curve fit for the Plate 100 material, from tests on C(T) specimens with a/W ~ 0.5.

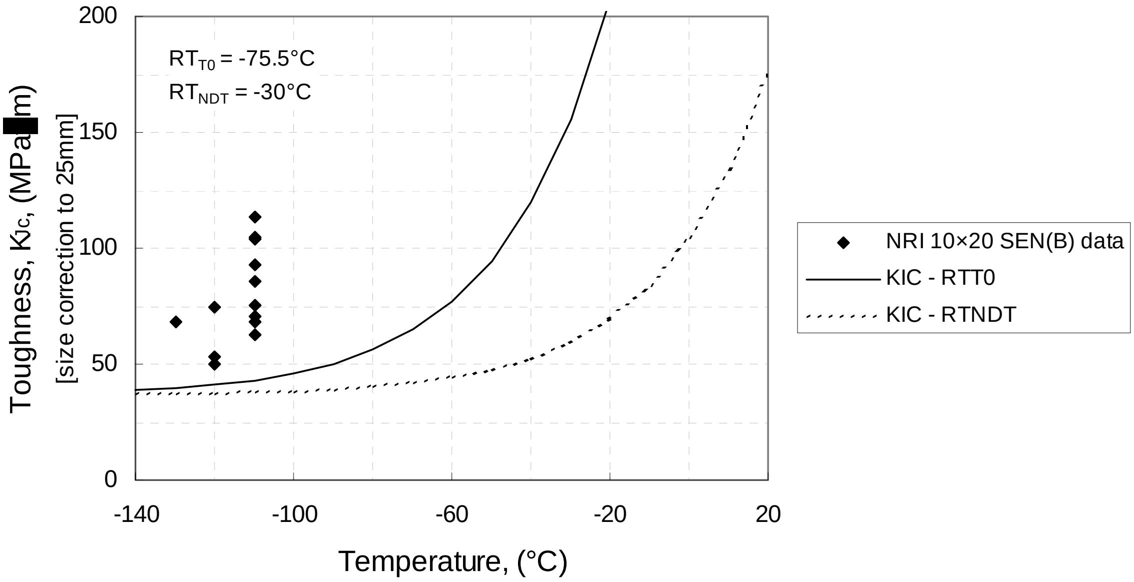

Figure. 3.13: Comparison of Plate 100 SE(B) fracture toughness data with the transition curves based on the ASME RT_{To} and RT_{NDT} parameters

Figure 3.14 shows the analysis of the NRI low constraint SE(B) $a_0/W \sim 0.1$ data, leading to a T_0 value of -120.4°C, which is 25.5°C lower than the figure obtained from the $a_0/W \sim 0.5$ experiments. As is evident from the figure, these NRI tests were executed in the range -130°C to -110°C. Late in the post-test analysis phase of the project, TWI carried out a set of 8 experiments at -80°C on 10x20 mm SE(B) in order to obtain a more accurate estimation of the actual constraint loss around the temperatures used for the embedded flaw beam tests. . The resulting K_{Jc} measurements were very high, leading to 6 invalid values following the specimen dimension requirements of ASTM E1921. Nevertheless all TWI data were included in the Master Curve analysis, applying the E1921 data censoring procedure, i.e. replacing the invalid K_{Jc} values by the maximum K_{Jc} capacity at -80°C. The T_0 was slightly increased to -129.8°C, as is presented in Figure 3.15. This provides clear evidence of a consistent constraint loss effect over the temperature range examined. The TWI test temperature just falls within the range $T_0 \pm 50$°C recommended by the E1921 standard.

In this context it should also be noted that testing the $a_0/W \sim 0.2$ specimens did not show any constraint effect. High and low constraint data are directly compared in Figure 3.15.

The fracture toughness results for Plate 200 material indicated that it possesses slightly different properties to those of Plate 100, as can be appreciated from the comparison of the fracture data shown in Figure 3.16. The T_0 estimate for Plate 200 is -88.2°C, i.e. 11.6°C higher than that for Plate 100.

Table 3.7 summarizes the T_0 values for the different plates, specimen types and a_0/W ratios, which is indicative of the degree of constraint. Since the large scale embedded flaw bend specimens were fabricated from Plate 200, it was decided to assume that the varability in fracture properties due to the influence of reduced constraint for the Plate 200 material would be the same as that exhibited by the Plate 100 tests.

Table 3.7: T_0 estimates from the Plate 100 and 200 fracture toughness data.

Material	Test Specimen and Constraint	Test Temperatures °C	Transition Temperature, T_0 °C
Plate 100 C(T), B=25 mm	$a_0/W \sim 0.5$	-100	-99.8
Plate 100 SE(B)	$a_0/W \sim 0.5$	-110, -120, -130	-94.9
10 mm x 20 mm	$a_0/W \sim 0.2$	-110, -120, -130	-95.0
	$a_0/W \sim 0.1$	-110, -120, -130	-129.8
Plate 200 SE(B)	$a_0/W \sim 0.5$	-110, -75	-88.2
10 mm x 20 mm	$a_0/W \sim 0.1$	-	*-123.1* *inferred fromT$_0$ shift for Plate 100*

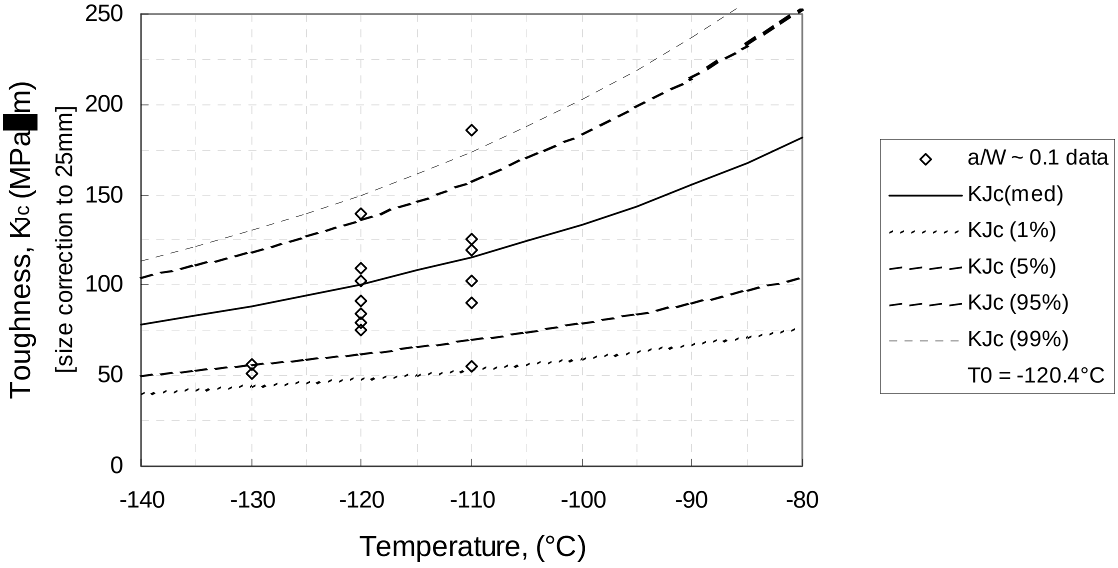

Figure 3.14: Low constraint fracture data for Plate 100, from SE(B) tests with a/W ~ 0.1.

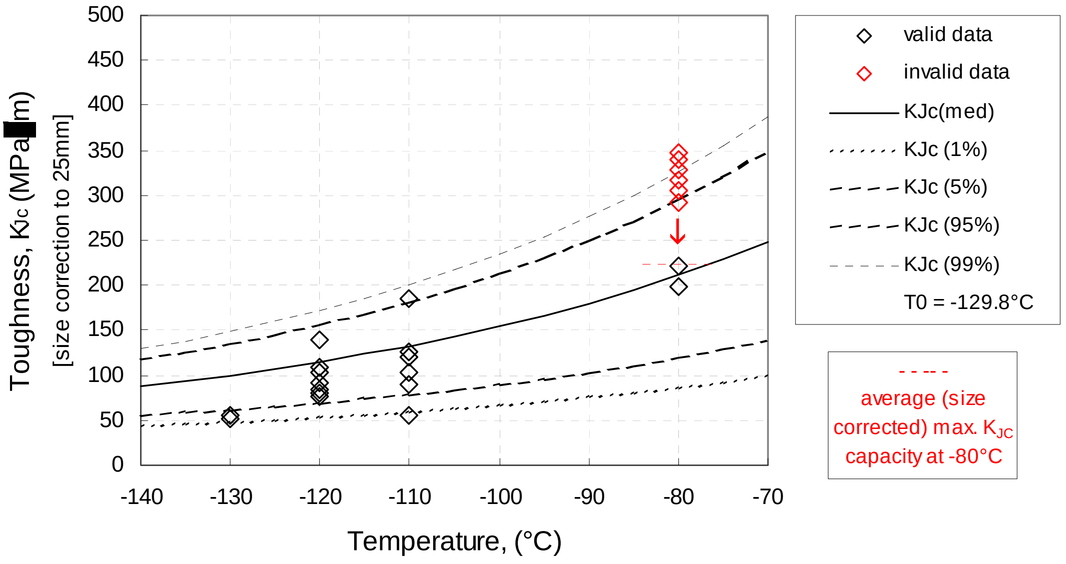

Figure 3.15: Low constraint fracture toughness data for Plate 100, from SE(B) tests with a_0/W ~ 0.1 performed by NRI (range -130 to -110°C) and TWI (-80°C).

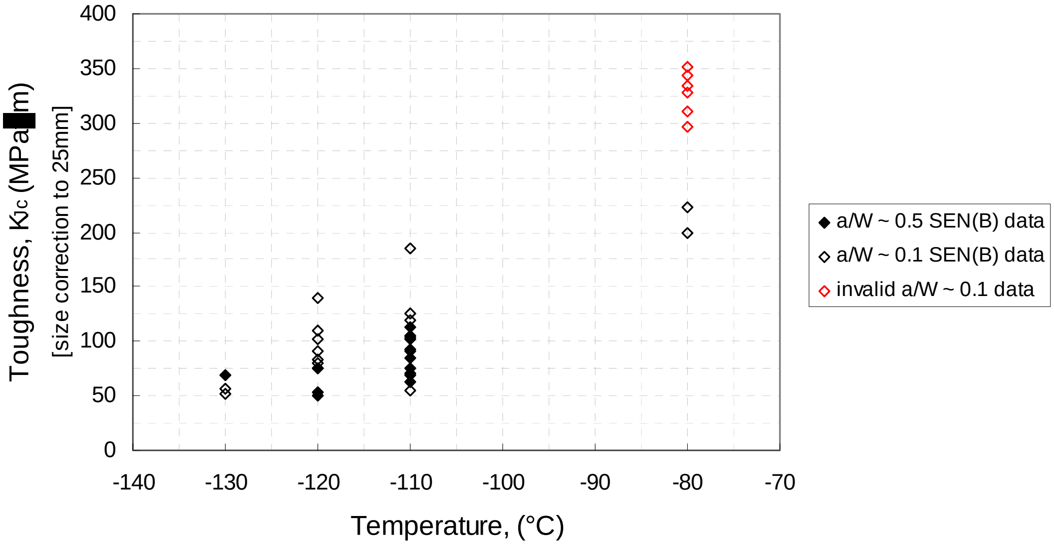

Figure 3.16: Comparison of $a_0/W \sim 0.1$ and $a_0/W \sim 0.5$ SE(B) data for the Plate 100 material.

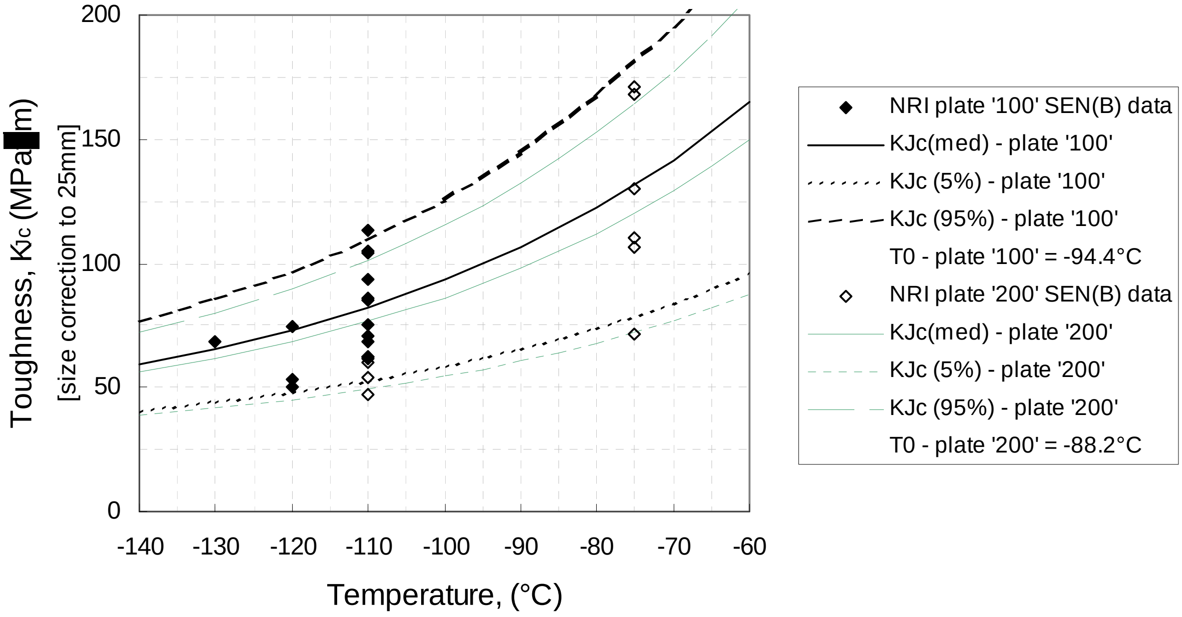

Figure 3.17: Comparison of the SE(B) fracture data for the Plate 100 and Plate 200 materials.

3.4.3 Weld Fracture Toughness Data

For the specimens machined from the weld, the scope of the fracture test programme and the adopted analysis procedure was essentially the same as that for the plate specimens.

The following testing has been performed:

- IWM and ORNL undertook tests on 25mm compact tension, C(T), specimens with $a_0/W \sim 0.5$.
- VTT performed fracture tests on 10x10 mm SE(B) specimens with $a_0/W \sim 0.5$ and ~ 0.1

In these test series the specimen orientation was CR i.e. the crack propagation was in the through-wall radial direction.

The K_{Jc} data for the deep notch SE(B) specimens are shown in Figure 3.18, together with the fitted Master Curve. When the IWM and ORNL C(T) data were compared - see Figure 3.19 - it was immediately apparent that the set of specimens tested by IWM possesses a markedly different and higher T_0 reference temperature than the set tested at ORNL. Investigation indicated that this was probably due to the location of the pre-crack tips in the IWM specimens, which appeared to sample material close to the weld root region. Although details of the welding procedure have not been obtained, it is considered that the material region investigated by IWM (around the centre of the weld thickness) was not appropriate to the near-surface flaw location in the large-scale specimens being tested in this project. The Master Curve fit to the VTT SE(B) data produced a T_0 estimate of -94.8°C and the T_0 obtained from the ORNL C(T) experiments was equal to -73.6°C.

Based on the above analysis, the estimate of the RT_{T0} parameter for the SE(B) specimens is -75.4°C. The corresponding RT_{T0} and RT_{NDT} transition curves are shown in Fig. 3.20.

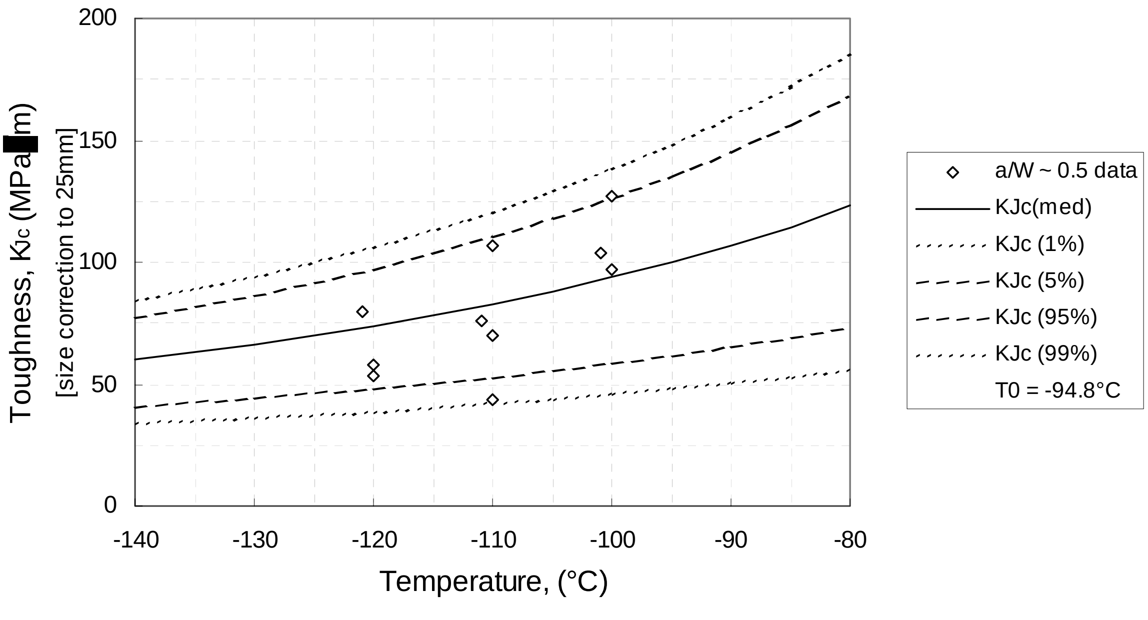

Figure 3.18: Fracture toughness data and Master Curve fit for the weld material, from tests on SE(B) specimens with a/W=0.5.

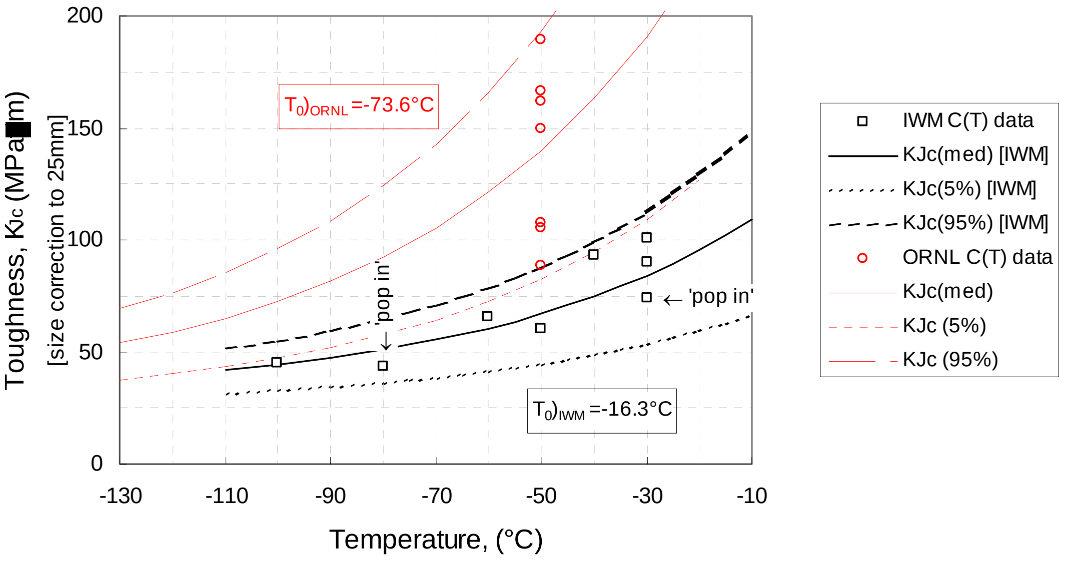

Figure 3.19: Fracture toughness data and Master Curve fit for the weld material, from tests on C(T) specimens with a/W ~ 0.5.

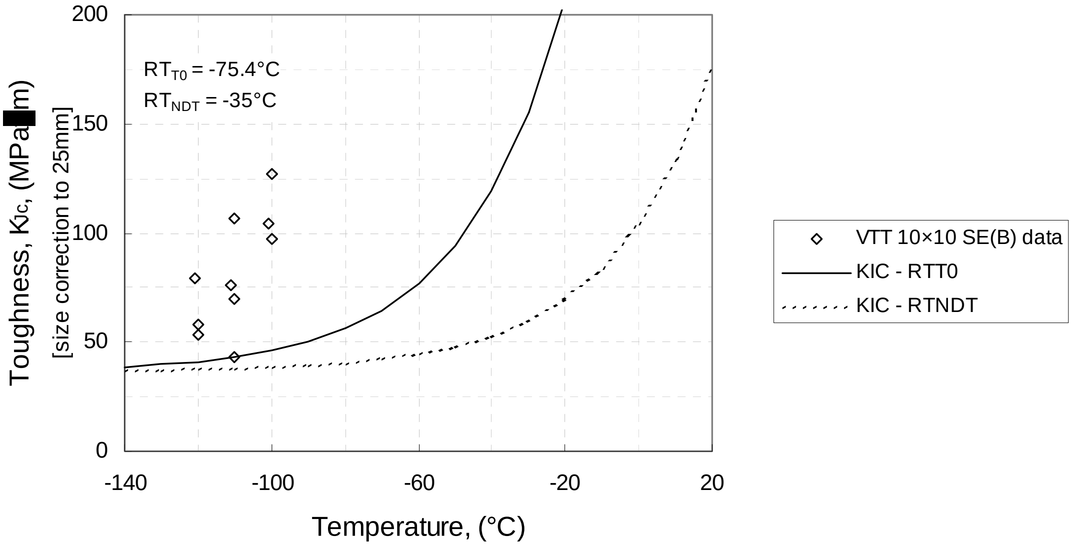

Fig. 3.20: Comparison of SE(B) weld fracture toughness data with the transition curves based on the ASME RT_{To} and RT_{NDT} parameters.

For the low constraint tests performed at VTT, the $a_0/W \sim 0.1$ specimens were taken from two of the weld blocks and appear to give rise to somewhat different populations, at least at the lower temperatures tested. However, in the Master Curve analyses, the data have been treated as a single set (Figure 3.21), to give a T_0 estimate of -132.8°C (it was shown that the T_0 estimates for the specimens from each block differ by ~8ºC). The T_0 shift due to the introduction of a shallow notch ($a_0/W \sim 0.1$) is -38°C, which is similar to the observation made for the Plate 100 metal. The high and low constraint data obtained for the weld specimens are directly compared in Figure 3.22.

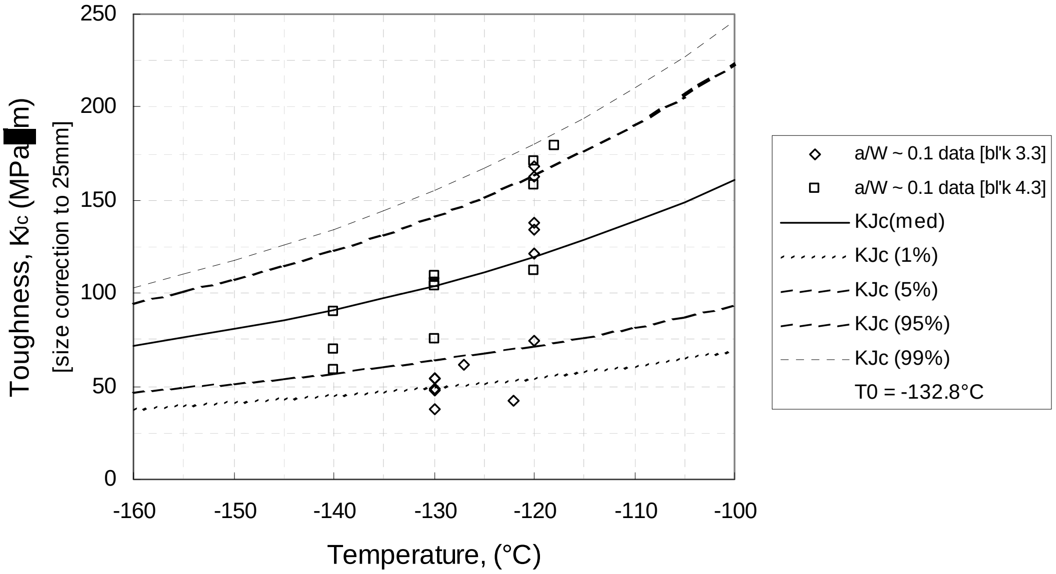

Figure 3.21: Low constraint fracture toughness data for the weld material, from SE (B) tests with a/W ~ 0.1.

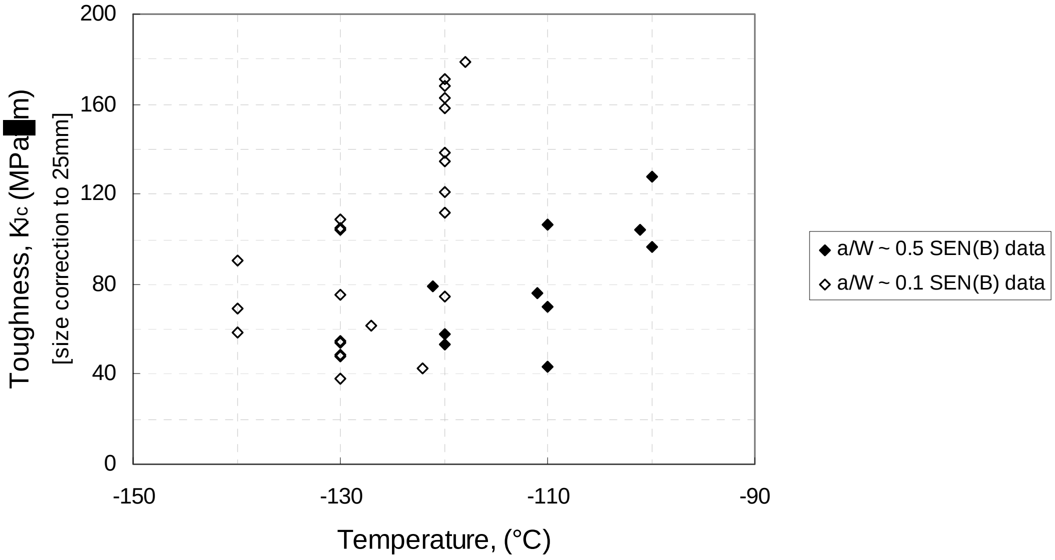

Figure 3.22: Comparison of a/W ~ 0.1 and a/W ~ 0.5 SE(B) data for the PVRUF weld material.

Table 3.8 presents the weld T_0 values for different specimen types and a_0/W ratios, which is indicative of the degree of constraint.

Table 3.8: T_0 estimates based on the weld fracture toughness data.

Material	Test Specimen and Constraint	Test Temperatures °C	Transition Temperature, T_0 °C
C(T), B=25 mm	$a_0/W \sim 0.5$	-50	-73.6
SE(B) 10 mm x 10 mm	$a_0/W \sim 0.5$	-100, -110, -120	-94.8
	$a_0/W \sim 0.1$	-120, -130, -140	-132.8

3.4.4 Constraint Analysis

For both the plate and weld materials, a number of analyses of constraint parameters have been performed in the scope of the TG2 activities. Two models/procedures have been considered:

- the m, α_{R6} and β_{R6} parameters to permit the drawing of constraint modified R6 diagrams [27,28].
- the Weibull stress and modulus as described by the Gao and Dodds $\Im$ function [29].

Below two examples of these analyses are briefly described:

A R6 constraint analysis for Plate 100 was carried out for a temperature equal to -110°C and using the NRI $a_0/W \sim 0.5$ and ~ 0.1 SE(B) data sets. A "mean" K_{Jc} value was calculated for both a_0/W ratios, using the average dimensional and load at fracture measurements obtained from all the specimens tested at -110°C. The biaxiality ratio β, T-stress and T/σ_0 ratio (normalized T-stress) were calculated for both K_{Jc} values. T/σ_0 was equal to 0.16 for $a_0/W \sim 0.5$ and -0.53 for $a_0/W \sim 0.1$. Subsequently the parameters required to draw the low constraint R6 diagram could be assessed (m, α_{R6} and β_{R6}). Figure 3.23 presents the R6 rev. 4 option 1 FAD together with the modified R6 FAD. K_{mat} was chosen as $K_{Jc(1\%)}$ from the Master Curve. The actual $a_0/W \sim 0.5$ and $a_0/W \sim 0.1$ data points are also included.

With respect to the Gao and Dodds $\Im$ function procedure, all NRI Plate 100 data sets were considered. First of all data to enabling plots of $K_{Jc}/K_{Jc(1\%)}$ and $K_{Jc}/K_{Jc(0.1\%)}$ vs T/σ_0 for the measured toughness results were derived. The $K_{Jc(1\%)}$ and $K_{Jc(0.1\%)}$ figures are the 1% and 0.1% lower bounds to the high constraint data sets, obtained from the Master Curve. Lower bounding curves to the toughness data were described by the Gao and Dodds $\Im$ function. In the derivation of this function, the assumed Ramberg-Osgood work hardening parameter 'n' value was that derived from fitting the stress-strain data. Figure 3.24 gives the $K_{Jc}/K_{Jc(1\%)}$ vs T/σ_0 plots for Plate 100, including the actual data points and the Gao and Dodds $\Im$ function.

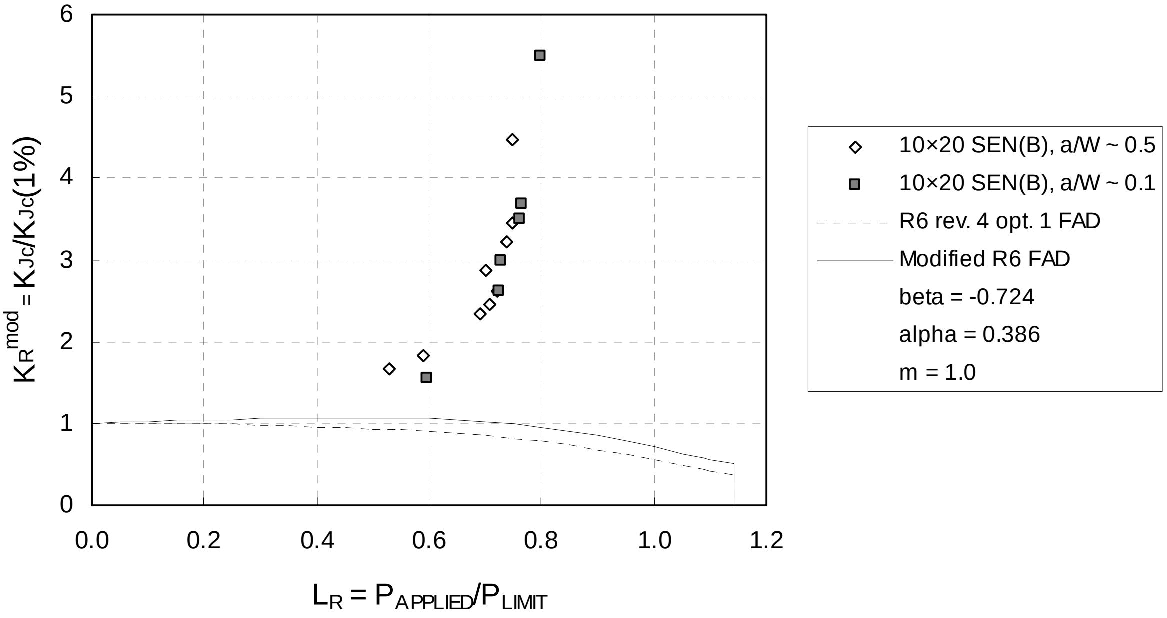

Figure 3.23: Comparison of Plate 100 a/W ~ 0.5 and ~ 0.1 SE(B) test data at -110°C with a modified R6 diagram

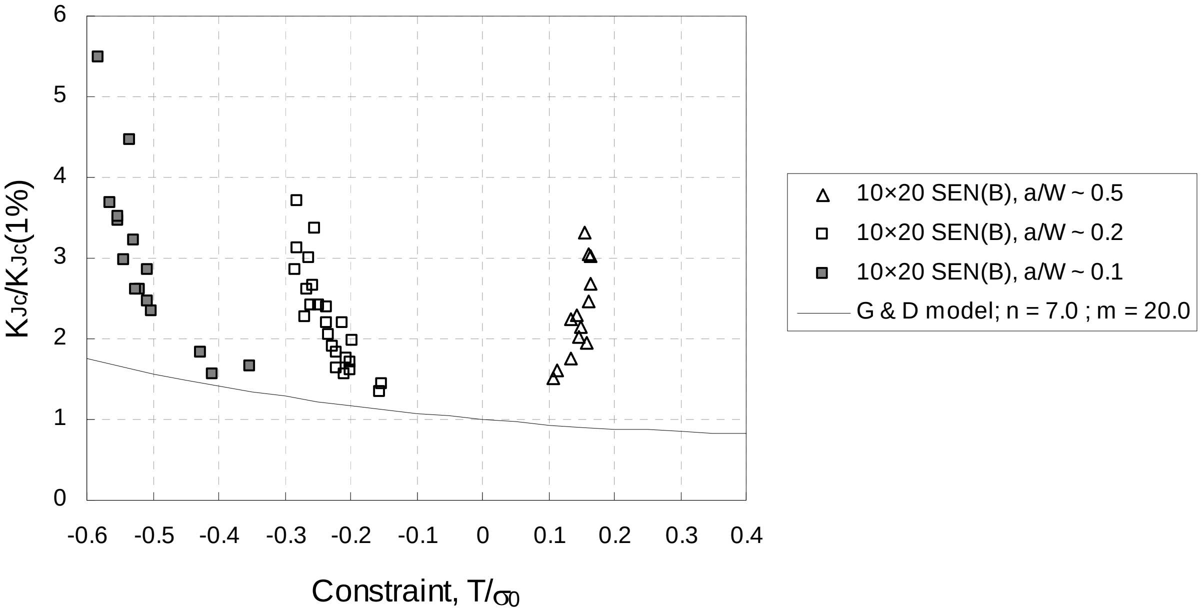

Figure 3.24: Plot of ratio of measured to bounding toughness vs constraint, T/σ_0

4 FEATURE TESTING PROGRAM

4.1 Biaxial Bend Tests

4.1.1 Test Piece Geometry & Fabrication

The overall design of the cruciform test pieces is shown in Fig. 4.1. The central section was machined from the PVRUF longitudinal weld. The nominal thickness is 101.6 mm of which 6 mm is the austenitic cladding. The semi-elliptical flaw was introduced by electro-discharge machining (Fig. 4.2) in each test piece. Its length orientation was parallel to the longitudinal weld and it extended in the weld through-thickness direction. After pre-cracking the final nominal dimensions were 53.3 mm long and 19.1 mm deep (including the cladding). The dimensions of the test piece after the welding of the loading arms is shown in Fig. 4.3.

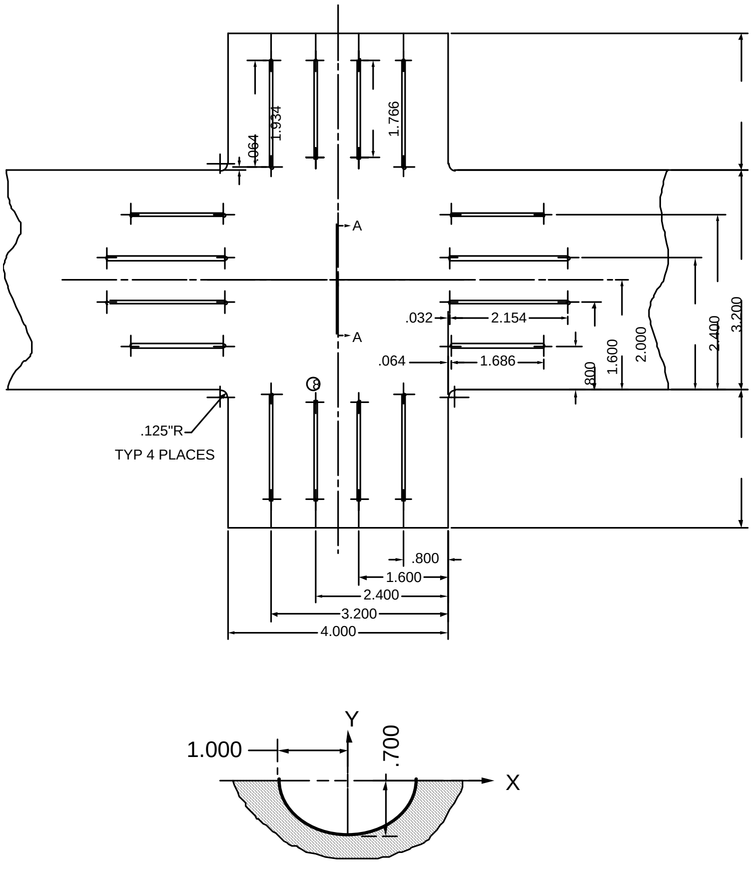

SECTION A-A
NOT TO SCALE

Figure 4.1: General dimensions and layout of test section of clad cruciform specimen (dimensions are in inches).

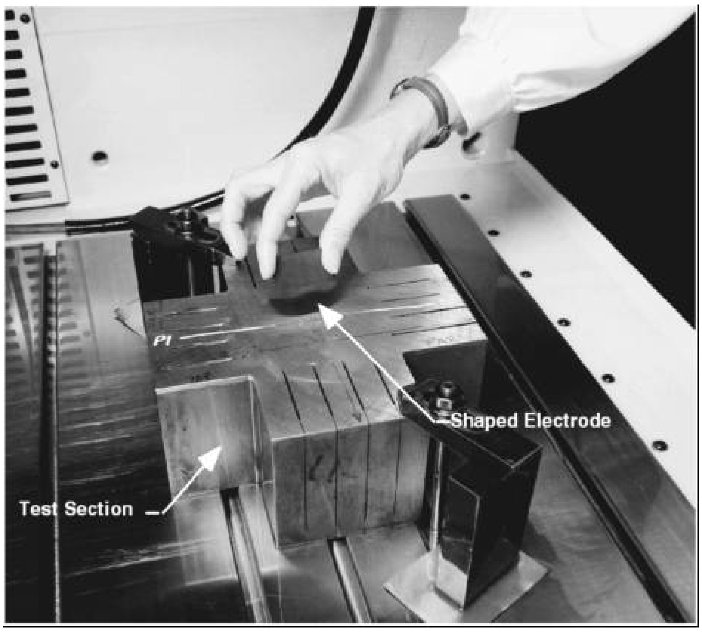

Figure 4.2: The shaped electrode used to machine semi-elliptic through-surface flaw.

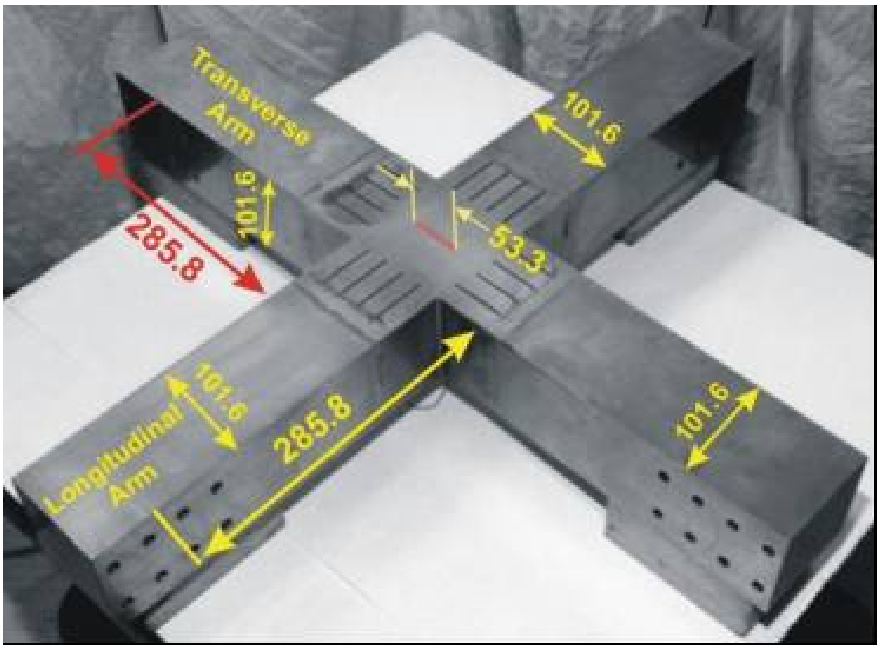

Figure 4.3: The completed cruciform test piece (dimensions in mm's).
N.B. The terms longitudinal and transverse refer to the testing device and not to the orientation of the flaw with respect to the vessel shell.

4.1.2 Residual Stresses

Experience gained in previous testing and analyses of clad beam specimens has shown that residual stresses have a measurable effect on fracture toughness values obtained. For these cruciform bend specimens, much of the through-wall weld residual stress is by removal of material. The dominant remaining residual stress is that in the clad layer. Framatome ANP GmbH performed a residual stress measurement using the ring core technique. The measurement was made at the weld on a 100 mm wide strip of beam no. 2. The obtained profiles are shown in Fig. 4.4.

Cladding:	0 – 6.5 mm;	Youngs Modulus = 186 GPa
HAZ:	6.5 – 13.5 mm;	Youngs Modulus = 200 GPa
Weld:	> 13.5 mm;	Youngs Modulus = 210.5 GPa

Probenbez. : NESC 4
Messposition .: mitte Werkstück
Werkstoffdaten:
E-Modul ......: 186000 bis 210500 N/mm2
Querkont.zahl.: 0.3

Diskettenbez. : E-SPAN-5505, Nr.: 2
Rekordnummer .: 43
Aufnahmedatum : 20.07.01, Uhrzeit : 14:44

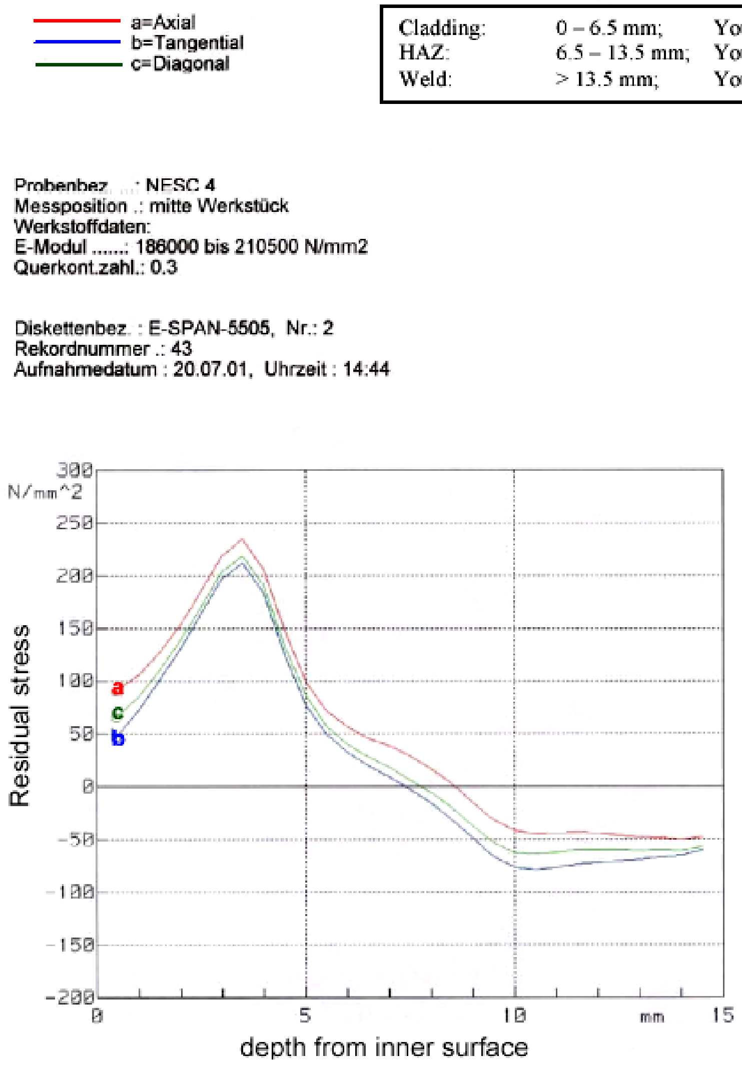

Figure 4.4: Ring-core measurements of the residual stress in the clad and weld HAZ.

4.1.3 Test Procedure and Results

Testing was performed in the ORNL 3.1 MN servo-hydraulic testing machine under 8-point loading to produce a uniform biaxial bending regime. The support lines for the beam were at the edge of the test section, 50.8 mm from the specimen center. The moment arm was 285.8 mm. The specimens were instrumented with eight thermocouples and three crack-mouth-opening displacement (CMOD) gages before installation in the test machine. To achieve the selected test temperature liquid nitrogen cooling was applied using an electrically-controlled manifold system (Fig. 4.5). The thermocouples readings typically indicate a consistent 5˚C (approximate) temperature difference from top to bottom surface of the specimen (the top surface receives the liquid nitrogen spray).

The key experimental variable is the test temperature of the beam, the objective being to achieve cleavage failure in the non-linear region of the load-versus-CMOD curve. Furthermore each set of specimens should be tested at a single temperature to facilitate statistical analysis of the results. However selection of a suitable temperature proved not to be straightforward. In the first test with a target crack-tip temperature of -60˚C as recommended by the TG3 analysts, the specimen failed well within the elastic region of the load-versus-CMOD curve. As a consequence, the subsequent tests were performed at slightly higher temperatures, in the range –40 to –33°C. Table 4.1 reports the test temperature and the moment and CMOD values at fracture. Fig. 4.6 shows the load-CMOD data.

Table 4.1: Failure conditions for PVRUF clad cruciform specimens.

Specimen Number	Specimen Type	Load Ratio	Test Temperature[2] (°C)	Fracture Moment (kN-m)	Fracture CMOD (mm)
PVR-4[1]	Clad Beam	1.0	-55.0	70.0	-
PVR-3	Clad Beam	1.0	-40.6	97.6	0.183
PVR-5	Clad Beam	1.0	-33.4	147.5	0.870
PVR-2	Clad Beam	1.0	-38.3	140.2	0.500
PVR-6	Clad Beam	1.0	-35.3	150.7	0.860
PVR-1	Clad Beam	1.0	-40.2	112.2	0.223

Notes

[1] Due to a data acquisition system malfunction the data were lost; estimated test conditions and results based on visual observation of test trace on computer screen.

[2] Temperature at the deepest point of the flaw estimated from a weighted average of the thermocouple data.

Fig. 4.5 View of the biaxial test, showing the liquid nitrogen containers used to control the temperature.

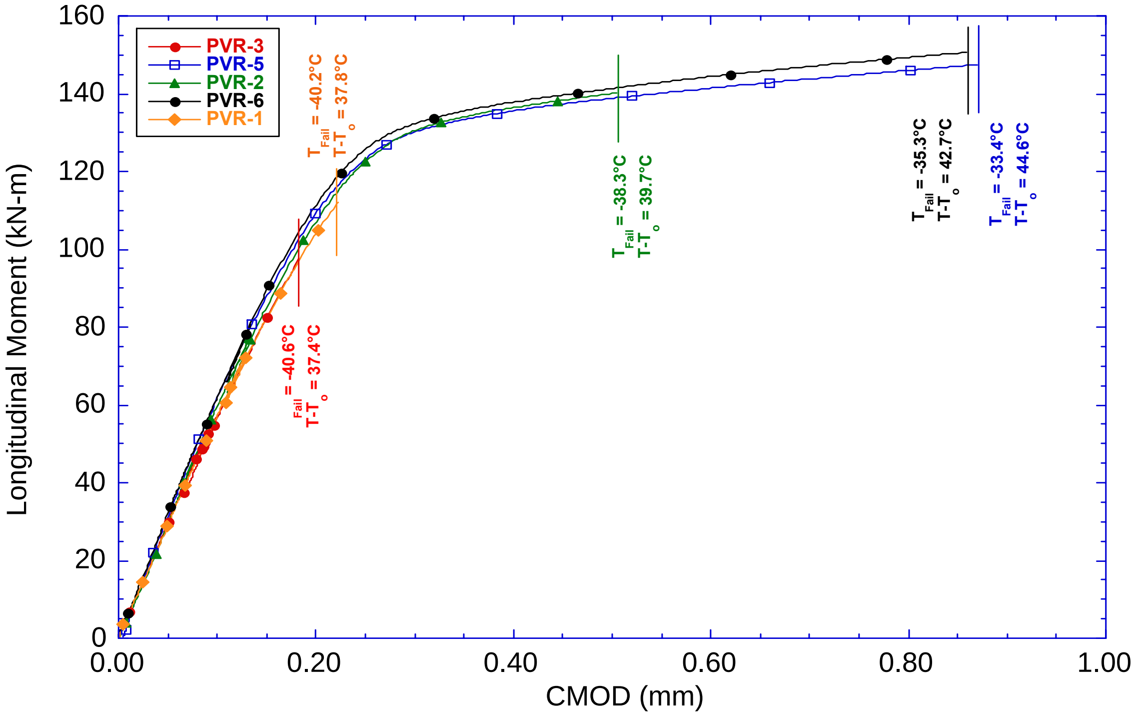

Figure 4.6 Applied longitudinal moment versus CMOD during five of the PVRUF cruciform beam tests.

4.1.4 Post-Test Fractography

The post-test fractography confirmed that the failure mode was pure cleavage fracture, without prior ductile tearing. Two labs checked the position of the cleavage initiation points (often more than one for a given specimen). As shown in Figure 4.7, these tended to occur towards the surface of the specimen rather than at the deepest point (Fig. 4.8).

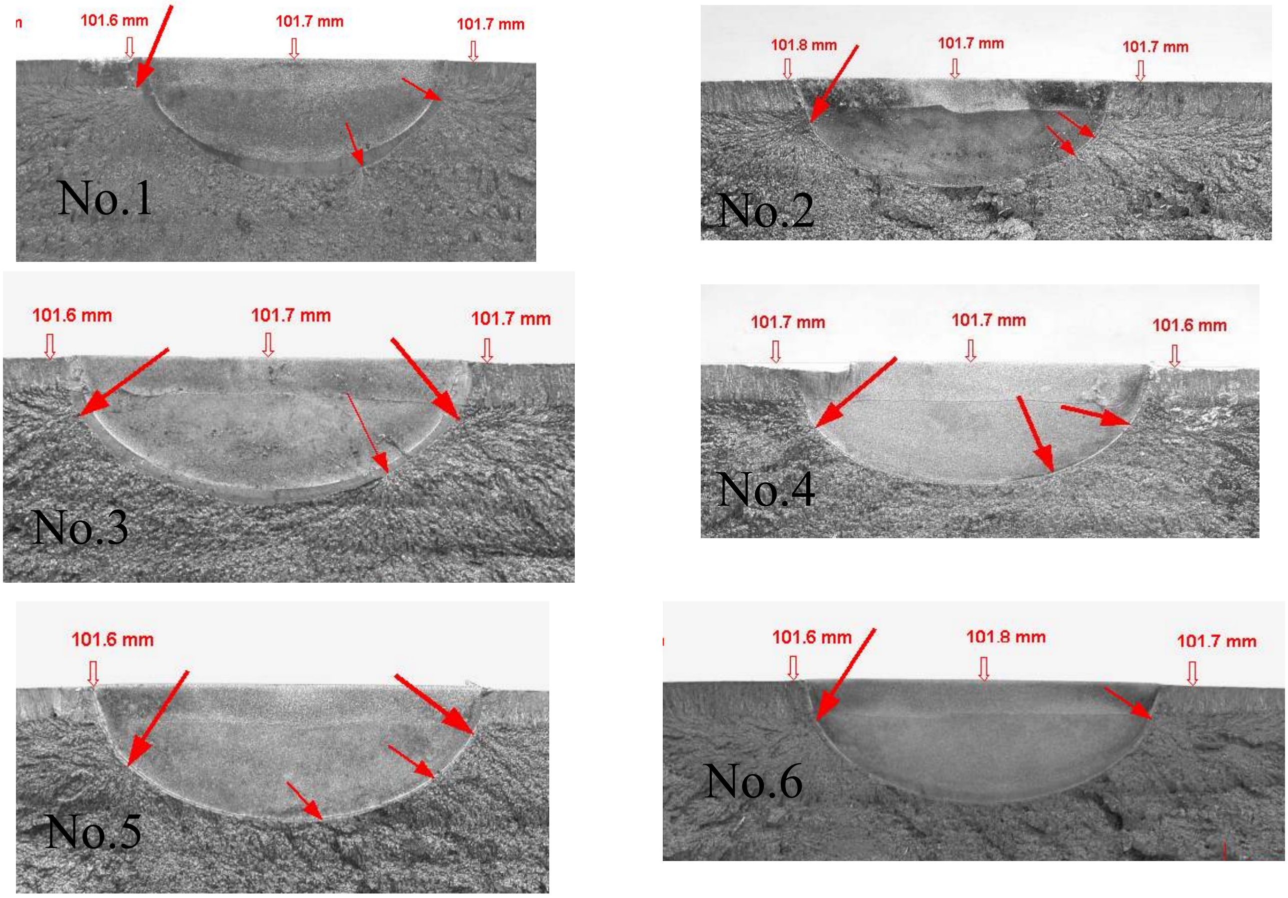

Fig. 4.7 Fracture surface from the cruciform beams specimens; the red arrows point to initiation sites.

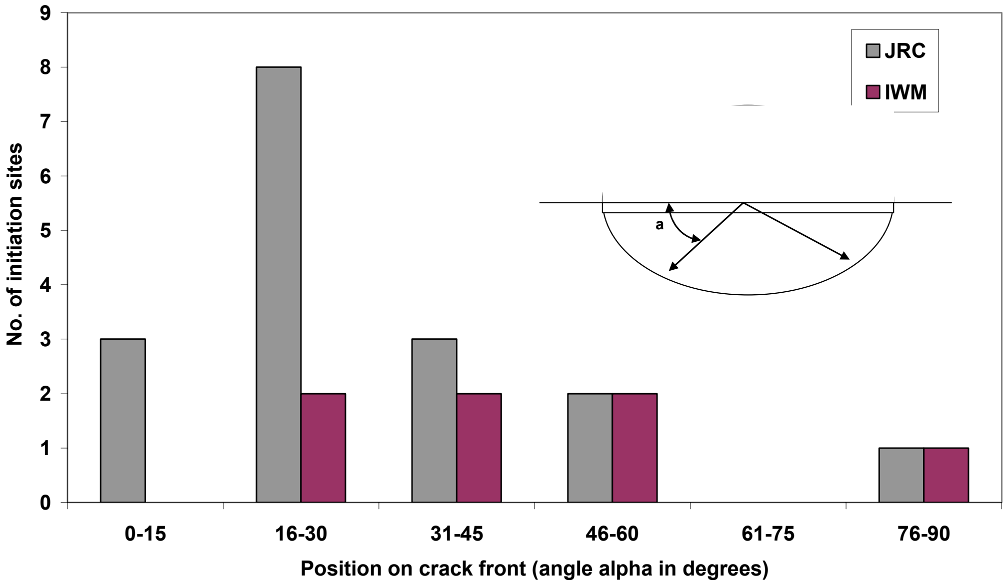

Fig. 4.8 Distribution of initiation sites for all the biaxial bend tests (for some specimens several sites were identified).

4.2 Embedded Flaw Specimens

4.2.1 Test Piece Geometry & Fabrication

The embedded flaw test pieces consisted in beam with nominal 101.6 x 101.6 mm square section and an overall length 800 mm. A through-thickness slot close to the upper (tension) surface was used to simulate an embedded flaw. Two material configurations were used: A533 B base steel plate with and without cladding. Fig. 4.9 gives details of the construction of the clad beam specimens and the geometry of the embedded flaw. This type of simulated flaw differs significantly from that used in previous studies, which have typically used specimens with surface defects that are then cladded over, so that the shallow tip of the defect is at the clad interface. For the selection of the notch geometry the following considerations were addressed.

- The shallow crack tip should be in the base material, but as close as possible to the clad.
- The length of the crack should be representative of what is used in safety assessments.
- Crack initiation should occur in the lower transition region.
- Clad and unclad specimens should have the same notch geometry.
- Crack initiation should occur at the shallow crack tip.

Keeping the height of the ligament from the upper or “shallow” tip to the free surface fixed at 14 mm, the consequences of using different flaw heights were analyzed[2] With a small flaw height value of 10 mm it was predicted that the beam would have to be loaded beyond the nominal plastic collapse load to produce initiation, and that this was likely to then occur at the deep tip. Flaw heights of greater than 20 mm were excluded as being too much greater than those in distributions of postulated sub-surface flaws for operational reactor pressure vessels. Hence a nominal 20 mm flaw height was selected. The unclad specimens had identical beam and flaw geometry as the clad ones.

---

[2] . The ligament of 14 mm was intended to ensure that the near surface crack tip was below the heat affected zone of the cladding in the case of the two clad specimens

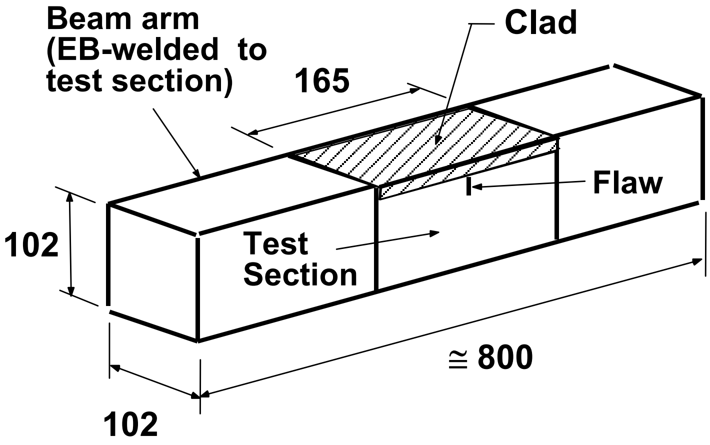

Fig. 4.9 Design of the embedded flaw test piece (dimensions in mm).

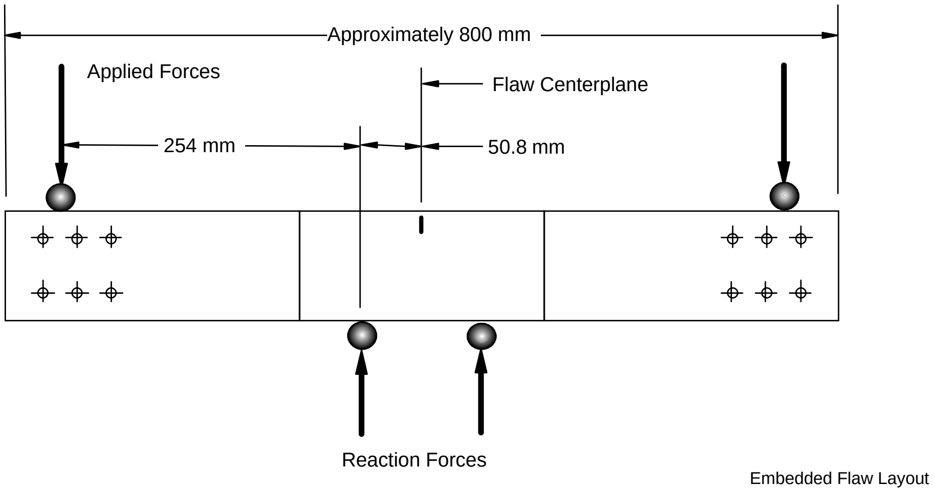

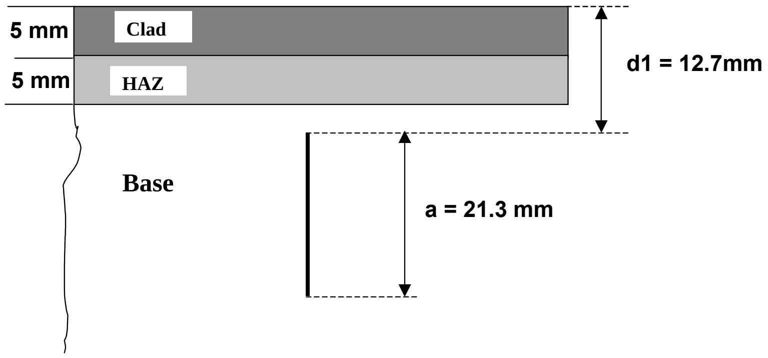

Fig. 4.10 Schematic of the embedded flaw beams with the flaw dimension after fatigue sharpening.

The fabrication sequence followed the experience gained on specimens with surface breaking flaws. To conserve material only the central section of the beam was taken from the plate of interest. The attaching of extension arms with electron beam welds completed the beam specimen. For the defect insertion, a wire electro-discharge machining process was used to create a uniform crack-like slot of 0.3 mm width. To allow the wire to pass through the beam a small hole is first drilled; then the wire-electrode EDM machine cuts the slot above and below the starter hole. The major advantage of this procedure is that there is no metallurgical alteration of the material between the flaw tip and surface. Prior to fracture testing the beams were pre-fatigued to produce approximately 1.3 mm crack growth at the shallow tip. The final flaw height was 21.3 mm with a ligament of 12.7 mm, as shown in Figure 4.10.

4.2.2 Test Procedure & Results

The beams were tested by ORNL in a 3.1 MN servo-hydraulic testing machine in four-point bending. The inner loading span was 101.6 mm and outer loading span was 609.6 mm, giving a moment arm of 254 mm. Liquid nitrogen cooling was applied to the insulated specimens using an electrically-controlled manifold system. For temperature control the specimens were instrumented with five thermocouples. Two pairs were attached at the side of each beam corresponding to the height of the upper and lower flaw tip. The 5th thermocouple was attached to the bottom of the specimen. In general the system succeeded in maintaining a temperature difference of ±1°C between the upper and lower flaw tips. Crack-mouth-opening displacement (CMOD) gages were also attached on each side of the specimen, 21 mm below the upper beam surface (Fig. 4.11).

The first test (4.1.1) on an un-clad beam was performed at -128°C, some 30^{o} below the estimated T_o value for the plate material, and failed in cleavage at a relatively low applied load, well within the elastic region of the applied load versus CMOD curve. The test temperature choice had been influenced by the pre-test FE analyses, which as it turned out, overestimated the potential constraint loss effects. The temperature for the second unclad beam (Un-Clad 4.1.2) was therefore increased to a value close to T_0 for Plate 100 (-95^{o}C). This level was maintained for most of the test, but in the final 5 seconds it increased slightly and fracture occurred at -90.4^{o}C, well into the non-linear range of the M vs. CMOD plot.(Fig. 4.12). Clad 4.2.1 was tested at nominally the same temperature as Un-Clad 4 1.2 to allow a direct comparison of the two configurations, and fractured at -93.2^{o}C. Clad 4 2.2 was tested at -75°C. The values of test temperature, bending moment and CMOD at fracture are summarized in Table 4.2. In all four tests the entire beam fractured, but the test instrumentation did not provide any evidence to indicate whether initiation took place at the shallow or deep flaw tip. It must nevertheless be noted that in contrast to the shallow tip, the lower tip had no fatigue pre-crack.

Table 4.2 Failure conditions for the embedded flaw tests

Test	Temperature* °C	Total Load kN	CMOD mm	Moment** kN-m
Unclad 4.1.1	-128.1	449	0.056	57
Unclad 4.1.2	-90.4	951	0.378	121
Clad 4.2.1	-93.2	853	0.262	108
Clad 4.2.2	-77.2	967	0.729	123

*) recorded temperature for the shallow tip
**) assuming a moment arm of 254 mm

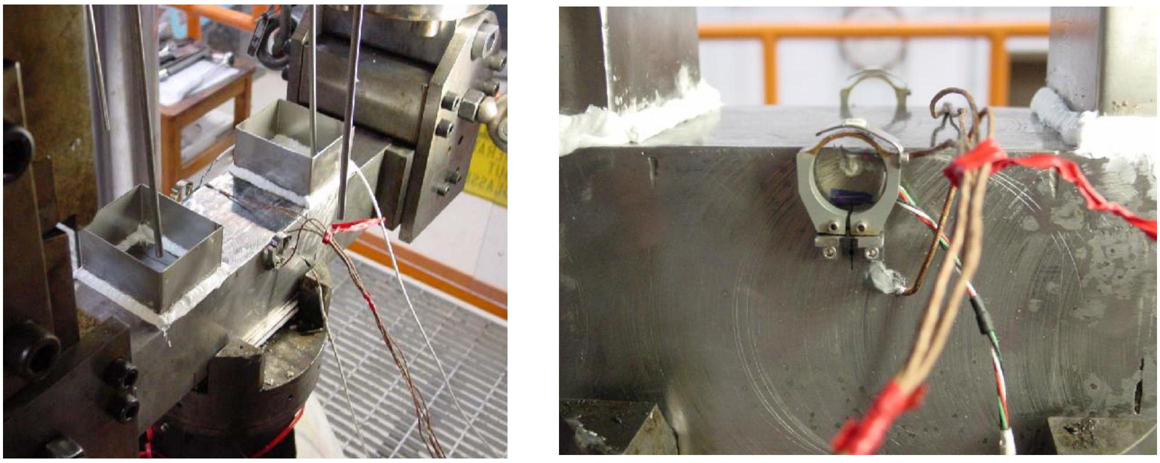

Figure 4.11: Details of the embedded flaw beam test set-up: a) the cooling system and b) the CMOD gages attached to side of the beam.

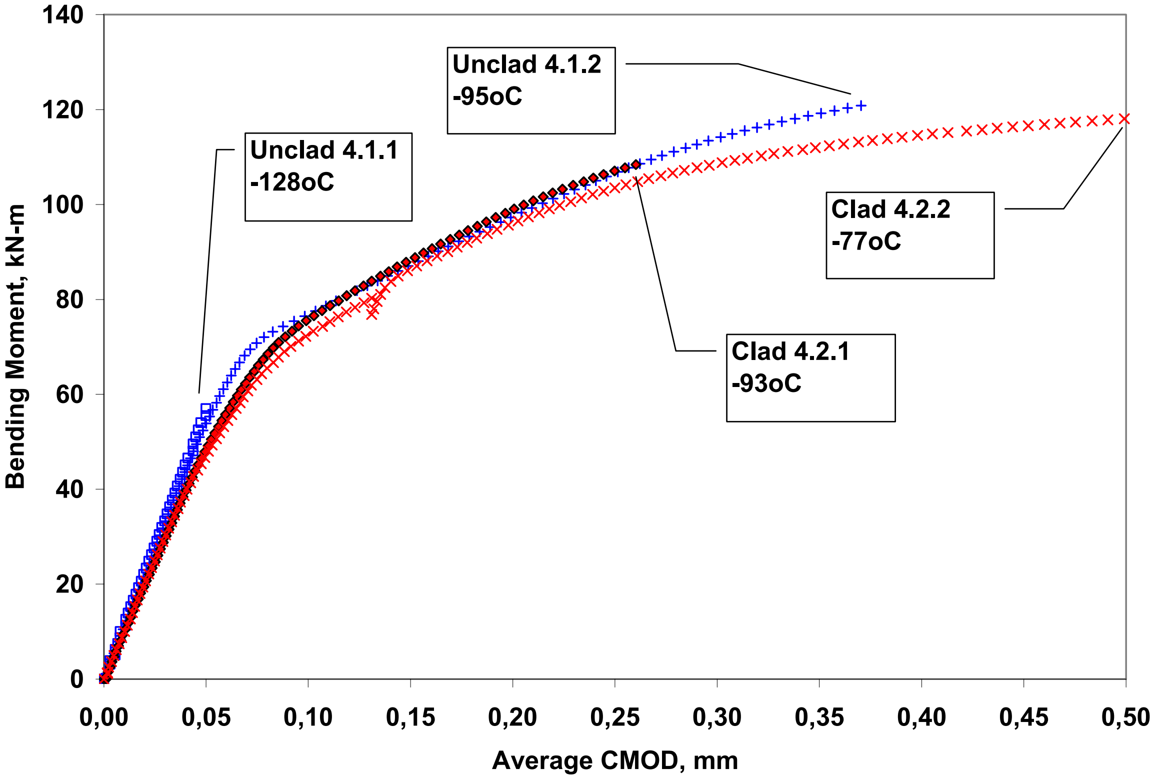

Figure 4.12: Moment vs. CMOD data from the four embedded flaw uniaxial tests.

4.2.3 Post-Test Fractography

Figures 4.13 and 4.14 show the fracture surfaces of all four beams. For the unclad beams the mode of fracture was characterised as cleavage (Fig. 4.13). For the clad beams fracture was likewise determined to have been cleavage in the plate and HAZ material and unstable tearing in the clad (Fig.4.14). In general no discrete fracture initiation sites were found and it is presumed that this occurred at several sites along the crack fronts simultaneously.

4.2.4 Second Series of Embedded Flaw Tests

Based on the success of the initial series of embedded flaw tests, it was decided to fabricate and test a further set of 6 test pieces so as to obtain a statistically significant set of results. The design corresponds to that used in the 1st series of tests on clad beams, as discussed above. The material for these test pieces was taken from a further section of the PV-RUF vessel[3], which was sent to the JRC by ORNL. JRC then arranged the sectioning the PVRUF shell segment, the insertion of the EMD slot and the electron beam welding of the extension arms on the 6 beams. This work was completed at the beginning of 2005 and further details are available in the fabrication report [30]. It is planned that these beams will be tested in 2006, and that the results will then be circulated to the NESC-IV participants.

---

[3] Charpy tests on samples taken from this section of the PVRUF vessel were performed by JRC. The results indicated a similar transition behaviour as Plate 200

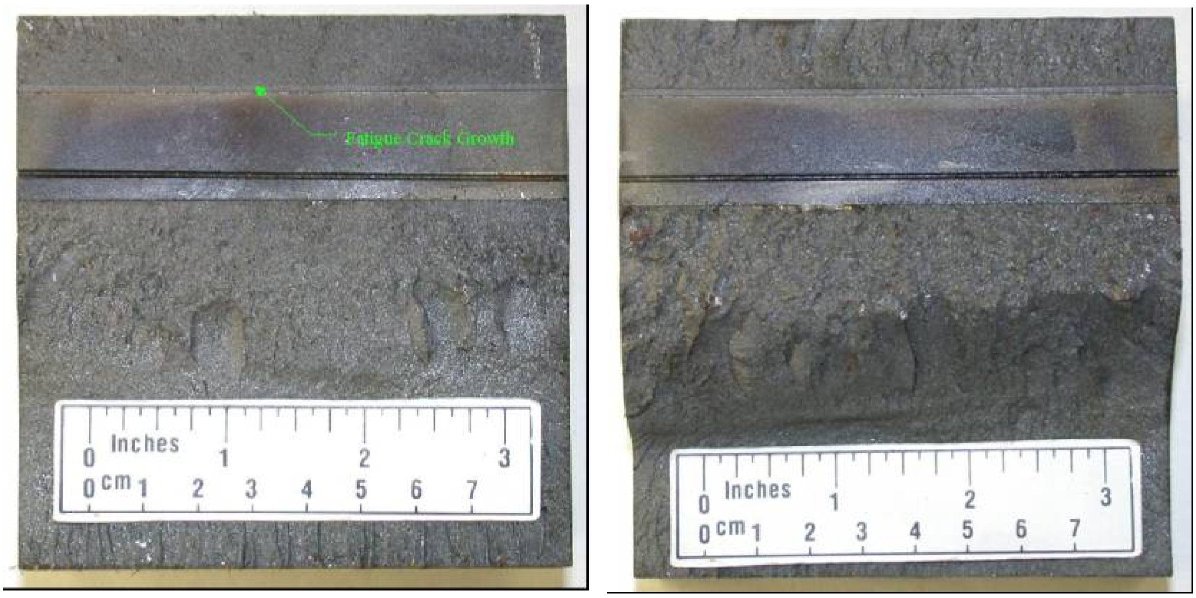

Figure 4.13: Fracture surface of specimen Unclad 4 1.1 (-128°C) and Unclad 4.1.2 (-90°C) – left and right respectively.

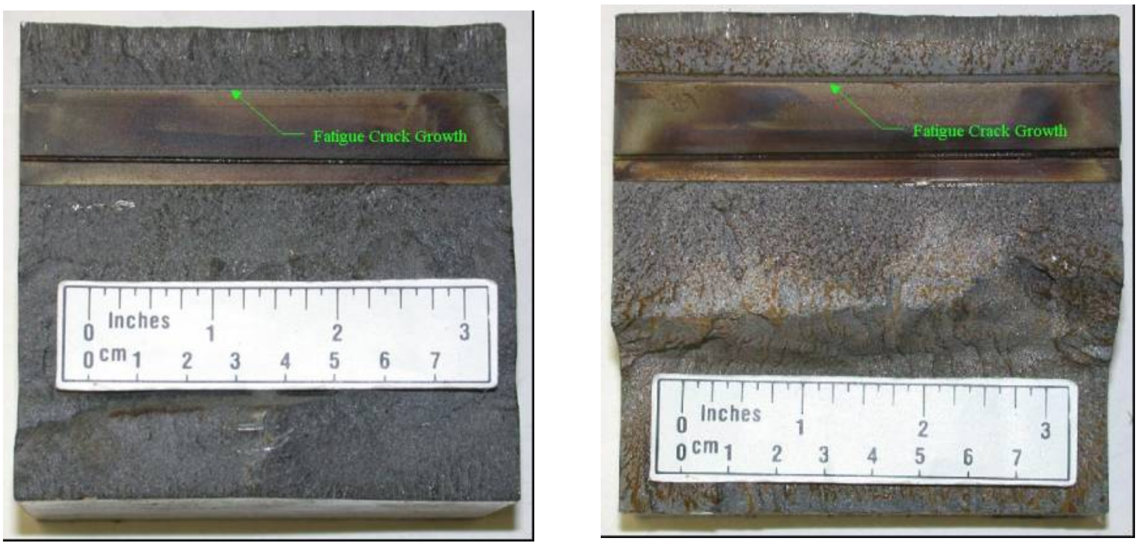

Figure 4.14: Fracture surface of specimen Clad 4 2.1 (-93°C) and Clad 4.2.2 (-77°C) – left and right respectively.

5 FRACTURE ANALYSIS

This chapter provides a summary of the investigations performed by the TG3 stress and fracture analyses task group. The work was performed in two parts:

a) Pre-test analyses were performed, leading to recommendations concerning the test temperature conditions for both the biaxial cruciform tests and the uniaxial embedded flaw tests, as well as for the geometry of the embedded flaw test pieces themselves. The results were detailed in the interim report.

b) Post-test analyses were performed on the basis of the Post-Test Problem Definition Documentation circulated in June 2002 [21]. This provided a unified presentation of all the input data required for structural post-test analysis of both cruciform bend tests for shallow flaws and uniaxial bend tests of embedded flaws; this covered component geometry, defect geometry, loading, mechanical properties and fracture properties. Additionally the material characterization data and associated analyses were compiled in a series of Excel sheets.

5.1 Surface-Breaking Flaws Under Biaxial Bending

5.1.1 Overview of the FE Analyses Performed

a) Det Norsk Veritas AB (DNV)

DNV [31,32] analysed the cruciform beam specimen using a 3-D FE model with the ABAQUS FE code. The materials (weld, base and cladding) are assumed to be elastic-plastic following a Ramberg-Osgood model fitted to the hardening behaviour of the uniaxial test results. It was assumed that the materials obeyed the von Mises flow criterion with its associated flow rule and isotropic hardening behaviour. Due to symmetry in geometry and load, only one forth of the specimens was modelled. The model consisted of 3610 twenty-node solid elements, which were fine enough around the crack front to resolve the crack-tip fields at the load level of interest. Contact elements were used between the specimen and the loading platen. The assumed test temperature was –40°C. To consider the cladding residual stresses in the FEM analysis, the FEM model is assumed to be stress free at 399°C, experiencing cooling down to ambient temperature, at which the crack is inserted in the model. After that, the model is cooled down to the test temperature (around -40°C). The general behaviour of the model was verified by comparing the predicted load-CMOD response with that of the tests. It is noted that the FE model response is rather sensitive to mechanical properties data used.

To calculate the crack-tip constraint parameter Q the SSY reference field was obtained by imposing a K-field on the remote boundary of a standard boundary-layer model (a semi-cracked annulus). The radius of the boundary layer model needs to be about 100 times the plastic zone size due to the imposed K-field. The FE model used for this consisted of 640 eight-noded plane strain elements arranged in 40 concentric rings focused toward the crack tip. The reference stress parameters were computed for all three materials; base, cladding and weld materials. These reference values are evaluated at the distance $r/J(\sigma_Y) = 2$ ahead of the crack tip. The constraint parameter Q were evaluated for different crack configurations at a load level of $K = 100$ MPa√m (J=43 kN/m); values are reported in Table 5.1. It was concluded that the constraint conditions are effectively similar in the cruciform test and in the deep SE(B) specimen at the cleavage fracture loads. For this crack configuration, the most critical location for crack growth is likely to be in the cladding HAZ, considering both J and Q values

Table 5.1 Values of the constraint parameter Q at K = 100 MPa√m

Crack Geometry	Q
SE(B)	
a/W = 0.10	-0.45
a/W = 0.50	-0.05
Cruciform tests	
At the deepest point	+0.10
In the cladding HAZ	+0.25

b) Oak Ridge National Laboratory

ORNL [33, 34] performed investigations of the surface cracks using an analytical approach for cleavage based on a Weibull stress statistical fracture model. In the ORNL calculation of the Weibull stress the hydrostatic stress is used as the effective stress in order to capture the constraint effect due to both shallow flaw effects and biaxial. After the Weibull stress model was calibrated, the large scale beams analyses were carried out. The assumed test temperature was –40°C. Six test results of the cruciform beams tested to failure are compared with the numerical outcome. The cumulative failure probability of the cruciform beams is predicted. For comparison with the experiments, a median-rank order statistics of the experimental data is used. The prediction lies within 90% confidence limits of the experimental data. The model was also used to predict the relative contributions of the different factors affecting the level of constraint:

SSY condition, uniaxial loading	$T_{0,SSY}$	= -70°C
Shallow flaw effect:	$T_{0,0:1}$	= -128°C
Biaxial effect	$T_{0,1:1}$	= -106°C

Further details of the ORNL local approach analyses are given in section 5.1.7 below.

c) MPA Stuttgart (MPA)

MPA [36, 37] conducted a series of FE simulations of the cruciform beam test piece, investigating in particular the crack tip constraint conditions. The mesh had nearly 9000 second order (reduced integration) elements and about 41000 nodes. FE analyses were done with ABAQUS version 6.3-1. For the material behaviour they used stress-strain curves based on the given Ramberg-Osgood-Parameters. The temperature dependence was introduced by the Young's modulus. For the actual analyses only one temperature, T = -40°C, was used. For the test simulation itself, a concentrated load of 265 kN was applied on the end of both the loading arms. All nodes on the upper surface at the end of the loading arm had the same displacement in load direction (realized by using an appropriate constraint condition). The length of the arm was 285.8 mm and therefore the maximum applied bending moment in the analysis is 151.75 kNm which is in the same order of magnitude than the maximum experimentally reached failure moment of 150.7 kNm. A stress-free temperature of 399°C was assumed, so that at the test temperature of –40°C the FE analysis predicts clad tensile stresses of about 140 MPa and low compressive stresses in the HAZ and weld. Due to these residual stresses a crack tip loading of $K_I \leq 20$ MPa√m in the cladding is estimated.

The analysis also considered several constraint parameters:

a) The calculated Q-parameter values indicated that loss of constraint is larger at the HAZ position than at the deepest point.
b) The T-stress calculation of the cruciform specimen was also done with ABAQUS. To avoid any uncertainties coming from thermal strains, an isothermal analysis was carried out at T=-40°C. Elastic behaviour was assumed. In the clad region and near the interface a T-stress of 220 MPa is

calculated, indicating high constraint. Near the deepest point of the crack, the T-stress reduces to about –120 MPa, indicating constraint loss. This result showing an out-of plane loading effect on the T-stress at the clad/HAZ is supported by Sherry et al's calculations [38] for plates under biaxial bending. Further analyses confirmed that with pure in-plane bending, the T-stress values predict constraint loss also at the surface position.

c) A further parameter, the quotient of multiaxiality q, was also examined It predicts strong loss of constraint near the HAZ interface and higher constraint at the deepest point. "q" can be used to predict stable or unstable crack growth. However since the beams all failed in cleavage, it is not considered further here.

d) Fraunhofer Institut für Werkstoffmechanik (IWM)

IWM [39] performed a detailed FE analysis using ABAQUS software. The materials properties for the clad, the HAZ and the weld were as described in the Problem Definition Document. Due to symmetry, the model represents only a quarter of the specimen and consisted of 8914 20-node elements and 43320 nodes. The numerical simulation of the test was performed following the sequence of steps:

1. Cooling the specimen from 400°C (stress free state) to 20°C.
2. Introducing the crack (by releasing respective nodes).
3. Cooling the specimen from 20°C to the test temperature of -40°C.
4. Load application with the biaxiality ratio of 1:1.

The analysis considered the distribution over the crack front of crack driving force, T-stress and the stress triaxiality factor h for both biaxial and uniaxial loading. From the results the following conclusions were drawn:

- The calculated average K_{Jc} values of the cruciform specimens and the respective reference temperature T_o are consistent with the Master Curve evaluation corresponding to the T_o value of -73°C for the high-constraint 1T C(T) specimens.
- Concerning the crack tip constraint, the T-stress at the HAZ–weld interface position on the crack front indicated high constraint comparable to that for a C(T)-specimen. Hence, fracture toughness values are expected as for high constraint C(T) specimens despite the shallow flaw.
- The T-stress at biaxial loading seems not to adequately characterize the crack tip constraint. Considering the position of the calculated peaks in the crack driving force and T-stress on the crack front, fracture would be predicted to start in the HAZ, whereas the experimental results revealed failure initiation both in the HAZ and the weld material below. This feature can be properly explained when considering the constraint level in terms of the triaxiality factor h.
- The deficiency of the T-stress based concept to describe the crack behaviour under biaxial loading conditions is confirmed by the analysis of the specimen subjected to uniaxial bending. In this case both constraint parameters (T-stress and h) revealed similar trends, and their use would lead to a similar prediction of the crack initiation, namely starting at the crack center.

e) Institute for Nuclear Research Pitesti (INR)

INR Pitesti [40] performed finite element crack analyses with the FEA-Crack 2.6 software, which works with WARP3D for 3D fracture mechanics analysis. Only a ¼ of cruciform component was modelled using 4666 nodes and 954 "20 node brick" elements. Only the weld mechanical properties were considered, due to limitations in FEA-Crack for introducing the clad and HAZ layer. The main parameters calculated were CMOD and the crack driving force K_J over the crack front. These values were evaluated in relation to the Master Curve using a FAD type approach. Overall it was concluded:

- The load-CMOD responses of all cruciform tests are reasonably predicted by FE analyses made for a temperature of -40°C;

- The highest values of K_J are obtained at a crack angle of 11.5° below the surface, not at deepest point;
- The K_J values from FEA at deepest points and the highest values fit well with those from the standard master curves (T_0= -78°C);
- The FAD analysis using the Master curve mean value for K_{mat} gives good predictions for PVR 2, 5 and 6 but is non-conservative for PVR 1 and 3.

5.1.2 Comparison of Crack Tip Driving force Estimates

The post-test fracture analysis of the biaxial tests is not straightforward on account of the need to consider the following factors:

- the elasto-plastic behaviour of 3 distinct material zones (clad, HAZ and weld) and their stress-strain properties
- the residual stress induced by the mismatch between the thermal expansion properties of the austenitic clad and the ferritic weld (simulated in this case by imposing a stress-free temperature of 400°C)
- use of a detailed 3-D FE model - a typical example is shown in Fig. 5.1.

As an initial check on the performance of the FE models, the predicted applied moment vs. CMOD curves were compared with the data from the cruciform beam tests themselves (Fig. 5.2). All four models (DNV, IWM, INR and MPA) were found to provide accurate representations of the physical behaviour of the test pieces.

Concerning the crack tip behaviour, the focus in the first instance is on the stress intensity factor K (calculated from the FE-computed J value using the standard plain strain conversion formula). The nature of the flaw and the applied loading mean that the value of K is not constant over the crack front. The cracked-body FE analyses show that Kj value in the HAZ region is greater than that at the root or apex of the crack. As indicated by the IWM results (Fig. 5.3), this difference becomes more pronounced as load is increased and amounts to 20% for an applied bending moment of 150 kN.m (the maximum value observed in the biaxial tests themselves). Fig. 5.4 (again from the IWM data) shows the predicted increase in K at the two positions as the applied moment is increased.

To compare the results of the different FE analyses, two locations have been selected: the middle of the HAZ and the deepest point or apex of the flaw. The average values for these locations are reported in Table 5.2[4]. Figs. 5.5 and 5.6 compare the values from the different analyses. The variation is modest, with a standard deviation at the highest bending moment level of 16 MPa.√m

5.1.3 RT_{NDT} and RT_{To} Assessment

Fig. 5.7 compares the results of cruciform tests with the reference temperature transition curves determined according to the RT_{NDT} and RT_{To} parameters determined for the weld materials (-35° and -74°C respectively, see Fig. 3.19 above). The experimental data points are based on the average Kj values reported in Table 5.2 above. All the points fall above the reference curves, confirming their conservatism.

---

[4] No crack front size correction has been applied to the K values in Table 5.2.

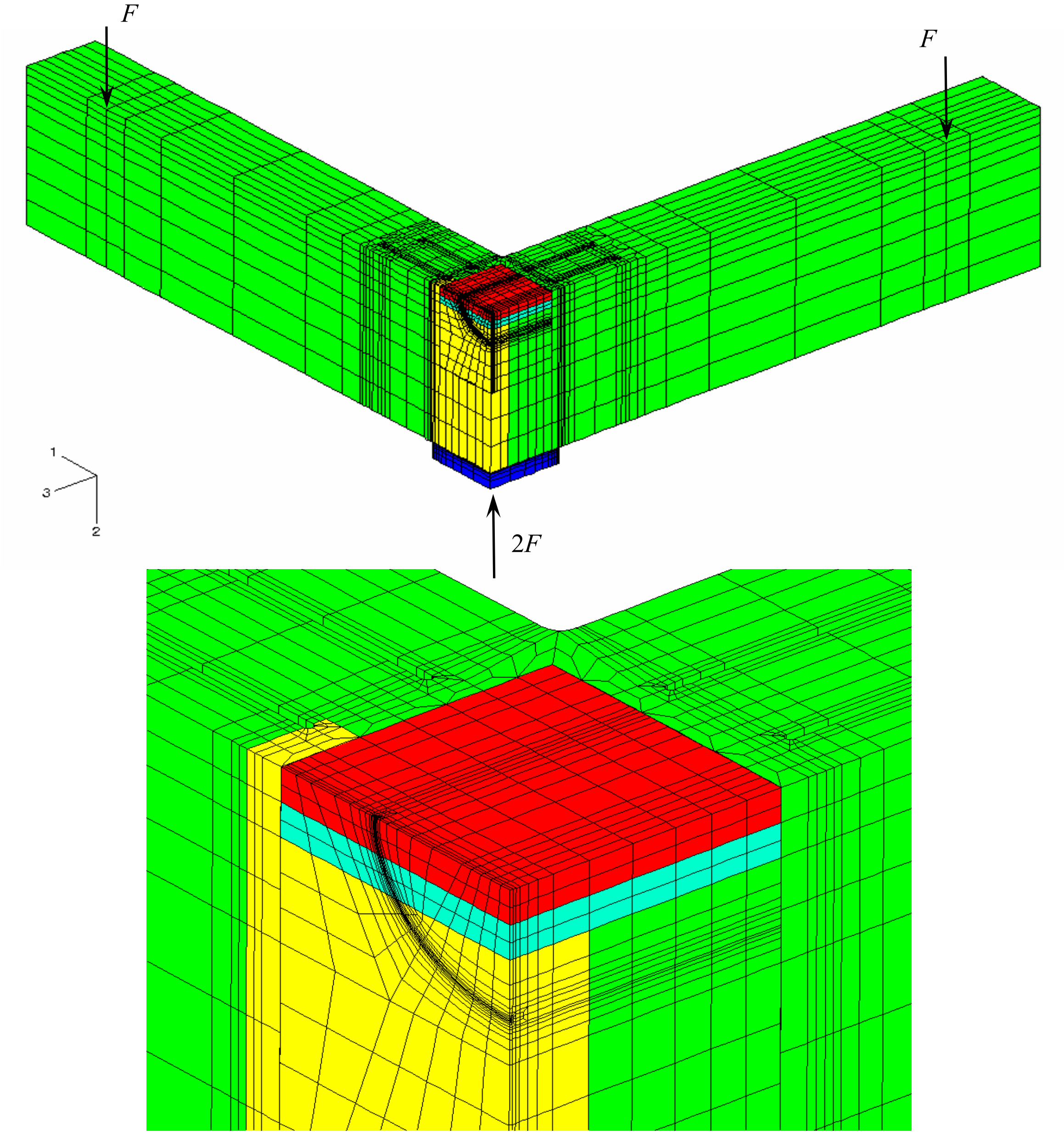

Fig. 5.1. Typical FE model of the cruciform beam test piece showing the clad, HAZ and the semi-elliptical surface flaw [39].

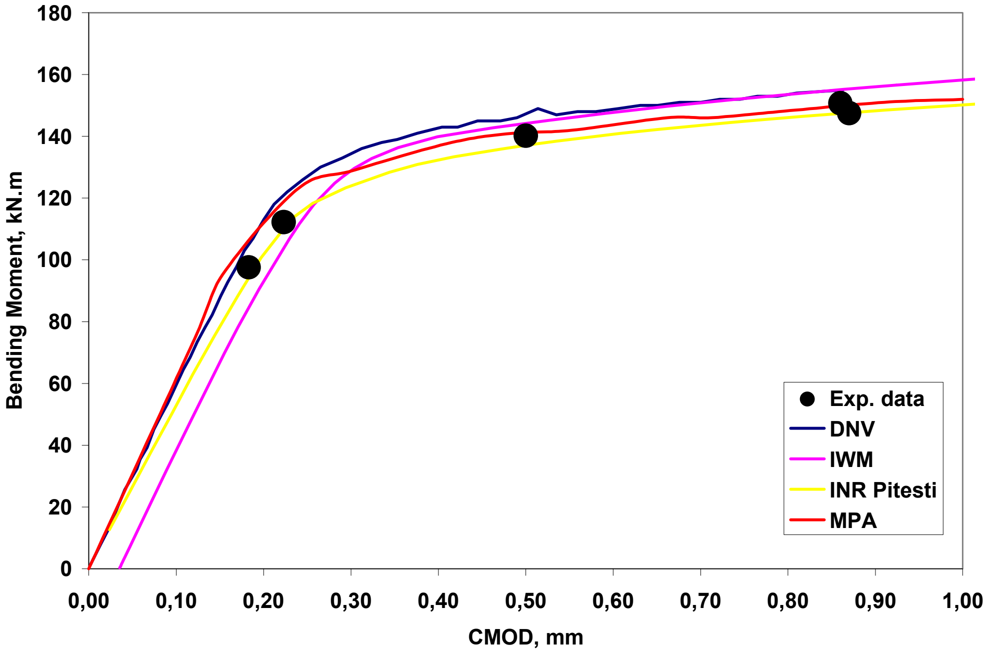

Fig. 5.2 Comparison of the experimental load- CMOD curves with FE predictions.

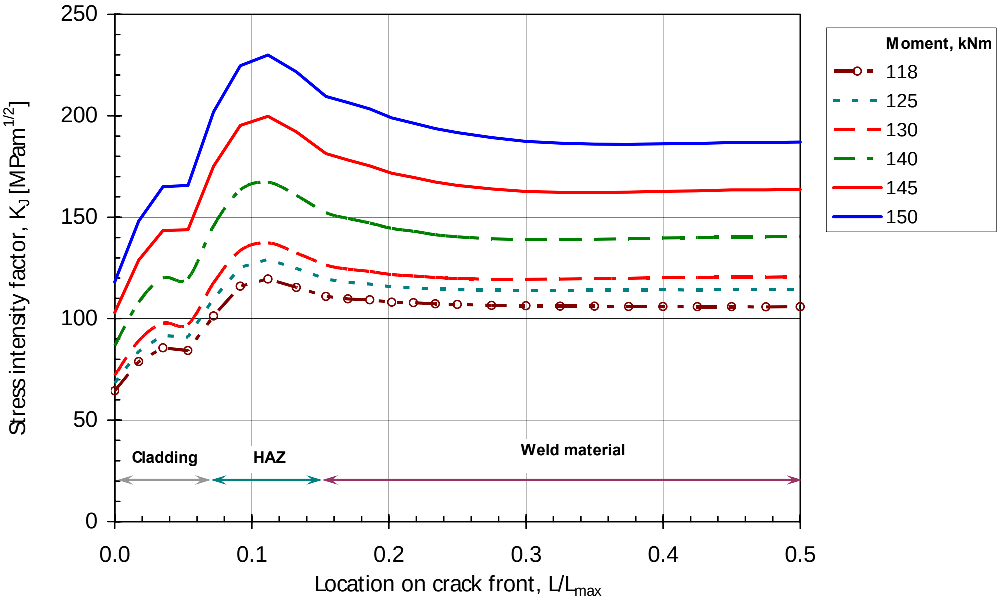

Fig. 5.3 Variation of K_J over the crack front [39]

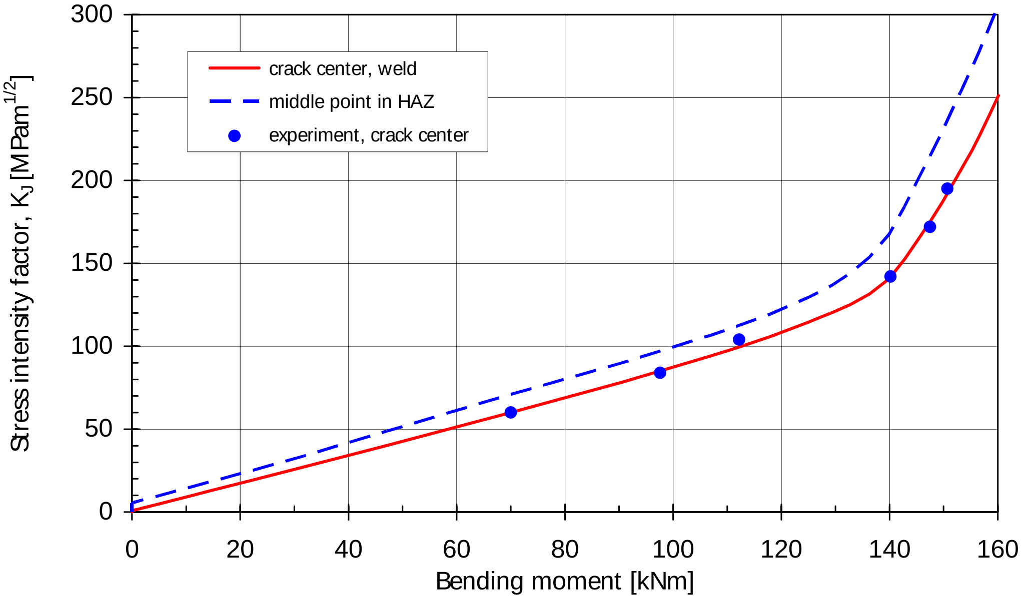

Fig. 5.4 Increase in K with load at the HAZ and deepest points [39]

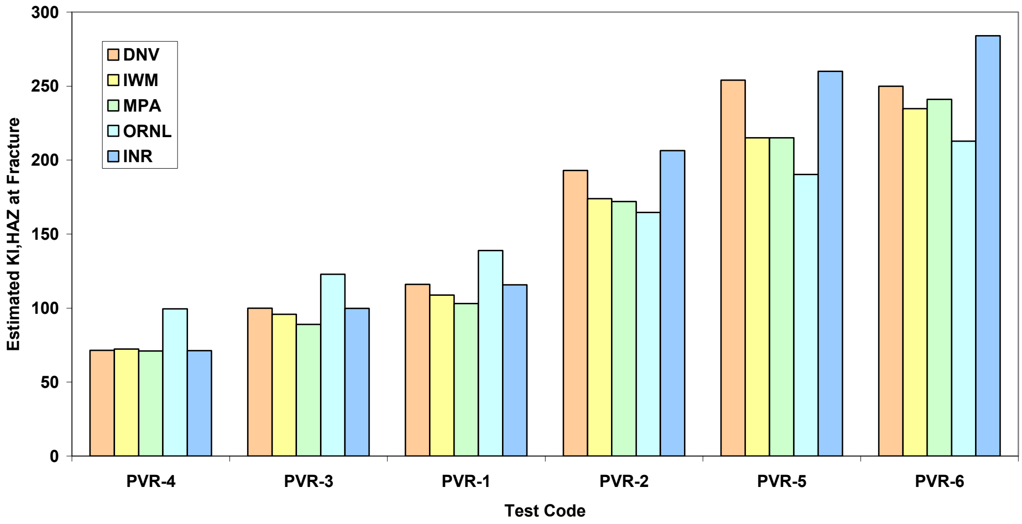

Fig. 5.5 Comparison of the K values calculated for the HAZ position in the biaxial bend beam test pieces.

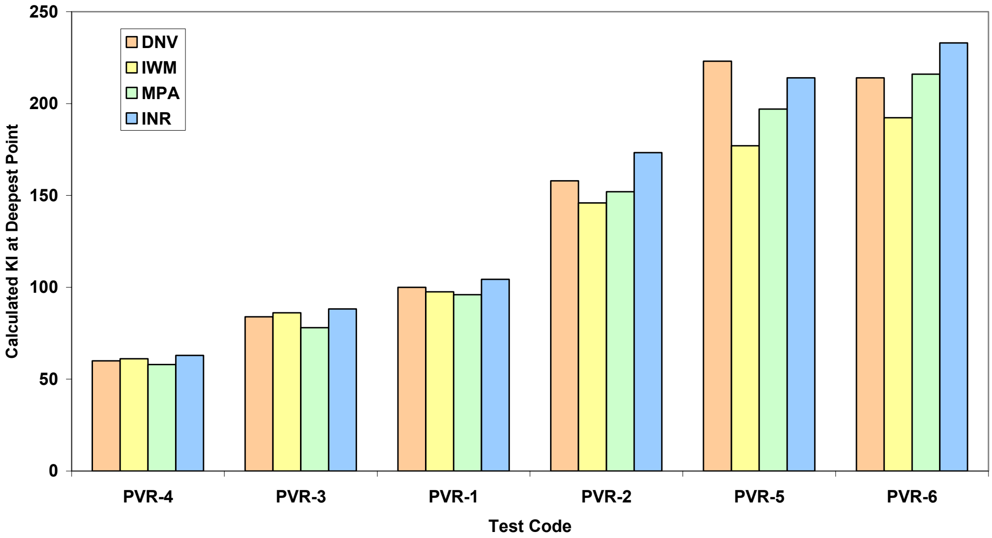

Fig. 5.6 Comparison of the K values calculated for the deepest point position of the surface-breaking flaw in the biaxial bend beam test pieces.

Table 5.2 Comparison of the K values calculated for the HAZ and deepest point positions at the fracture load in the biaxial beam tests.

Test	Temp	Moment	DNV	IWM	MPA	ORNL	INR	Average	St. Dev
					K values (HAZ), MPa√m				
PVR4	-55	77	71	72	71	100	71	79	14
PVR-3	-41	97,6	100	96	89	123	100	102	15
PVR-1	-40	112,2	116	109	103	139	116	117	16
PVR-2	-38	140,2	193	174	172	165	206	176	12
PVR-5	-33	147,5	254	215	215	190	260	219	26
PVR-6	-35	150,7	250	235	241	213	284	235	16
					K values (deepest point), MPa√m				
PVR4	-55	77,0	60	61	58	-	63	60	2
PVR-3	-41	97,6	84	86	78	-	88	82	6
PVR-1	-40	112,2	100	98	96	-	104	97	1
PVR-2	-38	140,2	158	146	152	-	173	149	4
PVR-5	-33	147,5	223	177	197	-	214	187	14
PVR-6	-35	150,7	214	192	216	-	233	204	17

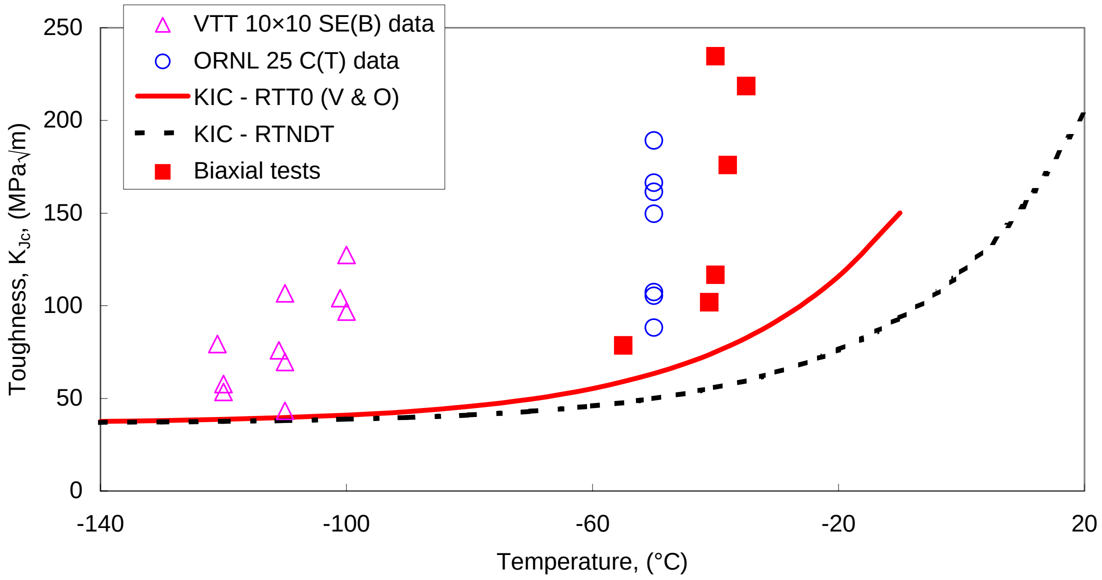

Fig. 5.7 Values of $K_{j,max}$ from the biaxial tests compared with the RT_{NDT} and RT_{To} reference curves for the PVRUF weld

5.1.4 Master Curve Assessment

This section examines the application of the Master Curve methodology, following the general approach for flaws in components as described by Wallin [41]. The role of constraint is however covered separately in section 5.1.5. Two variations are considered:

a) assessment based on the peak K_I value i.e. in the HAZ, without any consideration of crack front length correction, and

b) an effective K value (K_{Ieff},) as defined by Wallin, which provides for a crack front size correction when Kj varies over the crack front:

$$K_{Ieff} = \left[\int_0^s \left(\frac{K_I(s) - K_{\min}}{K_o(s) - K_{\min}} \right)^4 \frac{ds}{B_o} \right]^{1/4} (K_o - K_{\min}) + K_{miin} \qquad (5.1)$$

Here s denotes the path along the crack front. In this approach the size correction is implicitly accounted for; B_o = 25 mm is used as a reference.

In both cases, given that the variation in Kj with applied load is known from the FE analysis, the Master Curve approach can be used to provide a cumulative probability of cleavage initiation as a function of load.

$$P_f = 1 - \exp\left[\int_0^s \left(\frac{K_I(s) - K_{\min}}{K_o(s) - K_{\min}} \right)^4 \frac{ds}{B_o} \right] \qquad (5.2)$$

This is then compared with the experimental data from the biaxial bend tests by means of the rank order function:

$$P_{f,i} = \frac{i - 0.3}{N + 0.4} \qquad (5.3)$$

where “i” is the test number ranked from the lowest to the highest experimental fracture load and N is the total number of tests.

The calibration of Master Curve and the T_o parameter has been described in materials characterization section 3 above. Relevant values of T_o for the PVRUF weld material are summarized in Table 3.8.

a) Assessment based on $K_{I,max}$

The $K_{I,max}$ values are taken directly from Table 5.2 for the HAZ location. Fig. 5.8 compares these data with the 5, 50 and 95% cleavage probability Master Curves, based on the standard high constraint T_o estimate of -74°C. The data points lie within the band determined by the 5% and 95% Master Curves. Considerable scatter is observed. For test PVR-4, which failed at the lowest load, the Kj value falls just inside the 5% Master curve. On the other hand the values for tests PVR-5 and PVR-6, which exhibited the highest bending moment, lie on or slightly above the 95% Master curve. When the predicted cumulative failure probability (P_f) values are compared with the rank-ordered experimental data, an analogous picture emerges (Fig. 5.9), with three of the six tests failing at lower loads than would have been expected based on this best-estimate approach. Overall the results provide evidence that the biaxial loading counteracted the shallow flaw, constraint loss effect.

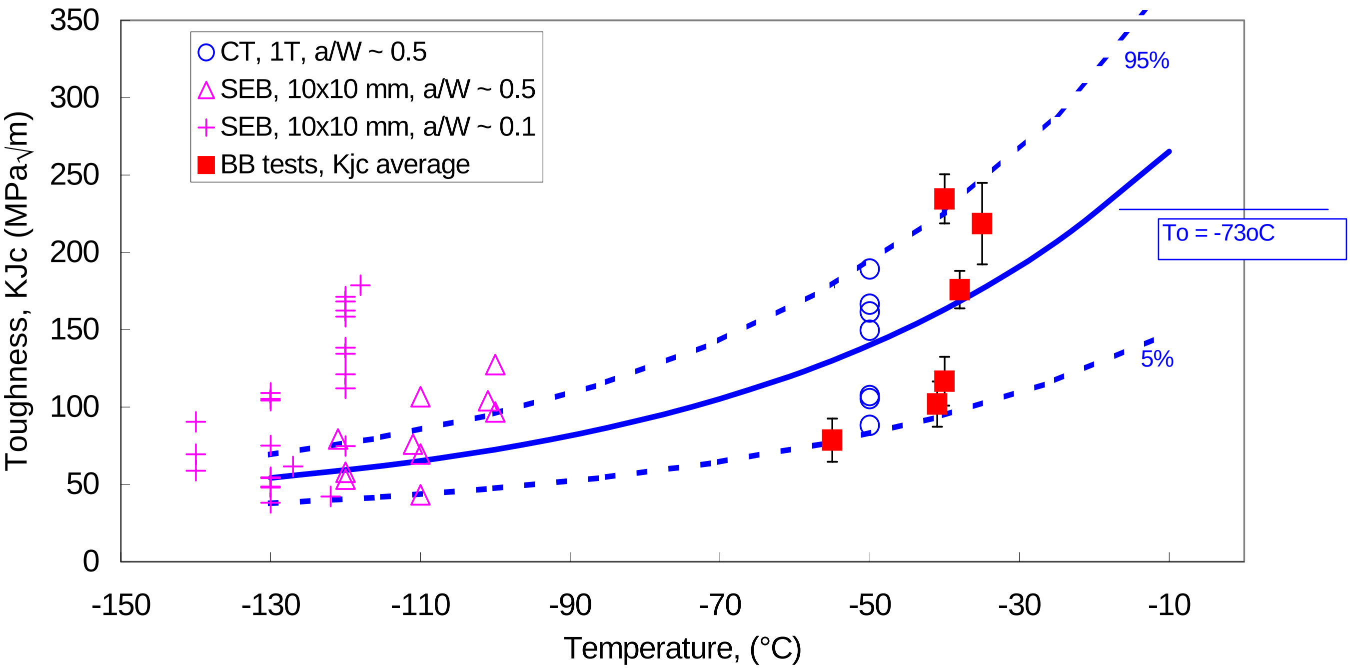

Fig. 5.8 Biaxial tests: average calculated values of maximum K_J (HAZ position) compared with the standard Master Curve.

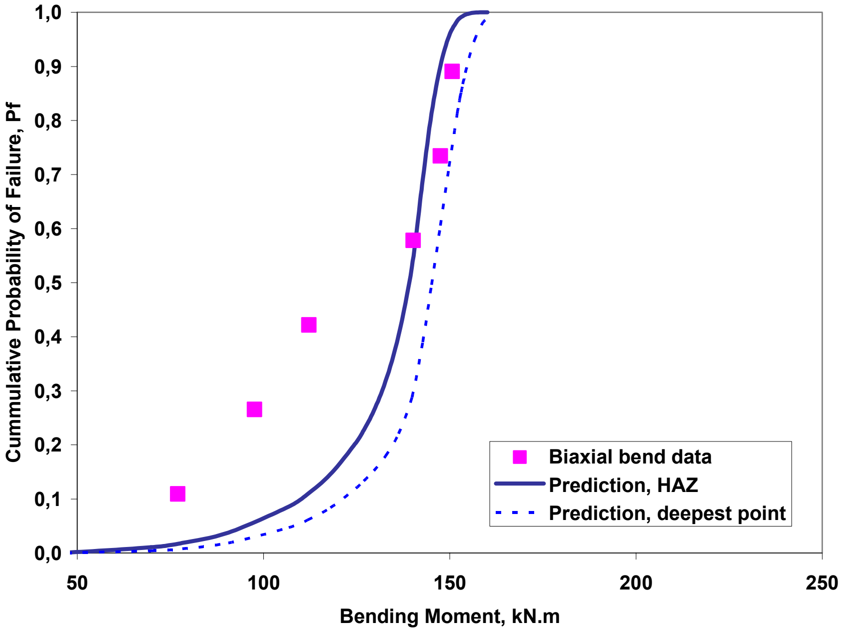

Fig. 5.9 Cumulative probability of fracture curve derived using the maximum K_j parameter compared with experimental data.

b) Assessment based on $K_{I,eff}$

The results of the IWM analyses [39] detailing the variation of Kj over the crack front were used to calculate $K_{I,eff}$. This required integration of eqn.(5.1) above. A simple rectangular integration rule was used, which is expected to be fairly reliable since the function is relatively smooth. The K_{Ieff} values corresponding to the fracture load in each of the tests are compared the maximum value of Kj (at the HAZ) and that at the deepest point in Fig. 5.10. For higher loads K_{Ieff} is substantially less than the K_{Imax} since this value is restricted to a fairly narrow range just below the free surface. Fig. 5.11 shows the $K_{J,eff}$ values plotted with the Master Curve. The use of this parameter is seen to slightly improve the agreement, since the range of the calculated K values is decreased.

5.1.5 Constraint Estimation Parameters

Several investigations examined the role of constraint, focusing on parameters such as T-stress [42, 43] and Q [44, 45]. The following summarizes the findings, considering also that, as discussed above, the biaxial tests results indicate that the constraint increase effect due to biaxial loading suppresses the shallow flaw constraint loss effect at low loads, whereas at high loads the constraint loss effect may predominate.

a) T-stress

MPA and IWM evaluated the elastic T-stress parameter for the semi-elliptic flaw from their FE models. Fig. 5.12 shows the trend of the normalized T-stress (T-stress/σ_y) at the HAZ and deepest point positions as a function of applied bending load. The MPA predictions (only available for the K = 100 MPa√m level) are in agreement with those from IWM, and predict a high level of constraint in the near-surface region of the crack front, but some constraint loss at the deepest point. This result is broadly in agreement with the experimental observations i.e. that the fracture occurred at loads consistent with high constraint fracture data and that the location of the identified initiation sites was predominantly in the near surface part of the crack front. The predicted value of normalized T-stress of 0.5 at fracture corresponds with that estimated for standard deep notch CT specimens. It is worth noting that if only uniaxial loading is considered, the T-stress analysis predicts strong loss of constraint at both the HAZ and deepest point positions (Fig. 5.13).

Since two-parameter constraint-based fracture assessment methods using T-stress are formulated mainly for constraint loss conditions i.e for T-stress/$\sigma_Y < 0$ and consider explicitly only the in-plane constraint parallel to the crack surface, any increase in constraint induced under biaxial loading with an out-of-plane component is not accounted for. Fig. 5.14 shows the variation of T_o with normalized T-stress as given by the models due to Wallin [46], Sherry et al [28] and Gao et al [29][5].

a) Q-parameter

The Q parameter is expected to provide a more accurate estimate of constraint level than the T-stress at loads for which elastic-plastic conditions prevail. Both MPA and DNV studied the variation of the Q parameter over the crack front. In both cases the formulation of Q was based on the crack opening stress, σ_1:

$$Q = \frac{\sigma_1 - (\sigma_1)_{SSY,T=0}}{\sigma_0} \tag{5.4}$$

where $(\sigma_{yy})_{SSY,T=0}$ is the stress opening the crack for the small-scale yielding (SSY) solution with $T_{stress} = 0$ and σ_0 is the reference stress in the Ramberg-Osgood material model. These stresses are evaluated at a distance $r = 2J/\sigma_o$ ahead of the crack tip. The Q values determined using this definition based on crack opening stress σ_1 are not expected to be sensitive to the out-of-plane load introduced in the biaxial bend tests[6]. Fig. 5.15 shows the results available for Q as a function of crack driving force, while Fig. 5.16 compares Q with normalized T-stress values as a function of applied bending moment. For crack driving forces of approximately 100 MPa√m (equivalent to J = 43 kN.m) the Q values are close to or slightly above zero at both the HAZ and the deepest point of the flaw, implying a high overall level of constraint (as shown by DNV, standard deep-notch SENB fracture specimens are predicted to have a Q value of –0.05 at K=100 MPa.√m). The models however predict that Q will decrease at increased loads, and that the decrease will be larger for the near surface region. This implied constraint loss effect at the HAZ does not agree fully with the experimental observations, as discussed above, although the relatively high values of toughness observed in three of the specimens is consistent with hypothesis that constraint is progressively lost with increasing load, notwithstanding the biaxial effect. Overall it is concluded that use of the Q parameter, at least in its σ_1 formulation, may lead to non-conservative predictions of fracture load under biaxial bending.

Two further constraint-related parameters were considered:

a) IWM calculated the triaxiality parameter h, defined as the ratio of the hydrostatic stress to the equivalent stress (σ_h/σ_e). Values in the range 2.5 to 2.7 correspond to high constraint conditions as in a C(T) specimen. Lower values indicate a reduced constraint level.

b) MPA calculated the quotient of multiaxiality, q, where $q = \sigma_e/(\sigma_m.\sqrt{3})$. High constraint is indicated when the ratio of q to critical value $q_c = 0.27$ is approximately equal to unity; when $q/q_c > 1$, constraint loss is predicted.

Table 5.3 summarizes the findings for the HAZ and flaw centre (deepest point) positions for the maximum moment considered (150 kN.m). It is seen that both h and q indicate loss of constraint in

---

[5] Assumed material properties for the PVRUF weld material at -40°C are as follows: elastic modulus, E = 210,000 MPa, Yield strength, Rp0.2%= 653 MPa and work hardening exponent, n = 9.

[6] The use of an alternative Q-stress definition based on the hydrostatic stress was used by Sherry et al [54] to analyse VOCALIST biaxial fracture tests, but this was not investigated in NESC-IV.

the HAZ at this load level, but high constraint at the deepest point. On this basis, one would expect to find the majority of crack initiation sites in the deeper part of the crack. This was not the case and hence these parameters cannot be considered reliable for the present combination of crack geometry and loading.

Table 5.3 Alternative constraint parameters for the surface flaw under a biaxial bend load of 150 kNm

Crack tip Position	q/q_c[1]	h[2]
HAZ	~1.8 *reduced constraint*	~1.9 *reduced constraint*
Deepest point	~0.96 *high constraint*	~2.9 *high constraint*

1) averaged over 1/3 of the ligament
2) taken at a normalized distance of $r\sigma_o/J=2$ from the crack tip.

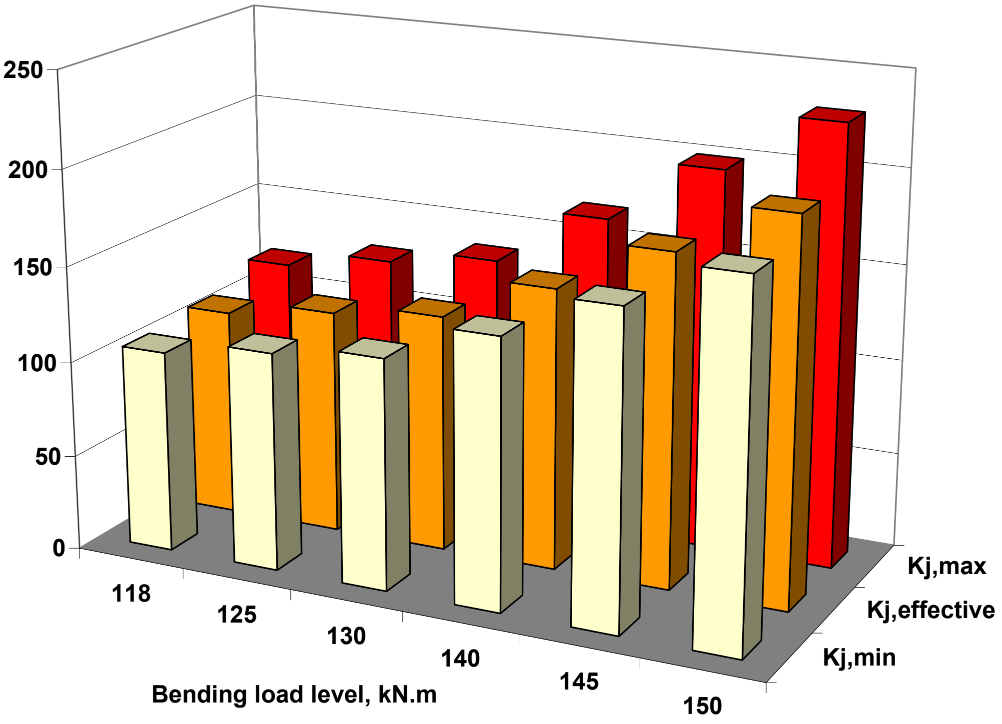

Fig. 5.10 Comparison of the effective crack driving force ($K_{J,eff}$) values from the biaxial tests with the values for the deepest point ($K_{J,min}$) and at the HAZ ($K_{J,max}$)

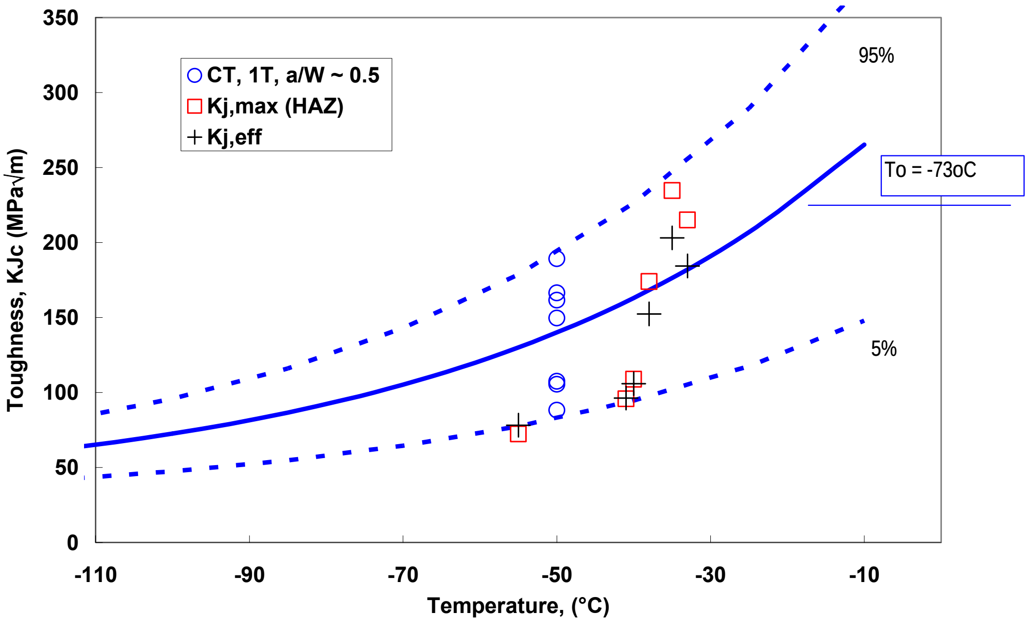

Fig. 5.11 $K_{J,max}$ and $K_{J,eff}$ values for the biaxial tests compared with the standard Master Curve

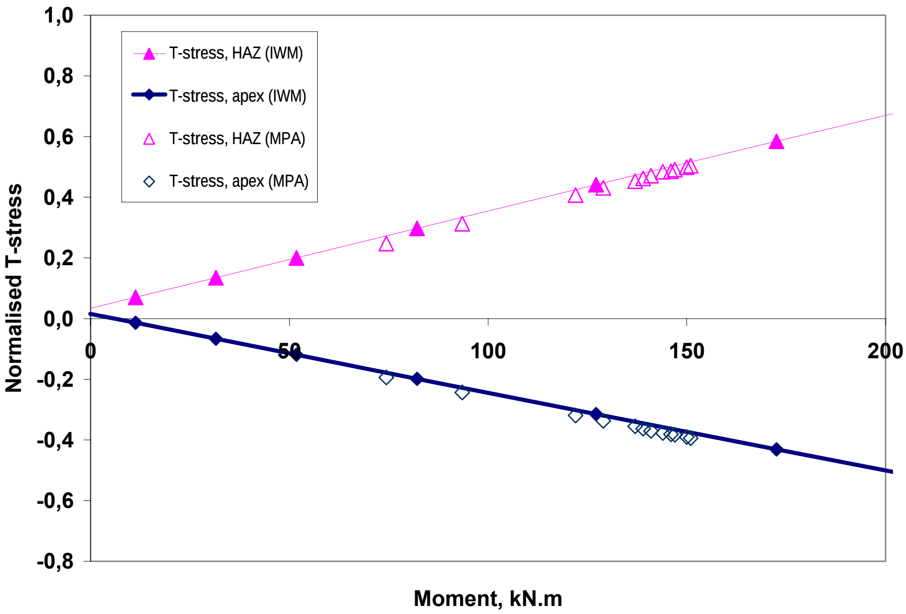

Fig. 5.12 Predicted dependence of T-stress on applied bending load at the HAZ and deepest point locations (MPA [37] & IWM [39]).

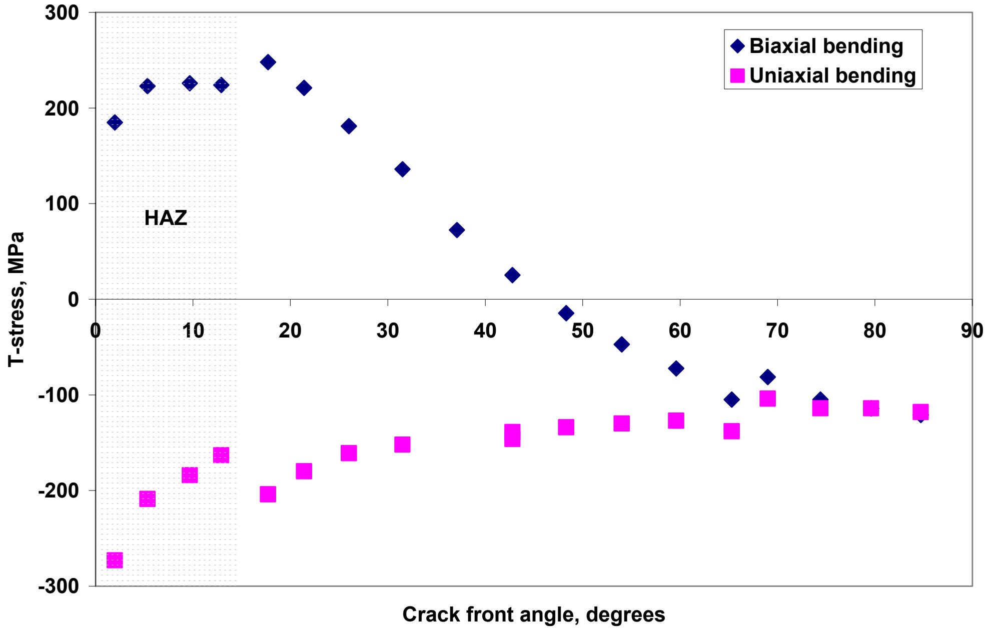

Fig. 5.13 Comparison of the T-stress values over the crack front from the MPA model under biaxial and uniaxial bending.

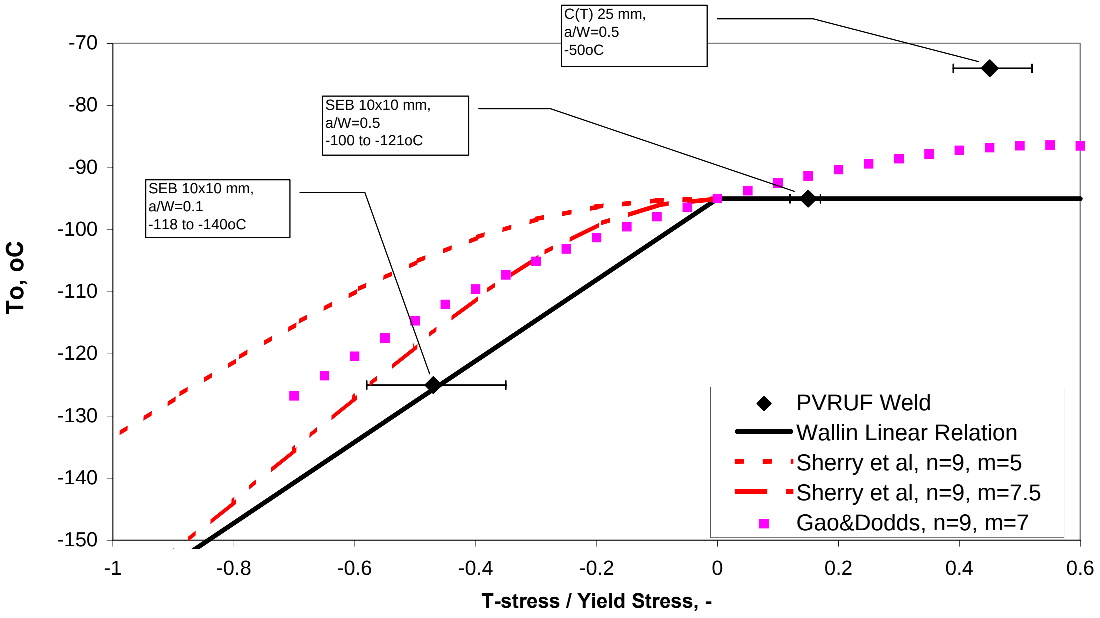

Fig. 5.14 PVRUF weld: variation of the Master Curve T_o parameter with normalised T-stress.

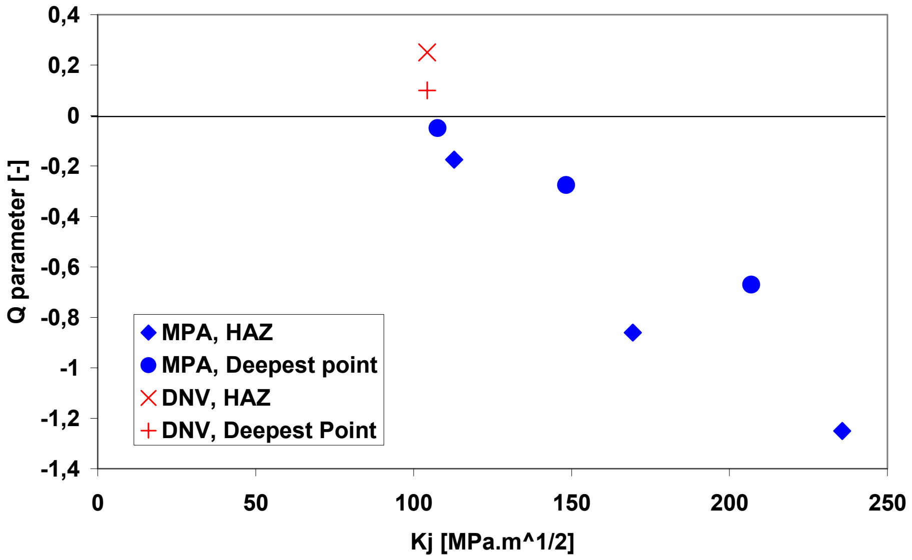

Fig. 5.15 Comparison of the Q values calculated by MPA and DNV for the surface-breaking flaw in the biaxial bend beam test pieces.

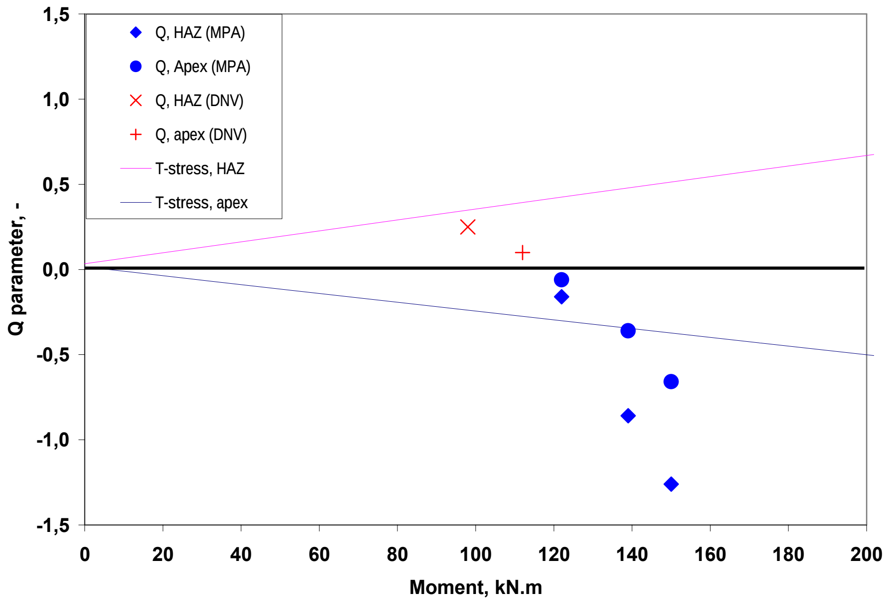

Fig. 5.16 Normalised T-stress and Q vs. applied load

5.1.6 Failure Assessment Diagram (FAD)

DNV analysis applied an R6 FAD approach. The main features were:

a) FEM elastic stresses from un-cracked geometries.

b) Best-estimate fracture toughness values at the test temperature, evaluated from a size-corrected mean Master Curve to the actual crack-front size.

c) Use of the DNV SACC program for calculation of K_r and L_r.

Assuming similar crack-tip situations in the cladding HAZ and at the free surface (no constraint loss effects), this best-estimate approach gives accurate predictions (Fig. 5.17) of fracture event for the three cruciform tests that failed at higher loads. However the three tests that failed at lower loads fall within the FAD, indicating some non-conservatism. Use of a lower bound Master Curve (5%) would be expected to restore the conservatism of the approach. From Fig. 5.17 it is also noted that the maximum L_r value was 0.79, confirming that the tests failed under constrained crack tip yielding conditions and the appropriateness of the test temperature range used.

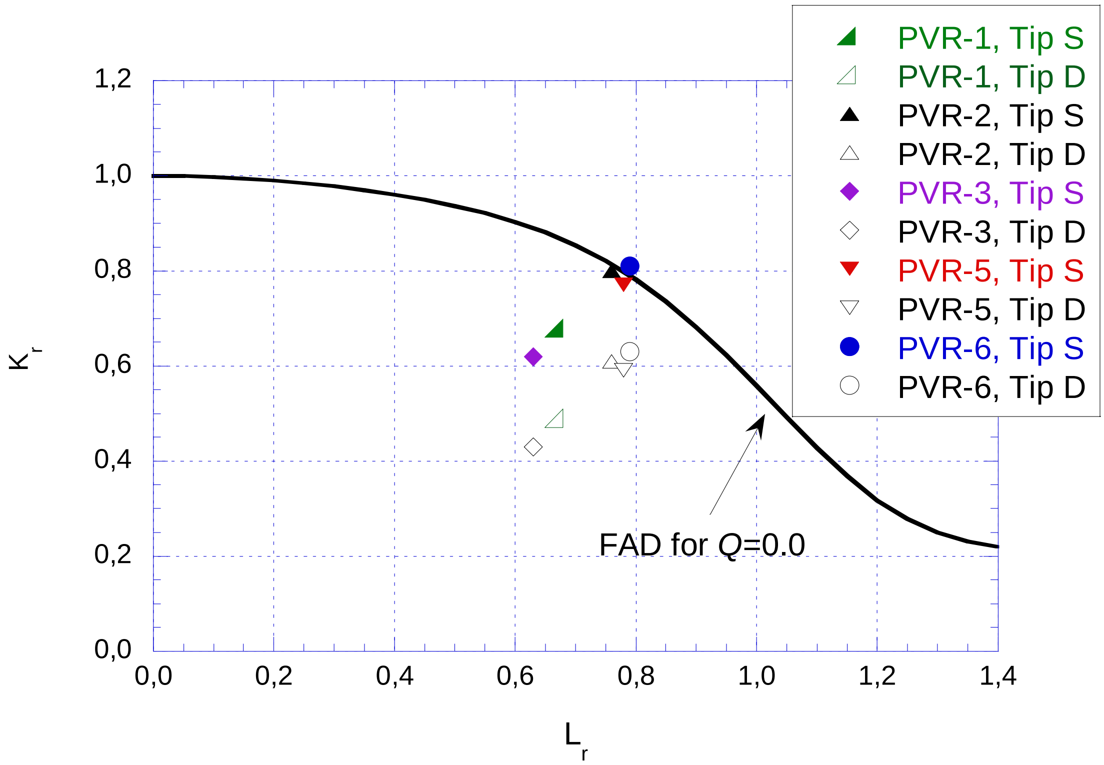

Fig. 5.17 Failure assessment diagram [32] for the biaxial tests using a K_{mat} value from the mean (P_f=0.50) Master Curve.

5.1.7 Weibull Model of Cleavage Fracture Toughness

The effects of biaxial loading on cruciform shallow-flaw fracture toughness data in the lower-transition temperature region were studied by ORNL using a Beremin Weibull methodology [47] that employs a multi-axial form of the *weakest-link* model applicable for a 3-D cracked solid [33,34]. The Weibull stress, σ_w, is characterized as a fracture parameter reflecting the local damage of the material near the crack tip:

$$\sigma_w = \left[\frac{1}{4\pi V_0} \int\limits_{\Omega} \int_0^{2\pi} \int_0^{\pi} \sigma_q^m \sin\varphi \, \mathrm{d}\varphi \; \mathrm{d}\theta \; \mathrm{d}\Omega \right]^{\frac{1}{m}} \tag{5.5}$$

It is evaluated by integration of the equivalent stress, σ_q, over the process zone. In Eq. (1), V_0 is a reference volume; m is the Weibull modulus; θ and φ are curvilinear coordinates for integration of the tensile stress; and Ω denotes the volume of the near-tip fracture process zone, defined as the volume within the contour surface $\sigma_1 \geq \lambda\sigma_0$, where σ_1 is the maximum principal stress and σ_0 is the yield stress. The cut parameter λ is nominally set to 2 to ensure that all material points within the active process zone have undergone plastic deformation [17]. A fracture criterion must be specified to determine the equivalent (tensile) stress, σ_q in Eq. (1), acting on a microcrack included into the fracture process zone. Of the criteria studied in previous investigations, only the hydrostatic stress criterion, where $\sigma_q = I_1/3 = \sigma_H$ (I_1 is the first invariant of the Cauchy stress tensor), showed a consistent response to biaxial loading.

The cumulative probability of failure by transgranular cleavage P_f can be estimated by a three-parameter Weibull distribution of the form:

$$P_f(\sigma_W) = 1 - \exp\left[-\left(\frac{\sigma_W - \sigma_{W,\min}}{\sigma_u - \sigma_{w,\min}} \right)^m \right] \tag{5.6}$$

where the parameters are the Weibull modulus m (shape parameter), the scaling stress (scale parameter) σ_u , and the minimum Weibull stress for cleavage fracture $\sigma_{w\text{-}min}$ (location parameter).

The GRD calibration scheme [35] was used to determine unique values of the Weibull parameters (m, σ_u) by applying toughness data measured under low and high constraint conditions at the crack front. For this calibration the fracture toughness data of SE(B) 1T specimens tested at T=-100°C were used and data sets at the test temperature of the large scale beams T=-40°C are simulated using the transition temperature and the Master Curve. The deep crack model had a transition temperature of T_0 = -88.3°C and the shallow crack model a T_0 = -132.8°C. The finite element calculations are performed with the commercial code ABAQUS. Two different models for each specimen type are constructed: the sharp crack tip models are used to calculate the global behaviour and the J-Integral, the outcome of blunt crack tip models are used for the calculation of the Weibull stresses. The good quality of the calibration is shown in Fig. 5.18.

The six test results of the cruciform beams tested to failure are compared with the numerical outcome of the Weibull model in Fig. 5.19. The cumulative failure probability of the cruciform beams is predicted. For comparison with the experiments, a median-rank order statistics of the experimental data is used. The prediction lies within 90% confidence limits of the experimental data. On this basis the ORNL Weibull model can be considered to reliably predict the fracture behaviour under biaxial loading.

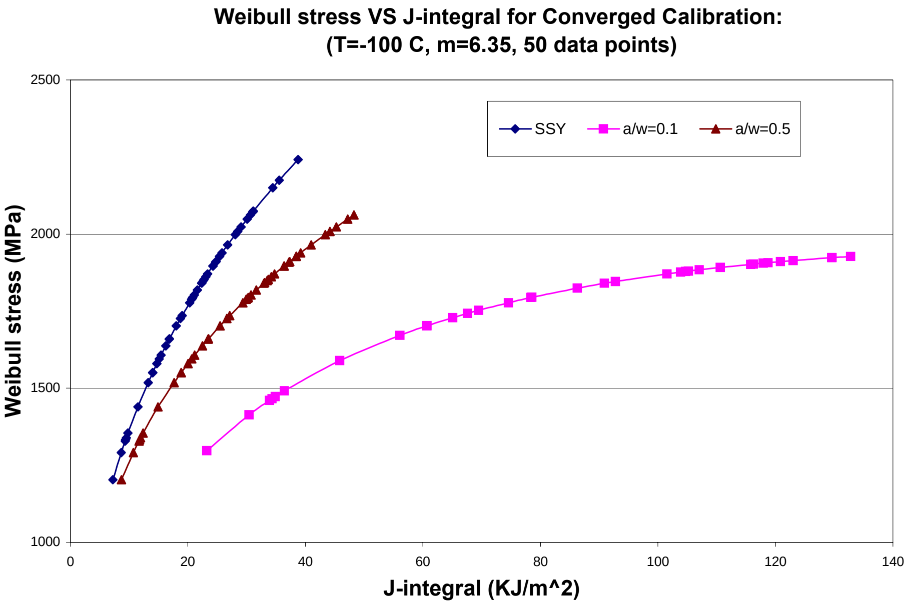

Fig. 5.18 Results of the G-R-D calibration scheme applied by ORNL for the weld material (Weibull stress is defined on the basis on the hydrostatic stress).

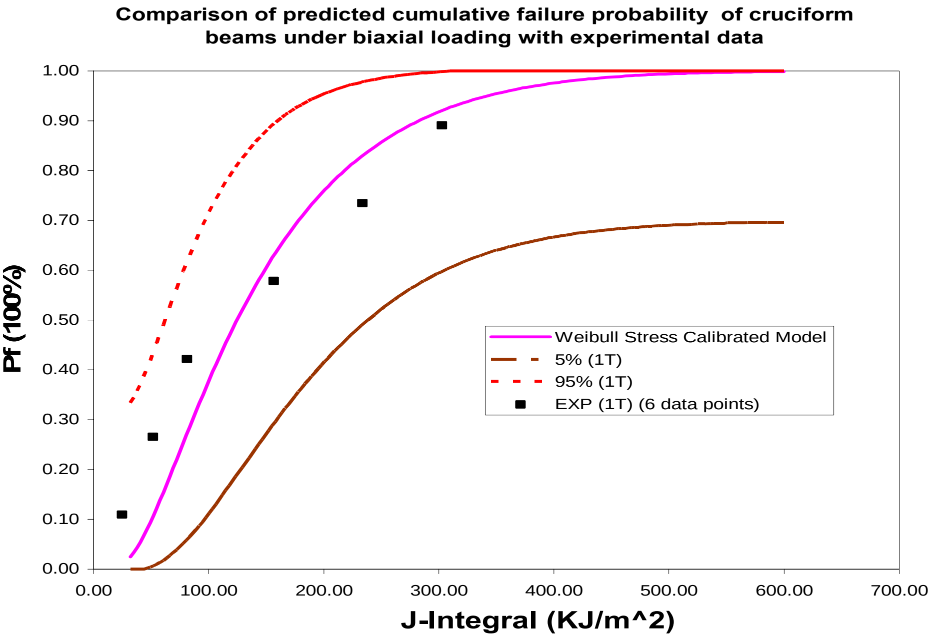

Fig. 5.19 Predicted cumulative failure probability of cruciform beams using the ORNL Weibull Model.

5.1.8 The Prometey Model

CRISM Prometey treated the NESC-IV data with their published procedure [48]. At ORNL 6 cruciform specimens with semi-elliptical surface cracks were tested under biaxial bending. A part of crack front crosses cladding and part of crack front is located in base metal. The coefficient of biaxiality β (here $\beta = P_z/P_y$; P_y is the load perpendicular to the crack plane; P_z is the load acting along the crack front) is equal β=1. The sizes of specimen and crack are W = t = 101.6 mm, 2c = 53.3 mm, a = 19.1 mm, cladding thickness S_{cl} = 5 mm. Test temperature is varied from –55 to –35°C. Additionally 7 standard C(T) specimens with deep crack (a/W≅0.5) were tested at T=–50°C.

According to the proposed procedure, an effective fracture toughness parameter K_{JC}^{eff} is determined on the basis of experimental data on fracture toughness K_{Jc} for specimen with semi-elliptical crack. The parameter K_{JC}^{eff} is calculated from condition of the same probability P_f for specimen with semi-elliptical crack for non-homogeneous ($K_I \neq$const) and homogeneous (K_I=const) distribution of SIF along crack front:

$$K_{JC}^{eff} = \left(\frac{2c}{B_i} \int_0^{\pi/2} (K_I(\varphi) - K_{\min})^4 \sqrt{1-\varepsilon^2 \sin^2 \varphi}\; d\varphi \right)^{1/4} + K_{\min} \qquad (5.7)$$

Here $K_I(\varphi)$ – SIF along crack front at brittle fracture, K_{min}=20 MPa√m, B_i – the semi-elliptical crack front length, $\varepsilon = \sqrt{c^2 - a^2}\,/\,c$, a and c – sizes of semi-axes. In order to treat test results of cruciform specimen by the proposed procedure it is necessary to know the dependence of SIF along crack front and length of the crack front. So, substituting values $K_I(\varphi)$ in the appropriate equations and using value K_{Jc} from NESC-IV data, K_{JC}^{eff} was determined for each cruciform specimen. It should be noted that when calculating K_{JC}^{eff}, the parts of the crack front that cross cladding are excluded from consideration because the brittle fracture probability for austenitic material is zero.

The treatment of test results for standard C(T) specimen by the "Master Curve" concept gives:

T_o=–73.8°C, $K_{IC(med)\ (T=-50oC)}$=140.0 MPa√m.

The treatment of test results of cruciform specimen by the Prometey procedure gives:

T_o=–68.1°C, $K_{IC(med)(T=-50oC)}$=128.7 MPa√m.

Comparison of values of $K_{IC(med)\ (T=-50oC)}$ for biaxial and uniaxial loading shows $K_{IC(med)}^{\beta=1} \big/ K_{IC(med)}^{\beta=0} \equiv K_{IC(med)}^{1:1} \big/ K_{IC(med)}^{0:1} = 128.7/140.0 \cong 0.92$. Such result is in very good agreement with the dependence: $K_{JC}^{\beta\neq 0} \big/ K_{JC}^{\beta=0} = 1 - 0.1 \cdot \beta$. This dependence was obtained on the basis of the treatment of the results calculated by using the local cleavage fracture criterion [48, 49].

5.2 Embedded Flaw Beam (Uniaxial Bending)

5.2.1 Overview of the FE analyses performed

For the post-test analyses attention was focussed largely on tests 4.1.2 (unclad) and 4.2.1 (clad) to allow assessment of the effect of the clad layer.

a) Det Norsk Veritas AB (DNV)

DNV [32] performed 2-D FE analysis of tests 4.1.2 (unclad) and 4.2.1 (clad) using ABAQUS. As for the biaxial tests, a feature of the analysis was the computation of the Q constraint parameter at the crack tip. The values obtained were compared with those calculated for both deep and shallow crack SEB specimens. The results were analysed in terms of the Master Curve and also using the R6 FAD method with constraint correction. These findings are discussed below in the relevant sections.

b) European Commission Directorate General - Joint Research Centre (JRC)

A 2-D finite element model was used to simulate the behaviour of the test pieces and to study the variation in crack tip constraint at both the near surface and deep crack tips with increasing load [50]. The beam was simulated with the commercial FE-code ABAQUS using a 2-D plane strain finite element model with eight-node bi-quadratic plane strain elements with reduced integration and hybrid formulation (CPE8RH). The moment load was simulated by a linear stress distribution over the beam thickness. A focused mesh was used at the crack tips with smallest elements of size 10^{-3} mm. Specially developed programs that allow automatic meshing for different notch geometries with the same crack tip mesh refinement were used to generate a series of meshes with a progressively increasing flaw height and reduced ligament These allowed the effect of by pseudo-crack propagation in the ligament on the crack driving force and constraint level to be studied. A Ramberg-Osgood-type deformation plasticity relation was used to model the constitutive behavior of clad, HAZ and base material: For the fracture mechanics analysis, J-integrals were computed using the domain integral method and were then transformed to elastic-plastic stress intensity factor values, K_J. Since both the shallow and deep tips are highly loaded, the location of fracture initiation is sensitive to the local constraint conditions. This effect has been examined by calculating the Q parameter. The results indicated that substantial constraint loss ($Q \sim -1$ at the beam limit load) takes places at the shallow (near-surface) tip. The deep tip is also subject to constraint loss, but to a much lesser degree. The predicted crack driving force values are slightly higher and the constraint loss slightly lower for the clad beam configuration compared to the unclad beam due to the high yield strength of the heat affected zone material. The FE results also show that, if initiation occurs at the shallow tip, crack growth through the ligament will be unstable despite considerable yielding of the clad. The application of Wallin's two-parameter model [46] was investigated and the results are considered further in the constraint section below.

c) Nuclear Research Institute Rez (NRI)

FE analysis [51, 52] was performed using SYSTUS code. The number of elements was 2832 (3D quadratic elements), with 13000 nodes. The mesh size near the crack front was 0.2 mm. A simplified approach of solving the problem was selected. Only mechanical load was applied and the thermal mismatch residual stress due to cooling from 400º to –95ºC was modelled by imposing estimated strains An acceptable accordance between experimental and calculated load vs. CMOD curves was reached. Modelling residual stresses improves the accordance between experimental and calculated

Moment vs. CMOD curves. The effect in terms of K_J is nearly 4%. Fracture toughness values for upper and lower crack fronts were calculated: J_c = 123.7 kJm^{-2} (K_{Jc} =170 MPa√m) for upper crack front, and J_c = 69.9 kJm^{-2} (K_{Jc} = 127.8 MPa√m) for lower crack front, and failure probabilities according to Master Curve concept were determined.

The Q-stress parameter for both upper and lower crack tips were calculated, although it is noted that FE mesh was relatively coarse (element size 200 μm) for such an analysis. Significant loss of constraint due to shallow crack effect was found for the upper crack tip, and some loss of constraint was found also for the lower crack tip. Practically no dependence of the Q-stress distribution with loading was found. In this connection, an interesting phenomenon was observed: The opening stress fields "scale well" i.e as the load increase so does estimated the loss of constraint) within an $r^*\sigma_0/J$ interval of 4 to 8, but not in the vicinity of 2. This is a reason why not to determine Q-stress parameter at higher $r^*\sigma_0/J$ values than 2 as it is usually recommended. At fracture, for the upper crack front: Q = -1. 04 and for the lower crack front Q = -0.45.

The effect of modelling the Lüders deformation i.e. higher material properties in the region of yield point, on the shape of calculated load vs. CMOD curve was numerically examined. The effect is to increase the calculated CMOD by up to 15% as the beam starts to plastically deform. As the bending moment is further increased, the two predictions converge together, as would be expected.

d) Oak Ridge National Laboratory (ORNL)

The ORNL analysis of the embedded flaw beams [33] used an analytical approach for cleavage fracture assessment based on a Weibull stress statistical fracture model as described in the preceding section for the cruciform beam tests under biaxial loading. The parameters for the model are estimated using the G-R-D calibration scheme, using the results of the SEB tests on deep and shallow notch specimens. The calculation of the Weibull stress used the hydrostatic stress as the effective stress.

Beam finite-element models with an embedded-flaw under uniaxial bending were constructed with the commercial code ABAQUS/CAE. The sharp-tip model had a small root radius of 0.001 mm, and contains 35,303 nodes and 7,580 elements. It was used to precisely calculate the through-thickness (average) fracture toughness $J_{applied}$ for both the top and bottom crack tips. The blunt-tip model (with a finite root radius of 0.0254 mm) was built with 39,353 nodes and 8,440 elements. This blunt-tip model was used to calculate the stress and displacement fields for the Weibull stress calculation with a modified WSTRESS code. Very detailed finite element analyses were conducted on the embedded-flaw beam models with material properties based on a temperature of –100 °C (close to the bending test temperatures). The results are considered in the Weibull model section below.

e) British Energy Generation Ltd (BE)

BE [53] used the R6 procedure [27] to make post-test best-estimate assessments of the embedded flaw tests, using the methods in Section III.7, “allowance for constraint effects”. The necessary data on constraint levels in the beams and on the effect of constraint on fracture toughness were derived from testing and analyses performed by other NESC partners. It proved necessary to use the Master Curve approach to derive appropriate fracture toughness data for the test temperatures and crack front length from the available test data. The methodology proved to be very successful in predicting qualitatively the outcome of the tests. The results are discussed in more detail in the FAD section below.

f) Serco Assurance (Serco)

In the Serco report [54] use was made of the constraint-based procedure of R6 Section III.7 together with a Beremin-type cleavage fracture model [47] to account for loss of constraint in the specimens. The analysis shows that the effect of constraint at the near surface was significant in each specimen test:

- The effect of loss of constraint at the near surface-crack tip was significant for specimens 4.1.2, 4.2.1 and 4.2.2 where failure occurred at $L_r \approx 1$. Constraint effects at the deepest crack tip were much smaller.
- Specimen 4.1.1 failed at a value $L_r = 0.44$ within the elastic regime where there was only a modest effect of loss of constraint at the near-surface crack tip. The driving force at the near-surface crack tip was higher than that at the deepest crack tip, indicating that this specimen is most likely to have failed due to cleavage fracture initiating at the near-surface crack tip.
- For specimens 4.1.2, 4.2.1 and 4.2.2, failure occurred after significant plasticity had developed, for which constraint loss is more important. Here, the loss of constraint at the near-surface crack tip was so severe that the increased fracture toughness makes it more likely that these specimens failed due to cleavage fracture initiating at the deepest crack tip.

The results are also discussed in the FAD section below.

g) Fraunhofer Institut für Werkstoffmechanik (IWM)

Detailed FE analysis was performed [39] to model the behaviour of the embedded flaw beams, considering in particular the T-stress constraint parameter. The main results include:

- The tests performed at temperatures between -90°C and -77°C failed at about the limit load for the beam. The calculated K_{Jc} values for both the near surface and lower tips fall above the standard Master Curve. This is consistent with the constraint parameter analyses which predict a large effect of constraint loss at the upper (near-to-surface) crack tip and a smaller effect at the lower crack tip.
- The upper crack tip experiences a higher stress intensity factor but also a higher loss of constraint. Hence, fracture probability at both crack tips is very similar but can not be quantified due to the small number of tests.
- The T-stress based approach using the Wallin model to adjust the reference temperature T_o provides a consistent explanation of the behaviour of the embedded flaw beams under uniaxial loading.

h) Framatome ANP GmbH

The Framatome analysis [55] considered both the unclad and clad beam designs. By means of the finite element method, local approach method and Weibull calibration models the two specimens were analysed at a test temperature of -90°C and the probability of failure calculated, taking into account constraint effects. It turned out that the failure moment of the unclad beam is 5% lower than that of the clad beam. Both crack fronts are supposed to fail at the same applied moment. The results of this particular analysis showed that the upper crack front nearer to the surface fails prior to the lower crack front, which is located deeper in the specimen (the failure moment is 5% lower). The numerical results agree well with the experiments. The experimental failure moments were accurately predicted and the failure scenario (which crack front fails first) could be determined. A theoretical shift in the transition temperature T_o due to constraint effects could be defined for both crack fronts.

5.2.2 Comparison of Crack Tip Driving force Estimates

As an initial check on the performance of the FE models, the predicted applied moment vs. CMOD were compared with the data from the uniaxial beam tests, as shown for example in Fig. 5.20. In general all the models provided accurate representations of the physical behaviour of the test pieces.

Concerning the crack tip behaviour, the focus in the first instance is on the stress intensity factor K (calculated from the FE-computed J value using the standard plain strain conversion formula). The majority of the FE analyses considered only the clad and un-clad specimens tested at approximately –90°C (4.1.2 and 4.2.1). Table 5.4 gives the values reported by the different analyses at the fracture bending moment for both the near surface (shallow) and deep tips.[7] These are also compared graphically in Fig. 5.21. The variation between the analyses is modest, with a standard deviation of 20 MPa.√m.

Concerning the influence of the clad properties on the crack driving force values, Fig. 5.22 compares the K_J vs. M at the shallow and deep crack tips for the clad and un-clad beams. Including the clad layer leads to a small increase in the Kj value for a given level of bending moment.

The 3-D analyses performed as part of the Weibull stress analyses also provided information on the predicted variation of J-Integral over the crack front. Fig. 5.23 shows the predicted J values for the deep and shallow tips for an applied moment of 106.4 KN.m. The values are constant along the crack front up (as assumed) with a fall-off occurred only in the immediate vicinity (approximately 5 mm) of the free surfaces.

Table 5.4 Comparison of the K_J values calculated for the embedded flaw beams tested in the range –90° to -95°C.

Test	T °C	DNV	JRC	NRI	IWM	ORNL	FANP	mean	st. dev
Unclad 4-1-2	-95.4								
Shallow tip		225	219	-	240	281	239	243	23
Deep tip		175	164	-	173	213	175	178	21
Clad 4-2-1	-93.2								
Shallow tip		186	147	170	195	195	178	181	14
Deep tip		133	108	128	133	128	123	127	7

5.2.3 RT_{NDT} and RT_{To} Assessment

Fig. 5.24 compares the average K_J values at fracture for the embedded flaw tests with the reference temperature transition curves based on the RT_{NDT} and RT_{To} parameters determined for the plate material (-30° and -75.5°C respectively, as discussed in section 3 above). All the test values fall above the reference curves, confirming their conservatism.

---

[7] In general the FE models considered the shallow and deep tips as sharp cracks, whereas on the test beams the only the upper tip was fatigue pre-cracked and the lower tip had a radius of approximately 0.25 mm.

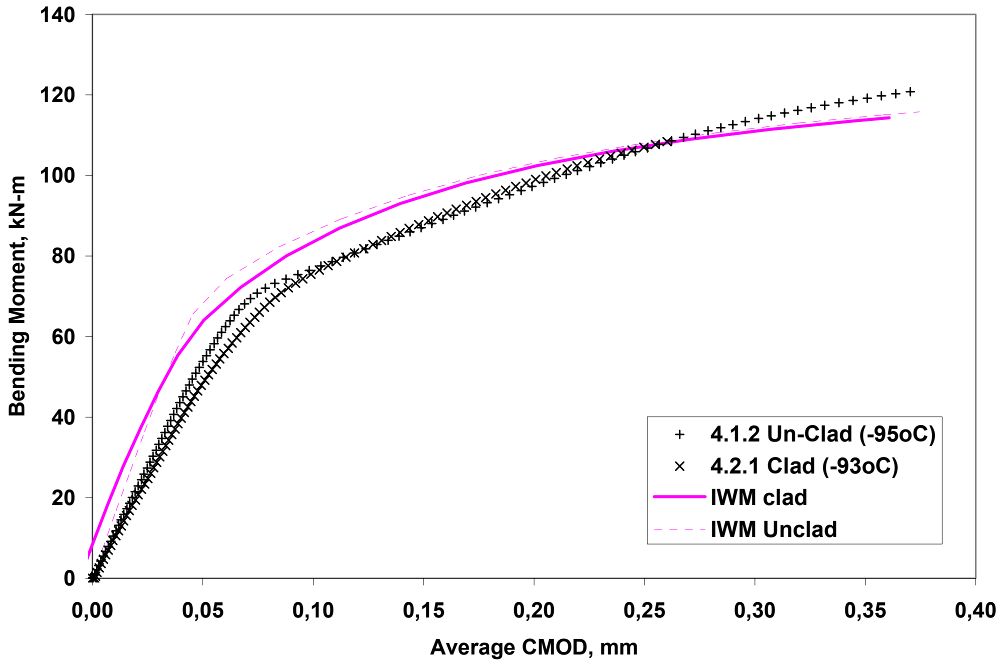

Fig. 5.20 Comparison of the experimental CMOD vs bend moment curves with the typical predictions from FE analyses [39].

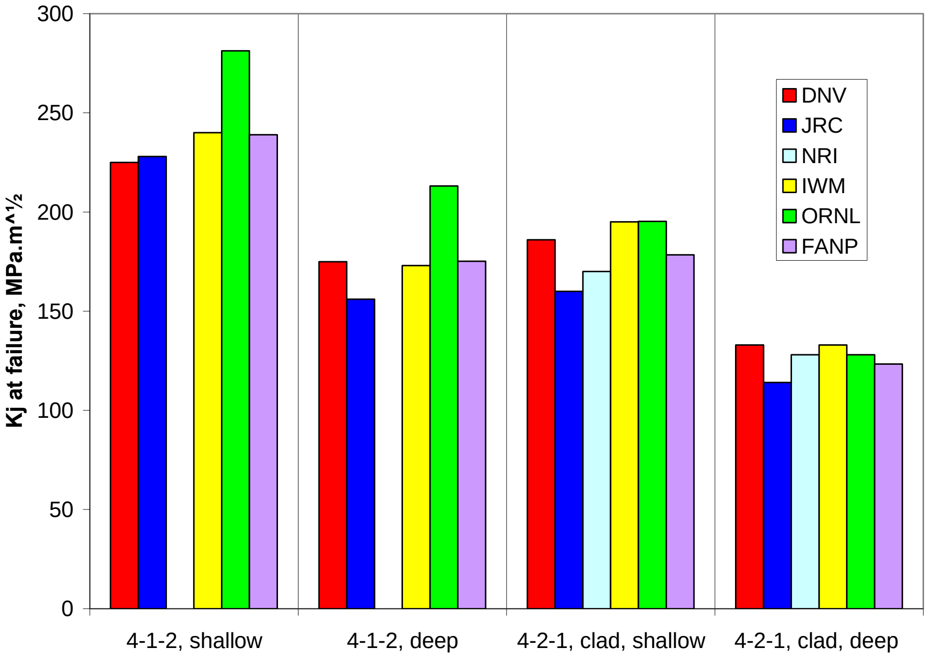

Fig. 5.21 Comparison of the K values calculated for the embedded flaw beam test pieces tested at approximately -90°C under uniaxial loading.

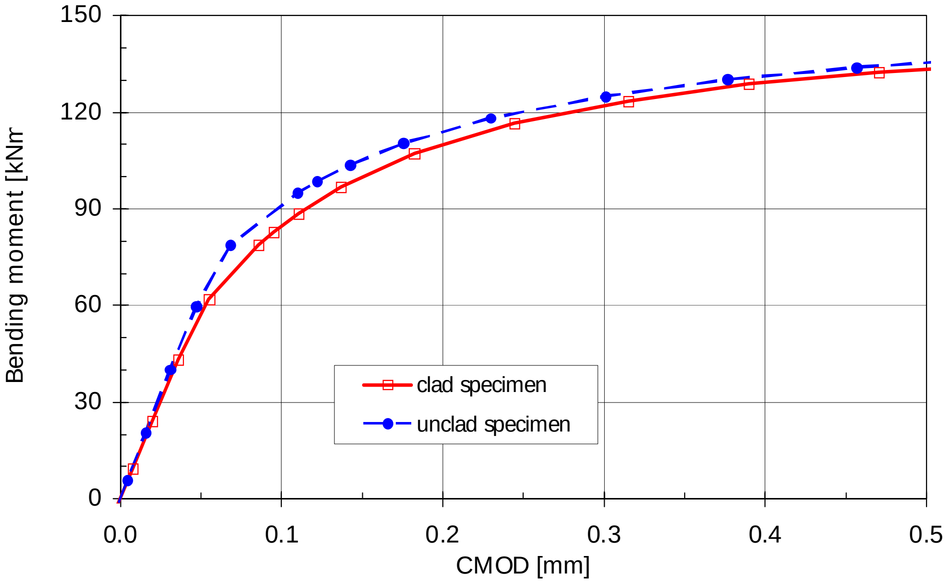

Fig. 5.22 Computed moment vs. CMOD for the clad and un-clad beam models [39].

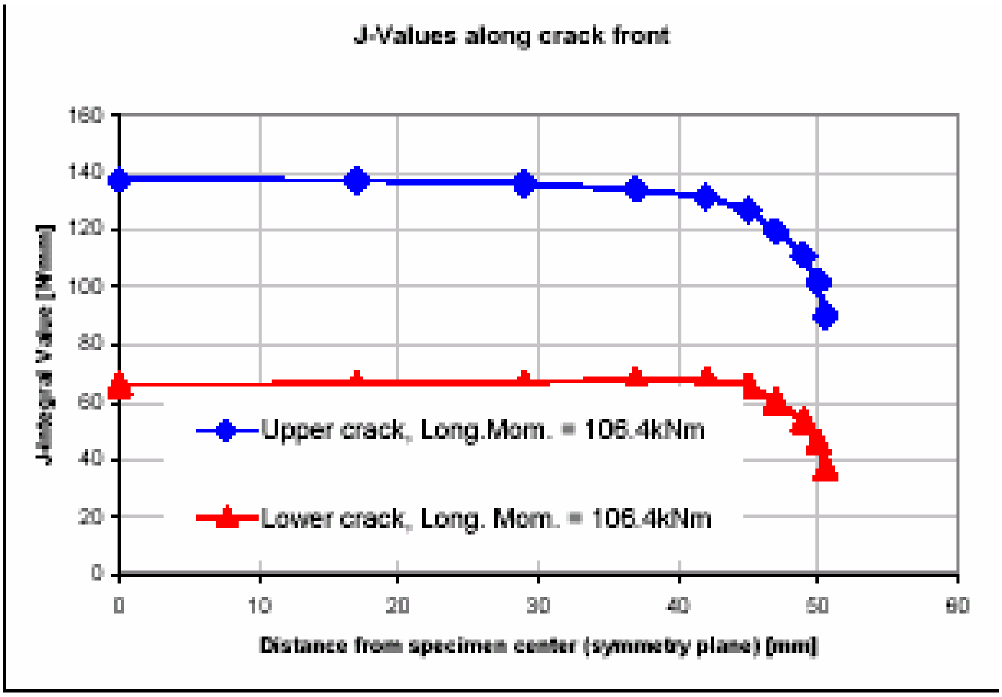

Fig. 5.23 J-values along both crack fronts at failure moment. CMOD-shape at the same loading state in the centre and at the surface (Framatome [55])

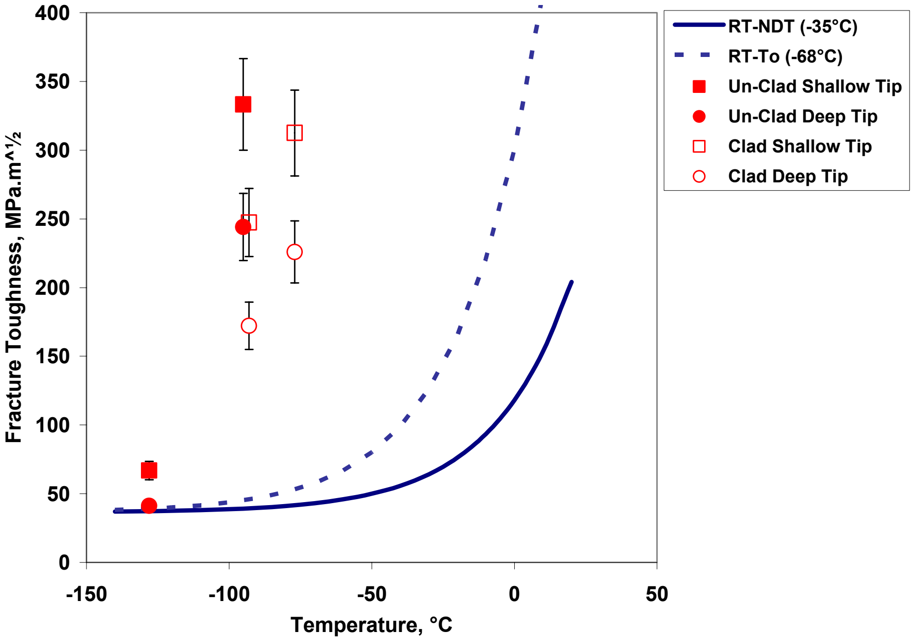

Fig. 5.24 Results of the embedded flaw tests compared with the RT_{NDT} and RT_{To} transition curves

5.2.4 Master Curve Assessment

This section examines the application of standard Master Curve methodology, following the general approach for flaws in components as described by Wallin [46]. The issue of constraint is covered in a separate section below. The assessment is based on the estimates of K_{Jc} at the fracture load for the deep and shallow tips. Since the distribution of K_J over the crack front is rather uniform, the standard size correction relation has been applied to reference the values to a 25 mm crack front:

$$K_{Jc} = 20 + \left(K_{Jc(\exp)} - 20\right)\left[\frac{B_{\exp}}{25}\right]^{1/4} \tag{5.8}$$

Concerning the Master Curve itself, the T_o parameter was determined from the various test series on the PVRUF plate materials (see Chapter 3, Table 3.7 above).

Fig. 5.25 compares the predicted K_I values at fracture for both the deep and shallow crack tips with the 5, 50 and 95% cleavage probability Master Curves, based on the standard high constraint T_o estimate of -88°C. With the exception of the test performed at –128°C (almost in the lower shelf), the data lie well above even the P_f(95%) Master Curve, indicated that substantial constraint loss occurs at both crack tips.

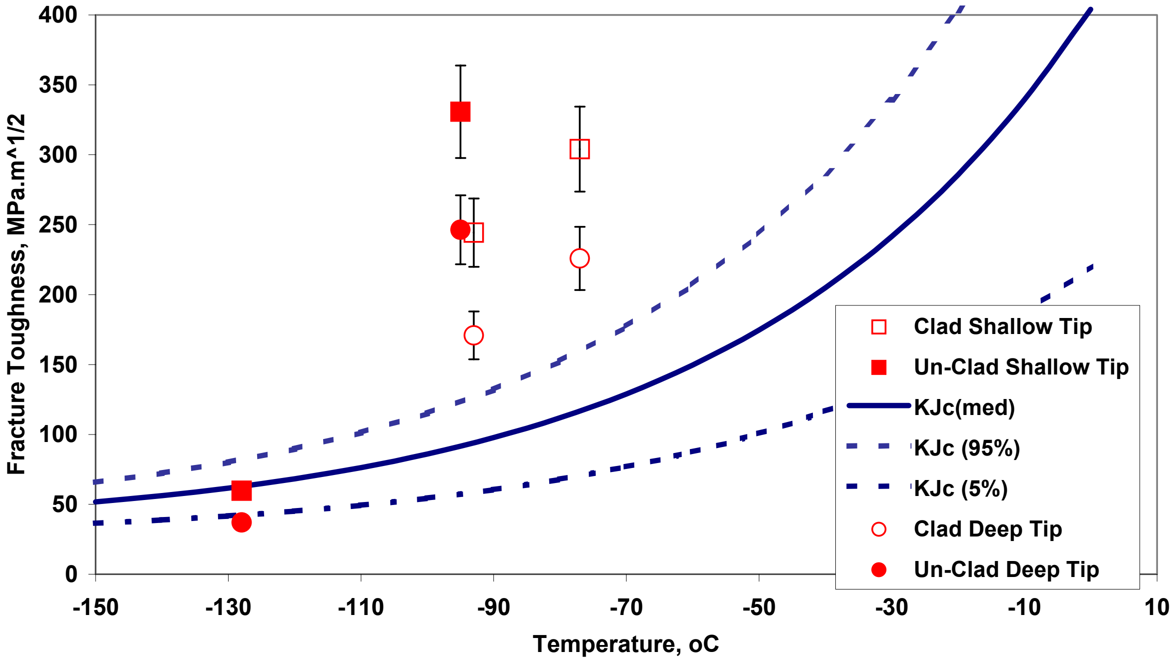

Fig. 5.25 Average values of K at fracture (size corrected to B = 25 mm) compared with the Master Curve (5%, 50% and 95%).

5.2.5 Constraint Estimation Parameters

Several investigations examined the role of constraint, principally via the T-stress and Q parameters. The following summarizes the findings.

a) T-stress parameter
IWM were the only organization to evaluate the elastic T-stress parameter from their FE models. Fig. 5.26 shows the calculated trend for both the shallow and deep tips with increasing load. Constraint loss (negative T-stress values) is predicted for the both tip, although the effect is most pronounced for the shallow tip.

a) Q Parameter
The Q parameter is expected to provide a more accurate estimate of constraint level than the T-stress at loads for which elastic-plastic conditions prevail. DNV, NRI and JRC studied the variation of the Q parameter for both the upper and lower tips for a nominal test temperature of -90^{o}C. In all three cases the formulation of Q used was based on the crack opening stress, σ_1, as defined in eqn.5.4 above. Fig. 5.27 show the JRC's predictions for the relation between Q and the crack tip driving force K_J at both crack tips and for the cald and unclad beam geometries. NRI's analysis of the variation of Q ahead of the crack tip is shown in Fig. 5.28. The DNV values for Q at K_J = 100 MPa.√m are summarized in Table 5.5. All these results are in good agreement with each other and indicate that constraint loss occurs at both tips, with the effect being particularly pronounced for the shallow tip. Fig. 5.29 compares the relation of Q and normalized T-stress with applied bending moment. As expected, at low loads both predictions are in close agreement.

Table 5.5: *Q*-values evaluated at *r/(J/σ_Y)* =2 for different crack configurations in the PVRUF plate material at K = 100 MPa.√m (DNV)

Case	Q
SE(B), a/W= 0.50	+ 0.05
SE(B), a/W= 0.20	- 0.34
SE(B), a/W= 0.10	- 0.68
Embedded flaw, deep tip	- 0.35
Embedded flaw, shallow tip	- 1.05

5.2.6 Wallin T-stress Constraint Loss Model

The JRC study [50] adopted Wallin's simplified two-parameter approach [46] to estimate the shift in the Master Curve T_0 parameter due to the local constraint loss. This has advantages in that a) its simplicity makes it well-adapted for sensitivity analysis and b) the "shifted" Master Curve expression can be inverted to obtain a fracture probability value, so allowing different crack tip scenarios to be compared. The constraint-corrected T_0 parameter is given by:

$$T_o^{Tstress<0} = T_o^{Tstress=0} + \frac{T_{stress}}{10\ MPa\ {}^oC^{-1}} \tag{5.9}$$

where the $T_0^{Tstress=0}$ value is taken as that for small scale yielding (high constraint) conditions when the T_{stress} is nominally zero. As shown in Fig. 5.29, eqn.(5.9) provides a reasonable approximation of the constraint loss effect found shallow flaw SE(B) specimens from Plate 100. It is also noted that the test temperatures for the low constraint specimens were generally 20 to 30°C lower than those for the high constraint specimens. Given the simple linear form of eqn.(5.9), a criticism is that it will be prone to overestimate the constraint loss effect when the T_{stress} is only slightly negative and underestimate it when the T_{stress} is strongly negative.[8] It can be shown, for instance, that the constraint loss models of Gao et al [29] and Sherry et al [28] predict a non-relationship between the shift in T_o and the T_{stress}. Both approaches require knowledge of tensile properties (E, n and σ) and the Weibull exponent, m. Calibrating m is non-trivial and studies within the NESC-IV project have produced estimates ranging form 3.4 (with the Weibull stress defined in terms of the hydrostatic stress) to 14.8 (with the Weibull stress defined in terms of the crack opening stress). Taking for example the model of Sherry et al (that of Gao and Dodds produces very similar results but is calibrated for a narrower range of m values), the constraint-modified value of K_{Jc} is given by:

$$K_{Jc}^{T-stress<0} = K_c^{T-stress=0}\left[1+\alpha\left(T/\sigma_o\right)^k\right] \tag{5.10}$$

where the parameters α and k depend on E/ σ_o, n and m, and are given by look-up tables in ref. [28]. Assuming that the shift in the T_o reference is uniform of the transition temperature range, it value can be determined from the Master Curve expression at $P_f = 0.5$ and assuming a reference value of K_c = 100 MPa for eqn.(5.9):

---

[8] The overestimation of constaint loss for T/σ just less than 1 is offset to some extent by the implicit upward shift of eqn.(10), which occurs since the T_o value at $T_{stress} = 0$ is determined from deep-notch specimen data, for which the actual T_{stress} value is typically greater +0.15 for SE(B) specimens and +0.45 for C(T) specimens.

$$\Delta T_0 = -\frac{1}{0.019}\ln\left(\frac{K_C^{T-stress<o} - 30}{70}\right) \qquad (5.11)$$

This calculation was made for sets for α and k values corresponding to a) E/ σ_o = 425, n=6 and m =5 and b) E/ σ_o = 425, n=6 and m =5, which bound the reported range of m. The resulting curves are included in Fig. 5.29. For m = 5, the prediction appears to provide a lower bound and as such strongly underestimates the constraint loss observed in the tests on a/W=0.1 specimens. This discrepancy may also reflect the fact that both the Sherry et al and Gao et al models are based on Weibull models defined in terms of the crack opening stress rather the hydrostatic stress definition, which produced the low m estimate. The curve generated with m = 15 is only slightly non-linear and agrees rather well with the simple Wallin model.

To apply eqn.(5.9) for the embedded flaw beam tests requires that the T_{stress} value is known for both crack tips as a function of bending moment. Although the JRC FE analysis did not directly calculate the T_{stress}, its value was inferred from the Q parameter results at low loads based on the equivalence: $Q \simeq T_{stress}/\sigma_0$. [56]. Further, since T_{stress} is an elastic parameter and proportional to applied load or moment, the linear trend can be extrapolated to higher bending moment values, as shown in Fig.5.30. In this way a value of T_{stress} and hence estimates of $T_0^{T_{stress}<0}$ can be obtained via eqn.(5.10) for either the shallow or the deep crack tip for any bending load value. Finally since the FE analysis provides the relation between K_J and M at each crack tip, the Master Curve equations can be inverted to give P_f as a function of applied bending moment.

Figure 5.30 presents typical P_f vs. M predictions, in this case for clad beam 4-2-1. For each crack tip two curves are shown: the first gives P_f values from the standard ($T_0^{T_{stress}=0}$) Master Curve; the second gives P_f values from the Master curve with the constraint loss correction ($T_0^{T_{stress}<0}$). The solid vertical line shows the measured fracture load; the P_f values at which this intersects the predicted curves are reported in Table 5.6. In general it is seen that for the shallow crack tip the constraint adjustment has two main consequences: a) it shifts the probability curves so that for a given moment the failure probability decreases and b) the likely point of fracture initiation (shallow or deep) tip becomes temperature dependent. Taking point b) first, without constraint adjustment fracture is predicted to always be more likely for the shallow than the deep tip. With the constraint loss model, three regimes can be identified. Well below the T_o temperature, failure is predicted at the lower tip and well above T_o, fracture is predicted at the deep tip first. In the intermediate range, the failure probability curves for the shallow and deep tips cross at a certain load level. Up to that point, fracture initiation is predicted at the shallow tip; above it, initiation is more likely at the deep tip (due to the constraint loss at the shallow tip at higher loads). The test temperature for 50% fracture probability for the shallow and deep tip is in fact relatively close to that used for tests Unclad 4.1.2 and Clad 4.2.2 i.e. in the range -90 to-95°C. This implies that a somewhat lower test temperature would be necessary to ensure fracture initiation at the upper tip.

The second aspect concerns the effect of constraint loss on the fracture load itself and hence on potential for increasing the load carrying capacity of the beams. The first test, which was performed at much lower temperature (-128 °C) than the others, is predicted to have experienced a modest loss of constraint, although the fracture probability is always higher for the shallow tip. However the P_f value of 0.77 obtained without constraint loss agrees better with the test result than that of 0.16 determined with the constraint loss correction. For the three other tests P_f is effectively 1.00 at the reported fracture loads if loss of constraint is not accounted for. When the fracture probability curves are constraint adjusted, an increase in the fracture load of over 30% is calculated at the P_f =0.5 level. In fact the P_f values at the experimentally recorded fracture loads are still very high (>0.96), and in all three cases initiation is predicted at the deep tip. The apparent overestimate of the constraint loss effect by the Wallin model for the first test at low temperature and load and its underestimate for the other three cases is not unexpected given the linear nature of eqn.(5.8). The former effect could be remedied by introducing a threshold on K_J before constraint loss effects could be applied.

Table 5.6 – JRC results from the Master Curve + T-stress constraint loss model

Test	Temp. °C	Crack Tip	K_{Jc} [1] MPa√m	T_{stress} [2] MPa	ΔT_0 [3] °C	Fracture Probability, P_f	
						No constraint correction	Wallin constraint correction
4-1-1 unclad	-128.1	Shallow	66	-283	-28	0.63	0.16
		Deep	41	-99	-10	0.04	0.02
4-1-2 unclad	-90.4	Shallow	316	-600	-60	> 0.999	0.89
		Deep	214	-209	-21	> 0.999	> 0.999
4-2-1 clad	-93.2	Shallow	219	-507	-51	> 0.999	0.68
		Deep	154	-195	-19	> 0.999	0.88
4-2-2 clad	-77.2	Shallow	312	-574	-57	> 0.999	0.62
		Deep	225	-222	-22	> 0.999	0.94

Notes

1) K_{Jc} values as calculated via FE analysis and size-corrected to 25 mm thickness using eqn.(5.8)

2) From the projected T-stress vs. bending moment trend line, as in Fig. 5.28

3) Calculated with respect to T_0 = -88°C from eqn.(5.9)

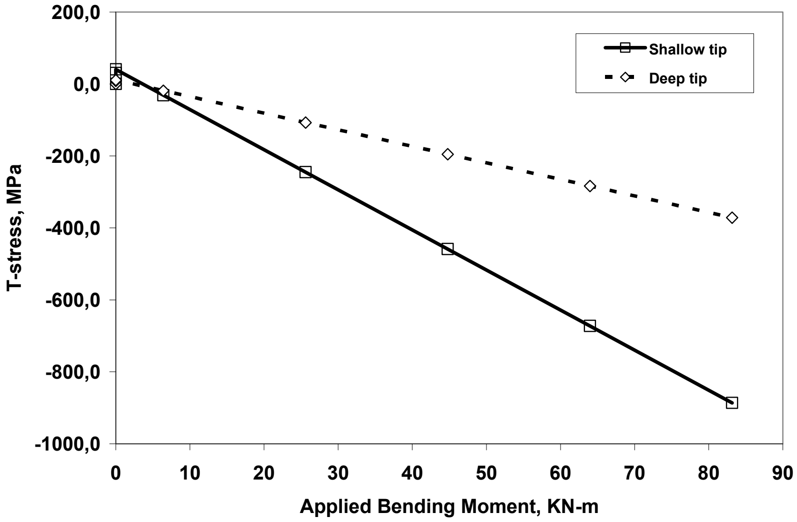

Fig. 5.26 IWM predictions for the change in T-stress with applied load (clad beam, -93°C)

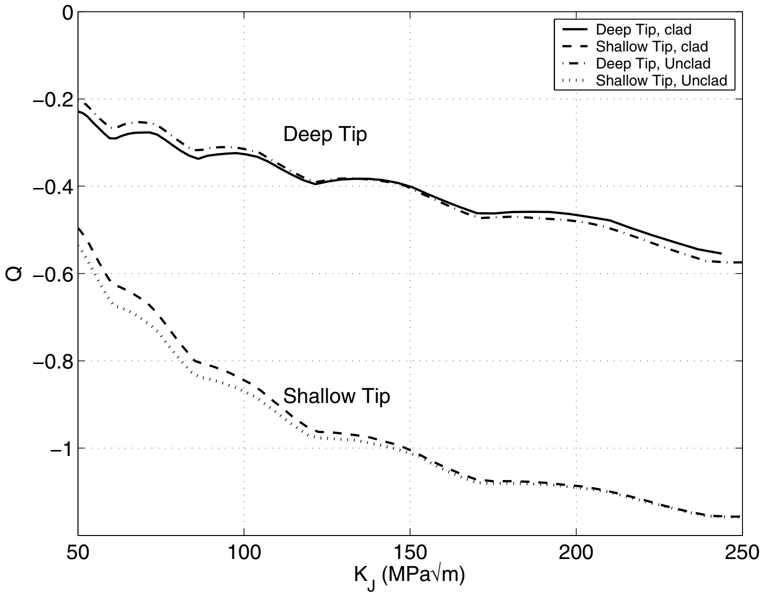

Fig. 5.27 Dependence of Q on load for the upper and lower crack tips in the clad and un-clad geometries (JRC).

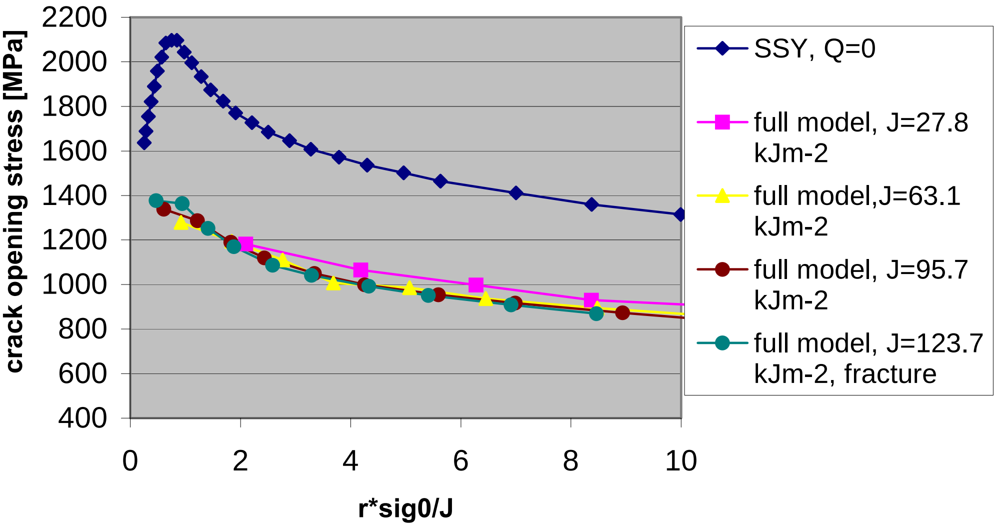

Fig. 5.28 Dependence of the crack opening stress on the distance from the crack tip (NRI).

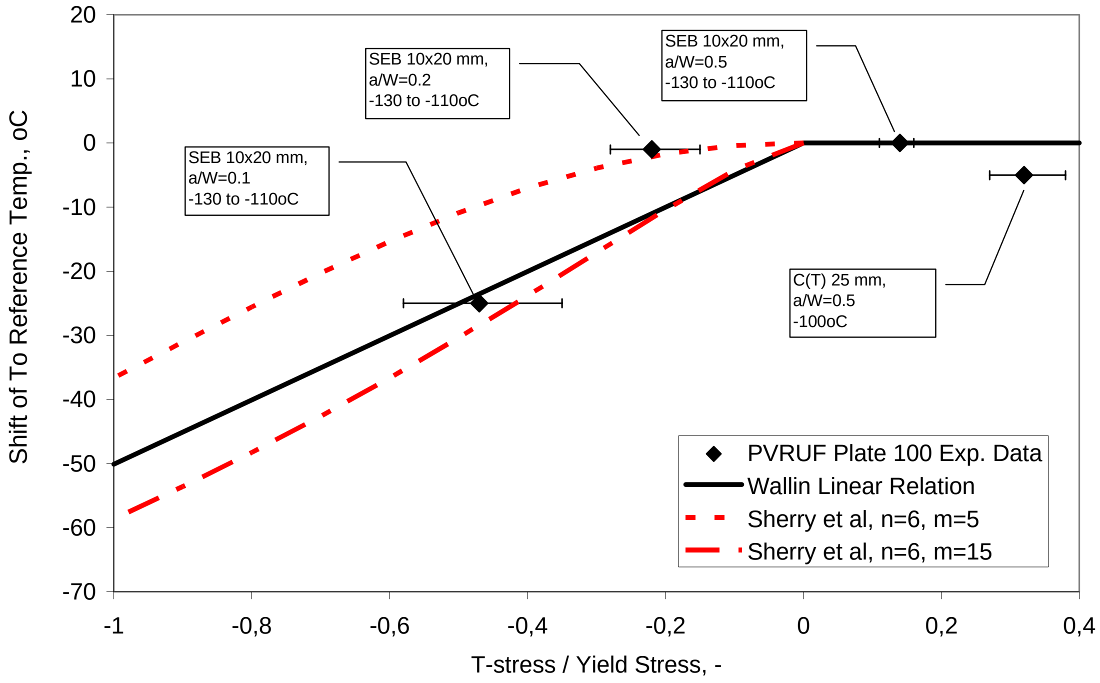

Fig. 5.30 PVRUF Plate 100: dependence of the T_o parameter on normalised T-stress - comparison of experimental data and predictions

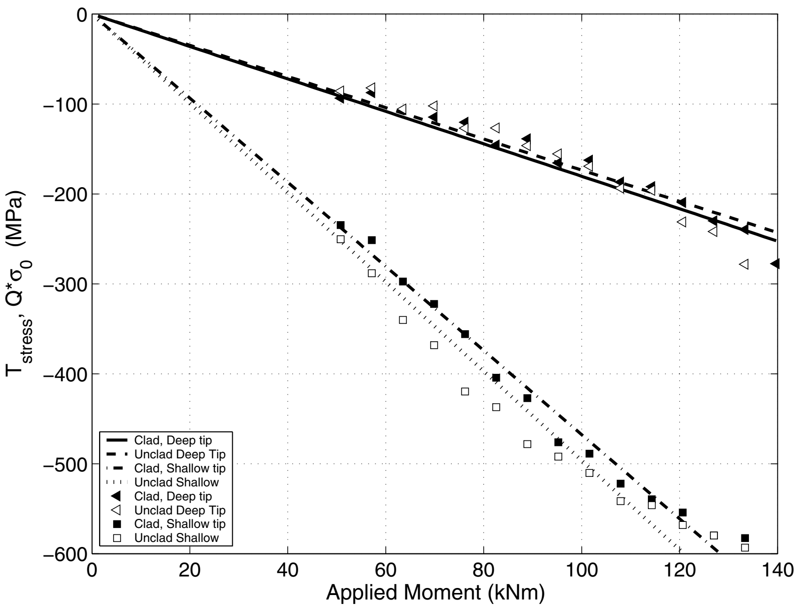

Fig. 5.30 JRC predictions for the change in T-stress with applied load (clad beam, -93oC), as derived from the Q parameter analysis

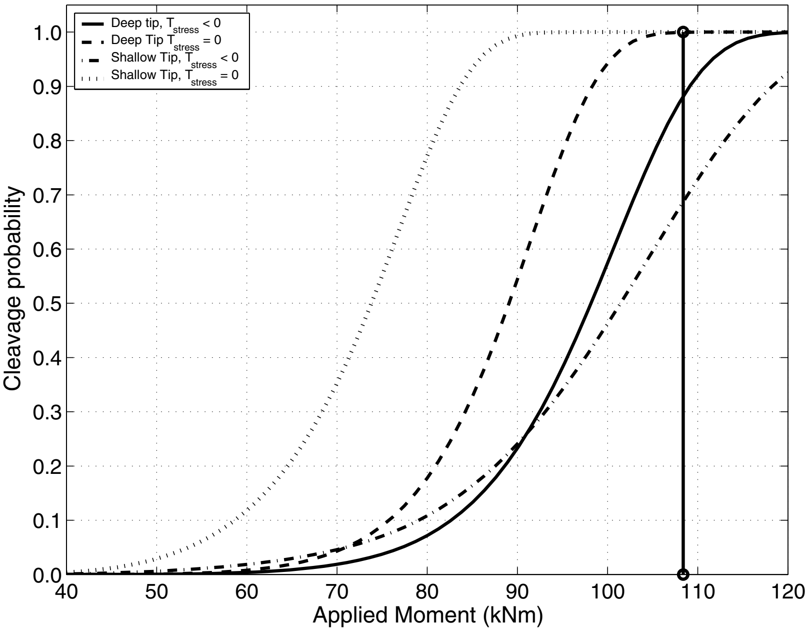

Fig. 5.31 Fracture probability as a function of bending moment for the shallow and deep tip, with (T_{stress} < 0) and without (T_{stress} = 0) constraint loss for Clad beam (4-2-1) at –93 °C.

5.2.7 Failure Assessment Diagram (FAD)

Three organisations (BE, Serco and DNV) investigated the application of the R6 FAD methodology [27] to the embedded flaw beam tests, considering in particular the procedure in R6 Section III.7 to reduce potential over-conservatism by taking into account of constraint loss effects. Two approaches are foreseen. In the first the FAD curve is modified via the relation:

$$K_r = f(L_r)\left[1+\alpha\left(-\beta L_r\right)^m\right] \tag{5.12}$$

Here the parameter β is defined either in terms of the T-stress or Q, while α and m[9] are derived from fracture toughness test data at different constraint levels using the relationship:

$$K_{mat}^{c} = K_{mat}\left[1+\alpha\left(-\beta L_r\right)^m\right] \tag{5.13}$$

where K_{mat} is the fracture toughness of a high constraint specimen and K^c_{mat} is the fracture toughness at a reduced constraint level. BE and DNV adopted this approach. The alternative route, studied by Serco, is to apply the constraint loss modification to K_r directly, so $K_r = K_I/K^c_{mat}$. Both approaches should give equivalent results.

---

[9] The exponent "m" in equations 5.11 and 5.12 should not be confused with the Weibull shape parameter, also denoted as m.

R6 does prescribe a fracture toughness transition curve as such, however methods such as the Master Curve are typically used to provide estimates of K_{mat} if appropriate experimental data is not available for the relevant temperature range and material condition. In the case of the Plate 200 material used for the embedded flaw tests, despite a database of some 70 fracture toughness tests, insufficient data were available for the feature test temperature to directly derive the R6 constraint-modified toughness parameters. This was because the majority of the tests were performed on material extracted from a different A533B plate (Plate 100) to that used in the large-scale tests, in a temperature range that did not cover the actual test temperature. As a result the Master Curve methodology was used to transfer fracture toughness data obtained at different temperatures and crack front lengths to the temperatures and crack front length of the embedded flaw tests.

The Master Curve also allowed the effect of constraint loss on the Plate 200 material used for the embedded flaw beams to be to be inferred from the Plate 100 response. In the case of the BE and DNV analyses, the fracture toughness data so inferred were used to derive R6 constraint-modified toughness parameters ($\alpha = 1.1$ and $k = 2.7$). Serco adopted a different approach, using recent work by Sherry et al [28] to estimate the α and m values from a knowledge of the flow properties and the shape parameter m of the Beremin cleavage fracture model [47]. In fact a range of m values (5, 7.5 and 10) were considered, corresponding to that typical for ferritic materials using best practice calibration methods [35]. Fig. 5.32 compares the predicted increase in toughness from the various functions at the -90^{o}C test temperature. The Sherry et al curve with m = 5 agrees best with the Master Curve extrapolated experimental data. Higher values of m produce an over-prediction of the potential toughness increase due to constraint loss.

Fig. 5.33 illustrates the results obtained by BE using the R6 Option 1 with the constraint loss modification to the FAD method and with K_{mat} size corrected to a crack front length of 100 mm. This proved to be very successful in predicting qualitatively the outcome of the tests. It showed that the first test, at -128°C, failed at about $L_r = 0.4$ under small-scale yielding conditions where constraint effects were neither expected nor observed. The subsequent tests, at temperatures between -90°C and -77°C, failed close to L_r=1. Constraint loss at the near surface crack tip raises the effective toughness to such an extent that fracture probably initiates at the deeper tip, which has a lower crack driving force but higher constraint. The DNV analysis produced comparable conclusions to those of BE.

Concerning the effect of crack front size correction, R6 best-estimate assessments were also performed without any size front correction. The predictions are compared with the test results in Fig. 5.34. Two points arise from comparison with the 100mm crack front length assessments in Fig. 5.32:

- The level of non-conservatism in the prediction of the first test is larger than for a crack front length of 100mm.
- The remaining three tests are still predicted to fail at the lower crack tip, although there is now no margin left in the assessments.

Thus omitting the 100mm size correction makes no qualitative change to the assessments, but does change the remaining margins, or lack thereof. The B=100mm assessments do however appear to fit the tests slightly better. No significant constraint effect is predicted for either the first test or the lower crack tips of the remaining tests, so the use or omission of a size correction is the only significant assumption being tested at these points.

Serco also applied the R6 methodology, using both Options 1 (no work hardening) and 2 (with work hardening), as well as making use of a constraint modified K_{mat} value[10]. Two types of assessment were carried out:

- Predictions of expected behaviour – using a median or 50% value of the fracture toughness to calculate K_r. For this analysis, the point where the load line and the failure assessment curve intersect represents the expected or "average" failure load which would result if a series of identical buried defect specimens had been tested.
- Predictions of lower bound behaviour – using a lower bound, 2%, value of fracture toughness to calculate K_r. Here, the intersection of the load line and failure assessment curves provides a lower bound, conservative value for the failure load. In a conservative, R6 safety assessment, the specimen may be "unsafe" (at risk of cleavage) at the predicted lower bound load.

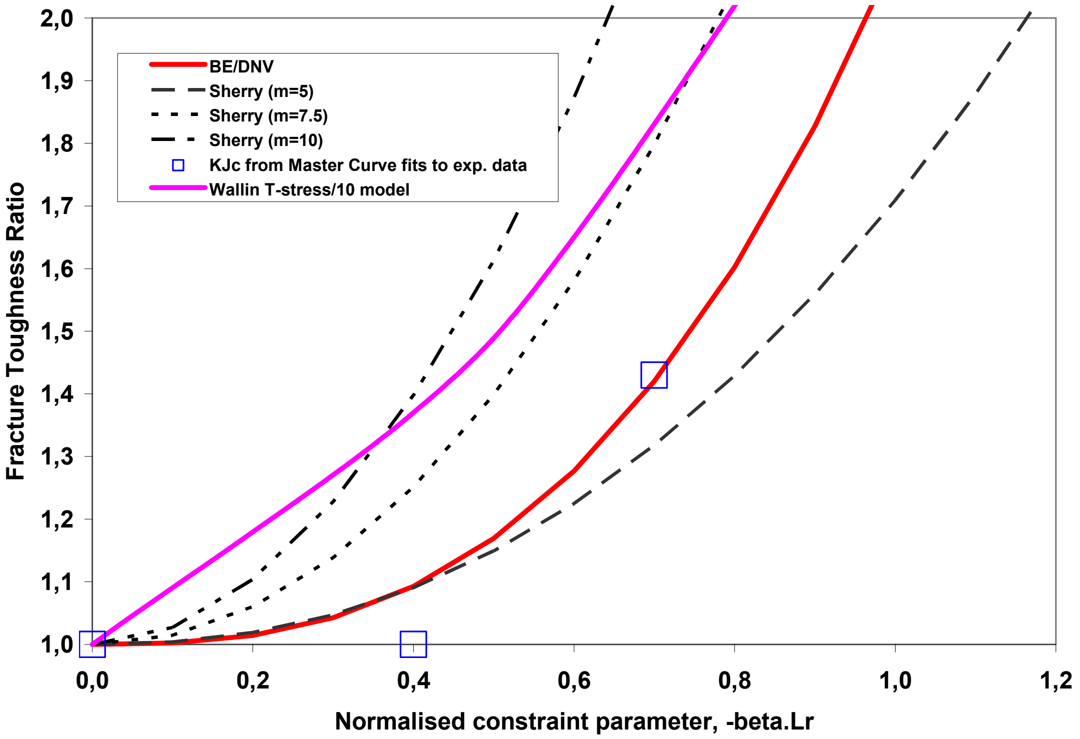

Fig. 5.32 Comparison of the constraint loss function used in the in the R6 assessments for Plate 100/200 at –90°C.

---

[10] In the R6 methodology constraint loss can modelled either via a modified FAD (as in the BE analysis) or via the K_{mat} parameter (as done here for the Serco analysis). Both routes provide equivalent results.

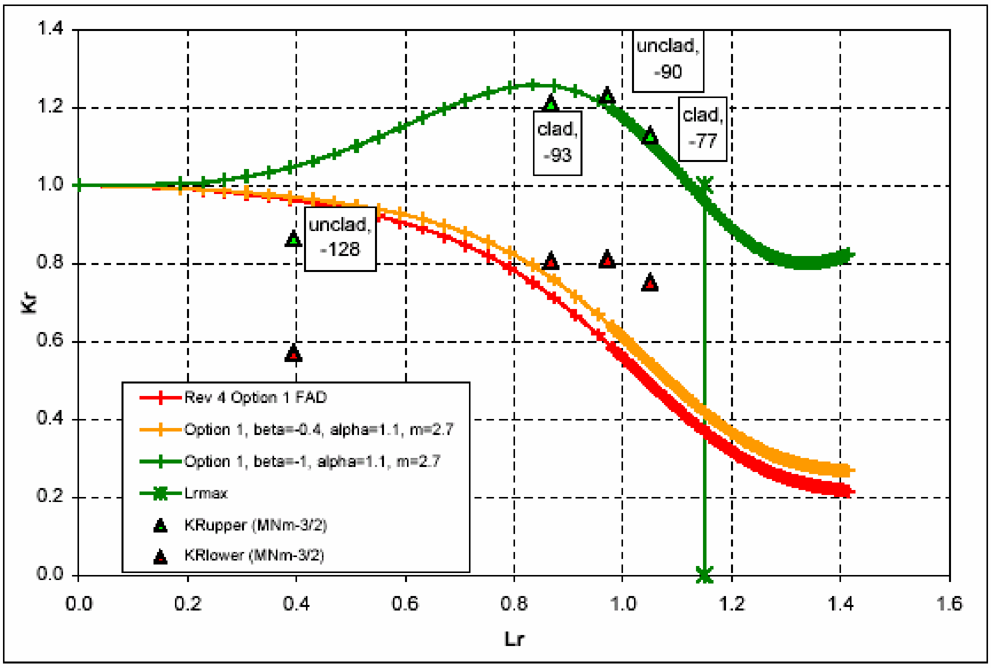

b) plane strain, K_r calculated with toughness data size-corrected to 100 mm

Fig. 5.33 BE R6 assessments of the embedded flaw test series with toughness data size corrected to 100 mm.

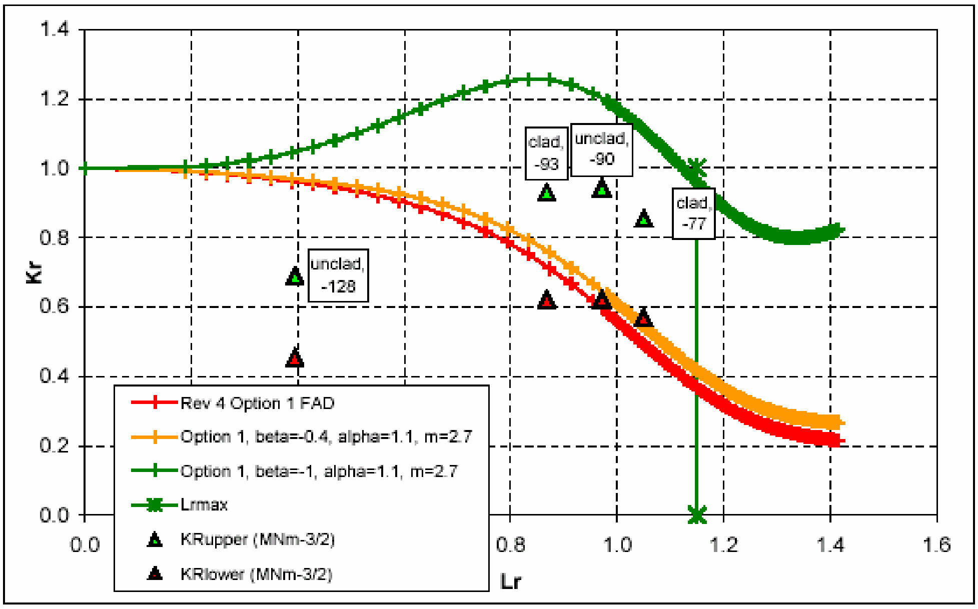

a) Plane strain, K_r calculated with toughness data size-corrected to 25 mm

Fig. 5.34 BE R6 assessments of the embedded flaw test series with toughness data size corrected to 25 mm.

Typical results for Clad 4.2.1 tested at -94°C are shown in Figs. 5.35a and 5.35b (median and P_f=2% lower bound fracture toughness values respectively). The plots show loading lines i.e. the K_r-L_r relation for a fixed flaw size as load is progressively increased, corresponding to no constraint adjustment (nca) and constraint-adjusted K_{mat} with different m values (see equation 5.12). The overall conclusions are similar to those of the BE analyses:

- The effect of loss of constraint at the near surface-crack tip was significant for specimens 4.1.2, 4.2.1 and 4.2.2 where failure occurred at $Lr \approx 1$. Constraint effects at the deepest crack tip were much smaller.
- Specimen 4.1.1 failed at a value $L_r = 0.44$ within the elastic regime where there was only a modest effect of loss of constraint at the near-surface crack tip. The driving force at the near-surface crack tip was higher than that at the deepest crack tip, indicating that this specimen is most likely to have failed due to cleavage fracture initiating at the near-surface crack tip.
- For specimens 4.1.2, 4.2.1 and 4.2.2, failure occurred after significant plasticity had developed, for which constraint loss is more important. Here, the loss of constraint at the near-surface crack tip was so severe that the increased fracture toughness makes it more likely that these specimens failed due to cleavage fracture initiating at the deepest crack tip.

Table 5.7 lists the probability that the failure occurred at each crack tip and indicates whether the R6 assessment using a 2% fracture toughness was conservative. Failure probabilities are given only for m = 7.5. The results for the crack tip deemed most likely to have failed are highlighted in bold.

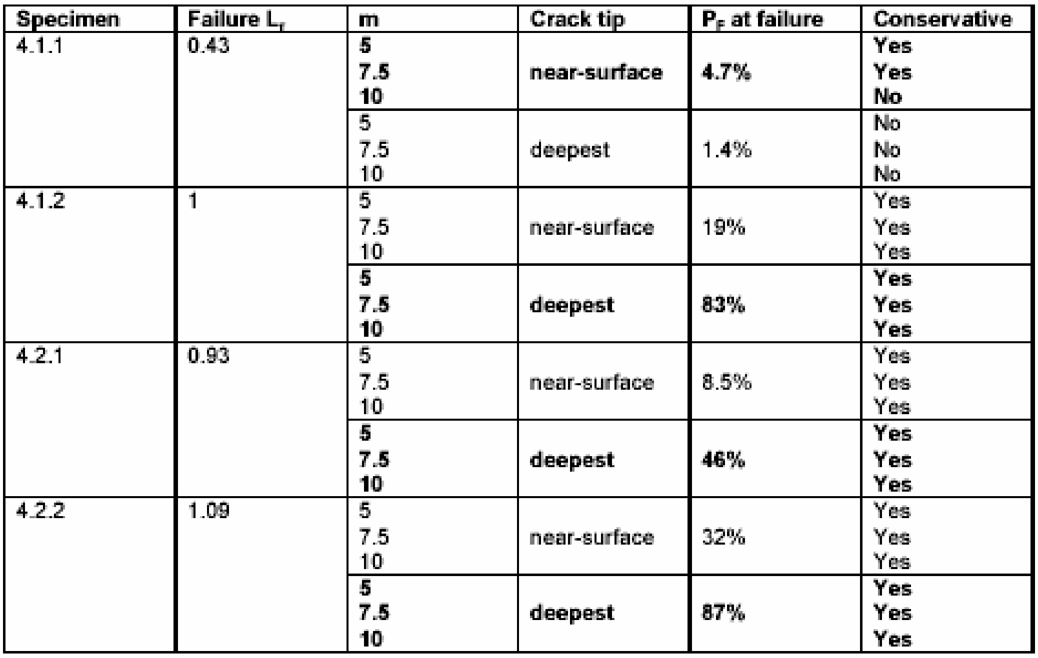

Specimen	Failure L_r	m	Crack tip	P_F at failure	Conservative
4.1.1	0.43	**5** **7.5** **10**	**near-surface**	**4.7%**	**Yes** **Yes** **No**
		5 7.5 10	deepest	1.4%	No No No
4.1.2	1	5 7.5 10	near-surface	19%	Yes Yes Yes
		5 **7.5** **10**	**deepest**	**83%**	**Yes** **Yes** **Yes**
4.2.1	0.93	5 7.5 10	near-surface	8.5%	Yes Yes Yes
		5 **7.5** **10**	**deepest**	**46%**	**Yes** **Yes** **Yes**
4.2.2	1.09	5 7.5 10	near-surface	32%	Yes Yes Yes
		5 **7.5** **10**	**deepest**	**87%**	**Yes** **Yes** **Yes**

Table 5.7 Probability of failure at each crack tip as a function of m, using a 2% failure probability fracture toughness value (Serco, [54]).

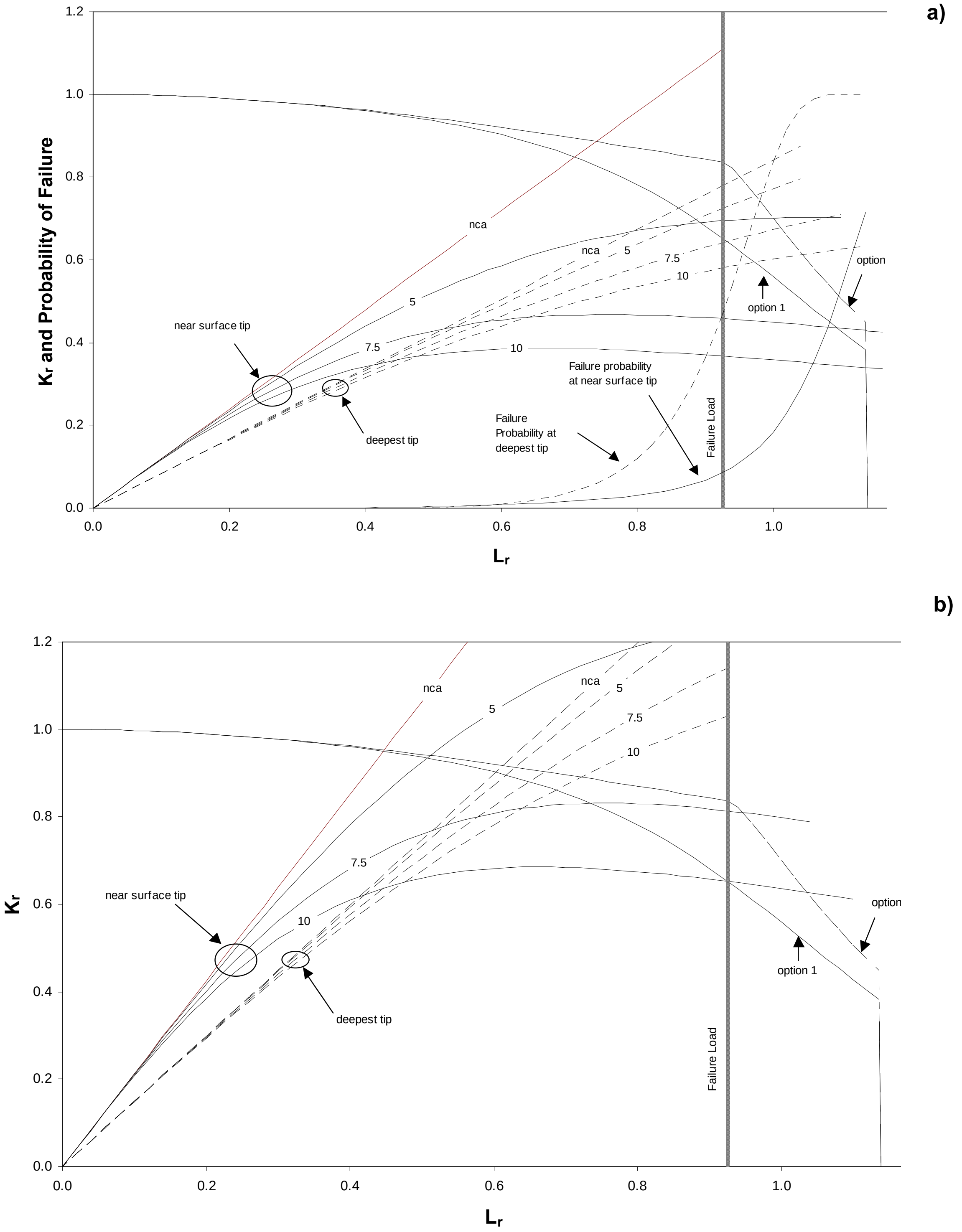

Fig. 5.35 FAD diagrams from the Serco R6 analysis of Clad 4.2.1 for a) a median 50% value of fracture toughness and b) a lower bound 2% value of fracture toughness

5.2.8 Weibull Models of Cleavage Fracture Toughness

The analytical approach for cleavage fracture assessment applied by ORNL and Framatome was based on a Weibull stress statistical fracture model as described in section 5.1.7. The parameters for the model were estimated for the PVRUF plate material using the G-R-D calibration scheme [35]. The ORNL calculation used the hydrostatic stress (σ_H as the effective stress (σ_q in equation 5.5) for the calculation of the Weibull stress so as to capture the constraint effect due to both shallow flaw effects and biaxial loading, whereas in the Framatome model the principal stress (σ_1) was used.

Given the estimated reference temperature T_o values and high-constraint conditions with a 1T flaw length, fracture toughness K_{Jc} (or J_c) data were stochastically-simulated from the Master Curve Weibull statistical model. A sample size between 50 and 60 was chosen, since adequate convergence had been obtained for this sample size in a previous study. Using the simulated 1T J_c data set (converted from K_{Jc}), an iterative Weibull stress calibration was carried out using 1T SE(B) bend-bar finite-element models (a/W = 0.1 for low constraint and a/W = 0.5 for high constraint) at a temperature of –100 °C. The Weibull stress shape parameter (m), obtained from this calibration procedure, is assumed to be temperature invariant. A modified Weibull stress calibration approach was recently developed at ORNL and Framatome to calculate the reference temperature T_0 at different constraint levels using the following procedure:

a) With the calibrated value for m using the SE(B) finite element models, map the stochastically-generated data (both shallow-flaw and deep-flaw datasets) from the SE(B) shallow-flaw (J_{low}) and deep-flaw (J_{high}) Weibull stress σ_W vs. J_C curves back to the SSY curve (J_{ssy}). The four fracture toughness data sets (J_{low}, J_{high}, $J_{low\text{-}SSY}$ and $J_{high\text{-}SSY}$) represent three constraint levels: (1) low constraint, (2) high constraint, and (3) SSY constraint (combined $J_{low\text{-}SSY}$ and $J_{high\text{-}SSY}$).
b) Convert the mapped J_c data to K_{Jc} by the plane-strain conversion.
c) Calculate the corresponding T_0 values for each dataset based on the procedure in ASTM E-1921.

Both ORNL and Framatome used the general purpose finite element code ABAQUS for the fracture mechanics investigations. The Weibull stresses were calculated using in-house post processor codes. The outcome of the numerical analysis was compared to the experimental values. The Weibull provides probability of failure estimates which can be used to address issues such as:

- Which crack front is most likely to fail first?
- Is there a difference in the failure behaviour between the clad and un-clad specimens?
- Is there a constraint caused shift in the transition temperature T_o compared to regular fracture toughness specimens?

The results of the ORNL calibration with the hydrostatic stress as the effective stress are shown in Fig. 5.36, where the calibrated Weibull shape parameter m is 3.4. The Framatome analysis, with the σ_1 definition of the effective stress, yielded an “m” value of 14.8.

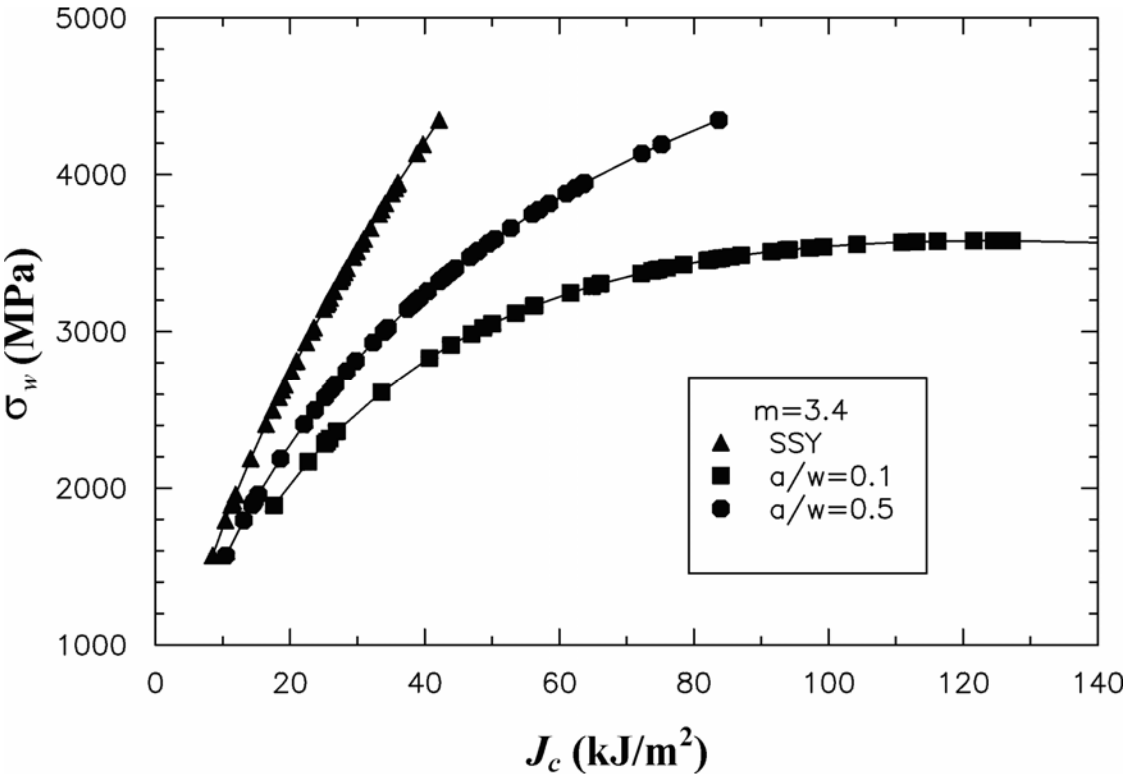

Fig. 5.36: Weibull stress as a function of J-integral for the converged calibration: T = -100°C, m = 3.4, Plate 100 material, 50 stochastically-generated SE(B) fracture toughness data points.

Once the Weibull models were calibrated, the Weibull stresses for the uniaxial loaded beams were analysed using finite element models. ORNL used a two-step process. A sharp tip model (Fig. 5.37) with a small root radius of 0.001 mm and containing 35,303 nodes and 7,580 elements was used to precisely calculate the through-thickness (average) fracture toughness $J_{applied}$ for both the top and bottom crack tips. Fig. 3.38 shows the blunt-tip model (with a finite root radius of 0.0254 mm) built with 39,353 nodes and 8,440 elements, which was used to calculate the stress and displacement fields for the Weibull stress calculation Both the calculations used material properties based on a temperature of –100°C (close to the bending test temperatures). ORNL's predictions for the Weibull stresses (σ_w) of the clad beam for the top and bottom crack tips as a function of applied longitudinal bending moment and of $J_{applied}$ are shown in Figs. 39 and 40 respectively. It can be seen that for a given applied bending moment the shallow crack-tip Weibull stresses are greater than those at the bottom-crack-tip. This is due to the fact that the shallow crack tip is farther away from the neutral axis of the beam during bending and is, therefore, subjected to a higher applied stress. On the other hand, this model also captures the difference in constraint effect at the different locations on the crack. The bottom-tip has higher constraint, and the Weibull stresses there are larger than those at the shallow tip for the same level of $J_{applied}$. Fig. 5.41 presents analogous results from the Framatome analysis, which considered both the clad and un-clad beam geometries. The former show somewhat more constraint loss for a given applied bending load.

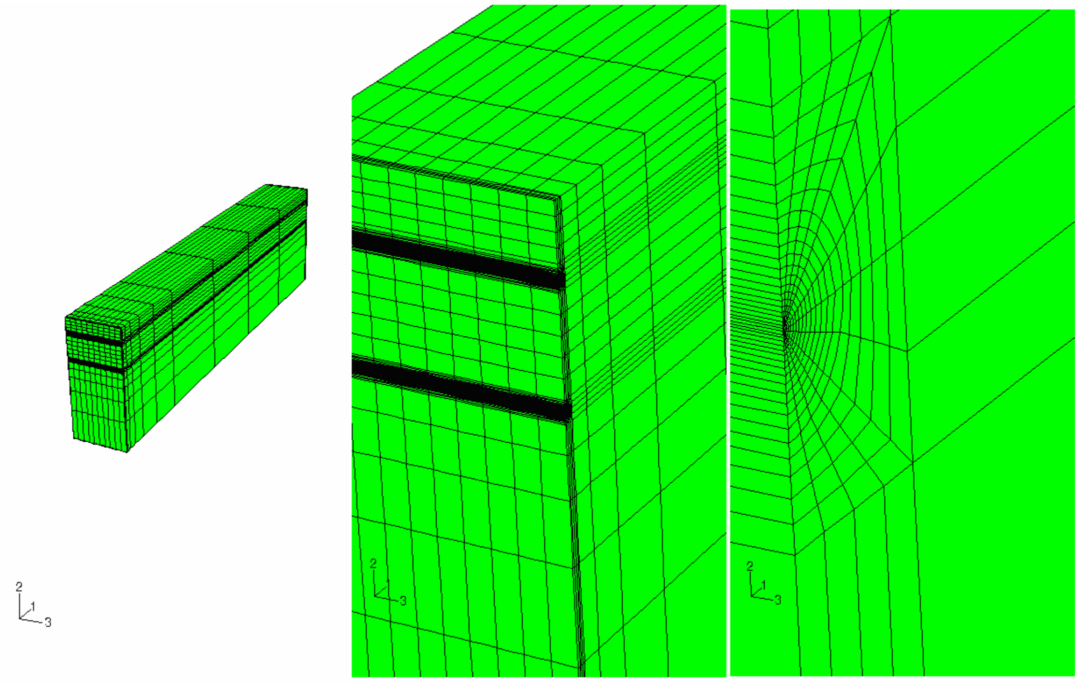

Fig. 5.37: Finite element 1/4 model of 4T beam specimen containing embedded sharp-tip flaw

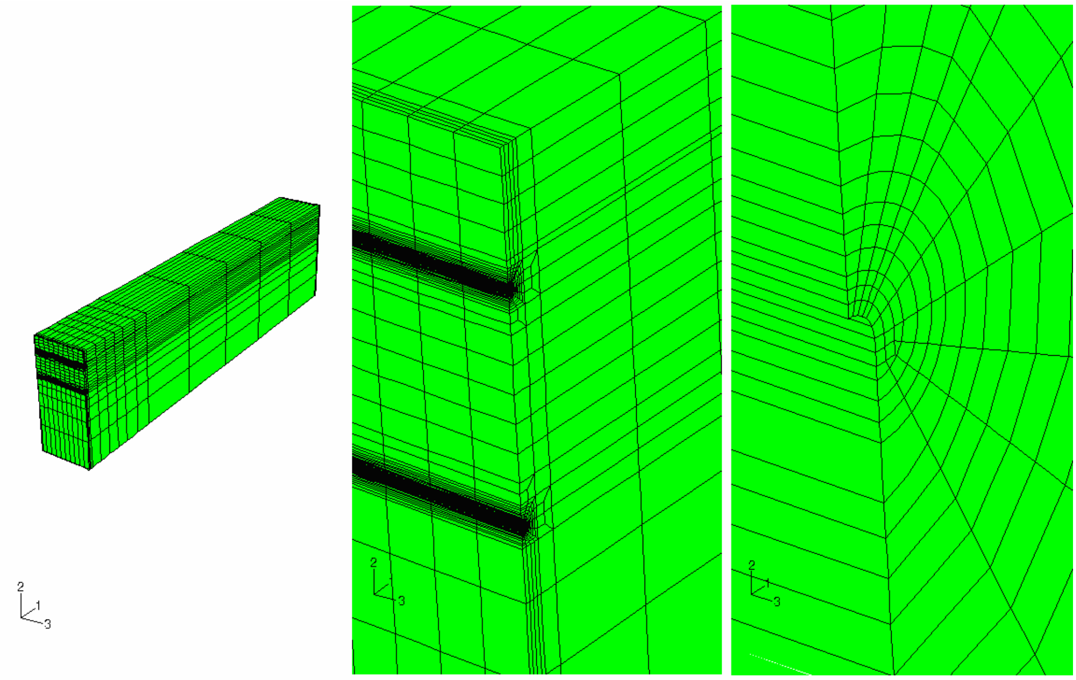

Fig. 5.38: Finite element 1/4 model of 4T beam specimen containing embedded blunt-tip flaws

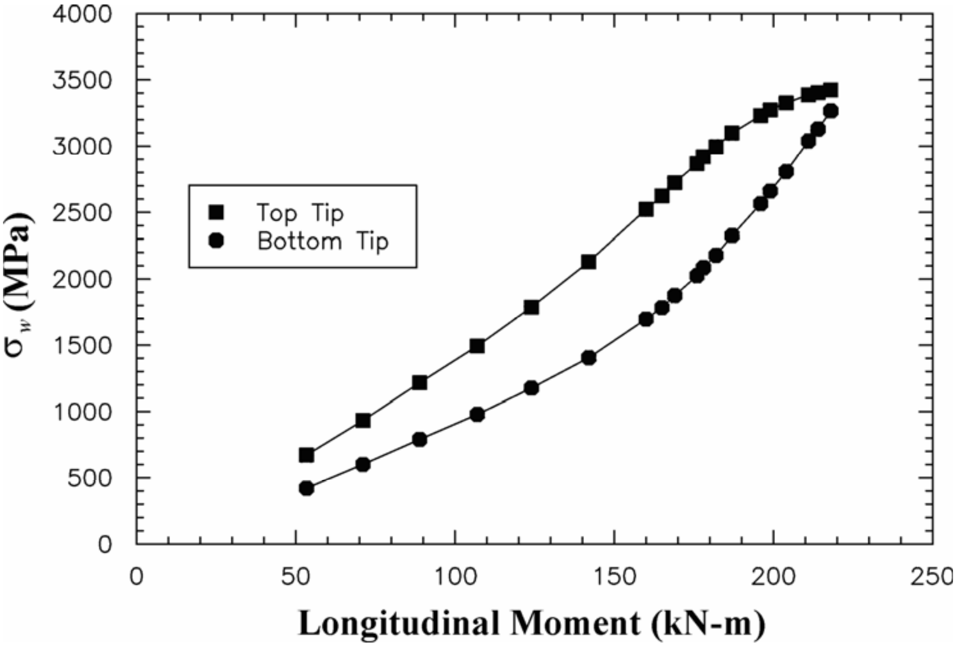

Fig. 5.39: Weibull stress load path for top and bottom crack tips as a function of applied bending moment (ORNL)

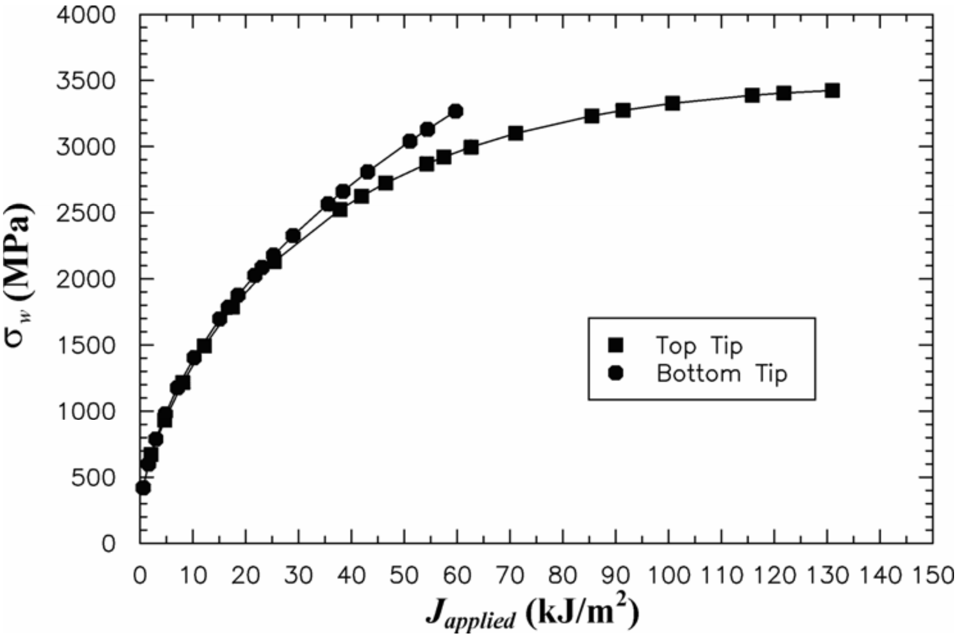

Fig. 5.40: Weibull stresses at the top and bottom crack tips as a function of applied driving force (ORNL)

An important objective of this analysis was to produce estimates of the probabilities of cleavage initiation (P_f) for both flaw tips (via eqn. 5.6). To determine which tip fails first during the bending, it is preferable to compare the P_f values at the two locations for the same bending moment rather than for the same J-Integral. The J_c dataset in the P_f vs. J_c relation was converted to corresponding longitudinal moment values using a polynomial approximation of $J_{applied}$ vs. bending moment. Fig. 5.42 shows ORNL's predictions for P_f at the shallow and bottom tips as a function of longitudinal bending moment. It is clear to see that the shallow tip is predicted to fail first during bending, even though the bottom tip has higher level of constraint.

Fig. 5.43 presents the P_f vs. bending moment results from the Framatome analyses of the clad and unclad beams. As already seen from the Weibull plots, the top-tip (upper crack) of the clad specimen is more likely to fail prior to the bottom-tip (lower crack), not due to higher crack front constraint, but only due to higher J-Integral values at same bending moment. With respect to the tests conducted at -93°C (4.2.1) and T = -77°C (4.2.2), these predictions (for a nominal temperature of -90°C) give reasonable failure probabilities at the experimental failure moments. The probability versus moment shows that the unclad beam fails at lower moments than the clad beam, but both crack fronts at the same time. The clad beam fails later and the top-tip (upper crack) slightly earlier than the bottom-tip (lower crack). If the failure probability is plotted versus CMOD, all specimens and crack fronts fail at practically the same value.

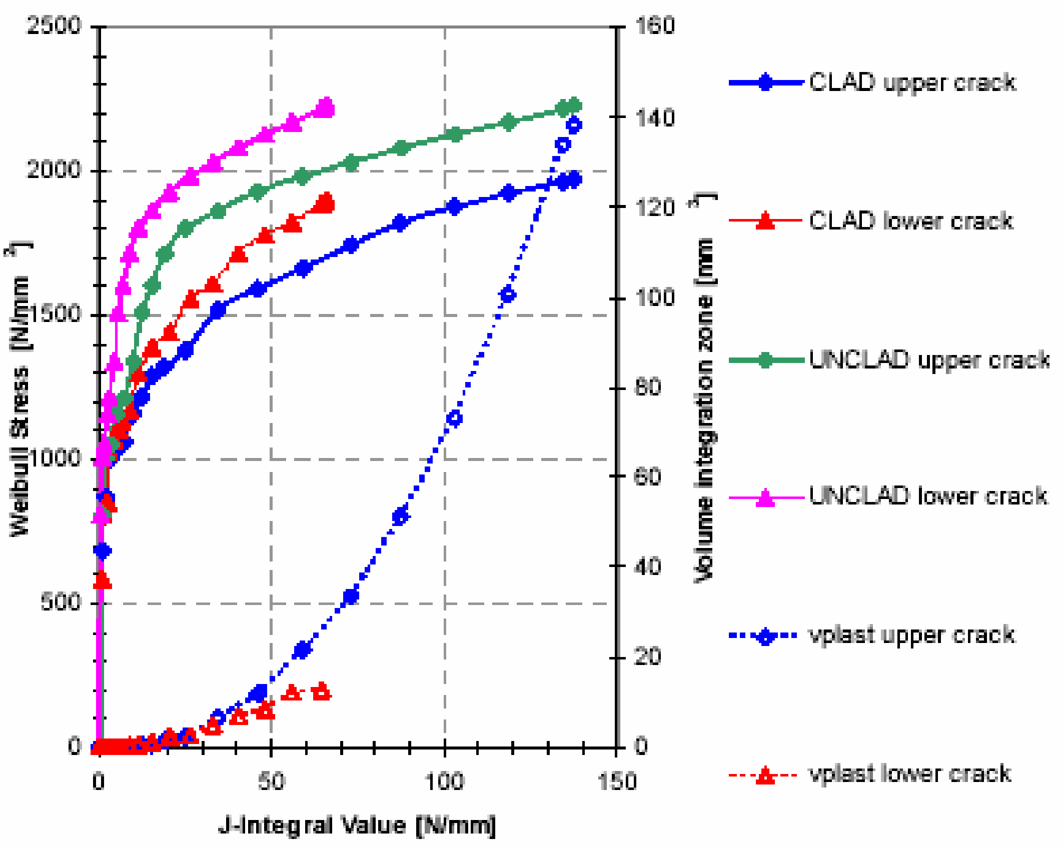

Fig. 5.41 Comparison of Weibull stress vs. J for clad and unclad specimens (Framatome)

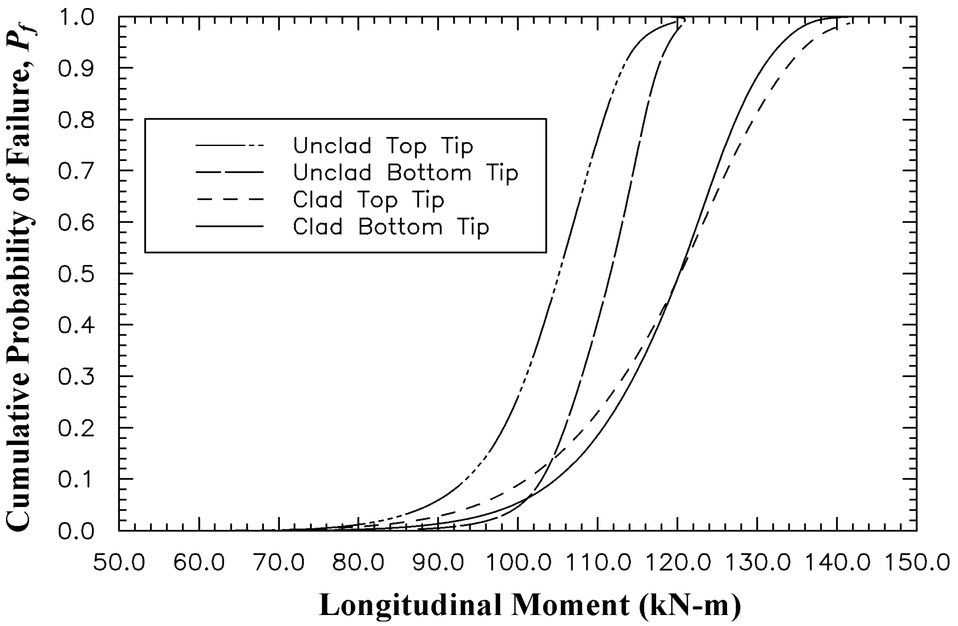

Fig. 5.42: Cumulative failure probabilities for the top and bottom crack tips as a function of applied bending moment (ORNL)

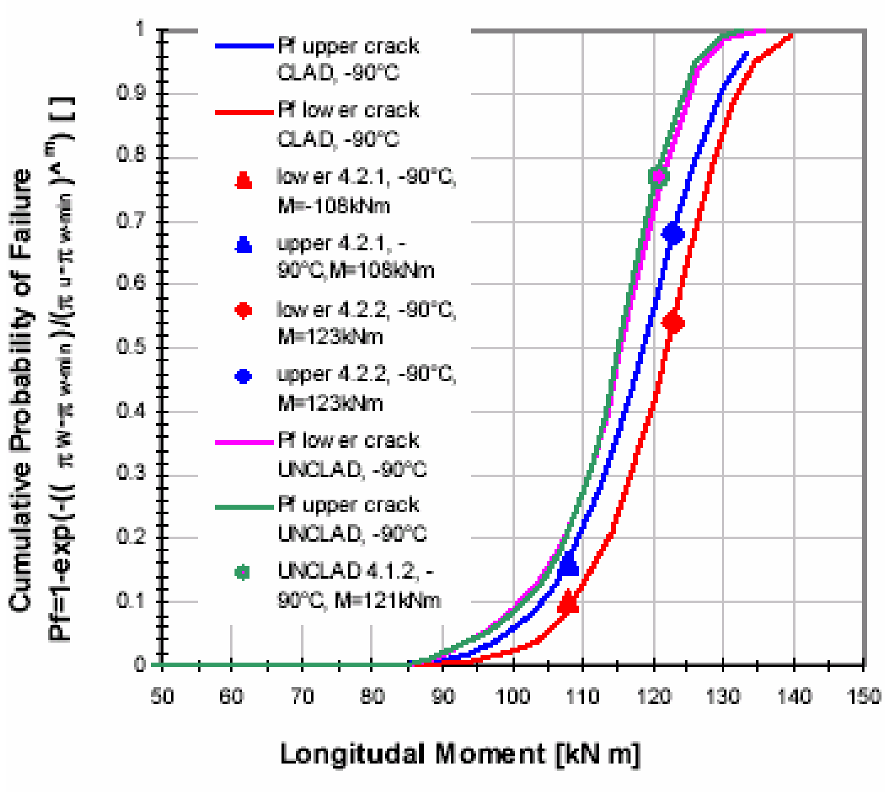

Fig. 5.43: Cumulative probability of failure vs. longitudinal moment & CMOD for cladded and uncladded beam at T=-90°C (Framatome)

6 DISCUSSION

6.1 Calibration of the Master Curve

The capability of the Master Curve to represent the transition behavior and the calibration of T_o parameter is the fundamental basis for the subsequent evaluation of transferability of the methodology to more complex flaw geometries and loading conditions. As detailed in Chapter 3 above, the ASTM E-1921 procedure was successfully applied to the fracture data for weld, Plate 100 and Plate 200. Fig. 6.1 shows the complete data set for high-constraint C(T) and SE(B) type specimens, plotted as function of $T-T_o$, where the T_o value corresponds to that for each data set. It is evident that for all three materials the mean Master Curve is consistent with the observed transition behavior in the range T_o ±25°C, and that data points fall with the limits defined by the 5% and 95% fracture probability curves.

Concerning the T_o estimates for the different specimen types and test conditions, a bias of +10 to + 15°C is expected between SE(B) and C(T) specimens types due to differences in constraint. However in the case of the weld, the T_o value from the C(T) tests was 21°C higher than that from the SE(B) tests. This result may have been influenced by several factors: the C(T) tests were conducted at a temperature at least 50°C above that of the SE(B) tests and at a different lab (albeit following the same testing standard) and finally intrinsic material variability. For the Plate 100 material, the T_o from the C(T) tests was 4°C below that determined from the SE(B) tests. Again in this case the fact that the C(T) and SE(B) tests were performed in different labs and material variability (as evidenced for instance by the difference in T_o between the Plate 100 and 200 materials) may have influenced the results. Overall it appears that, even if a common test standard is applied, some caution is needed in interpreting fracture test data from different data sets of limited size and scope.

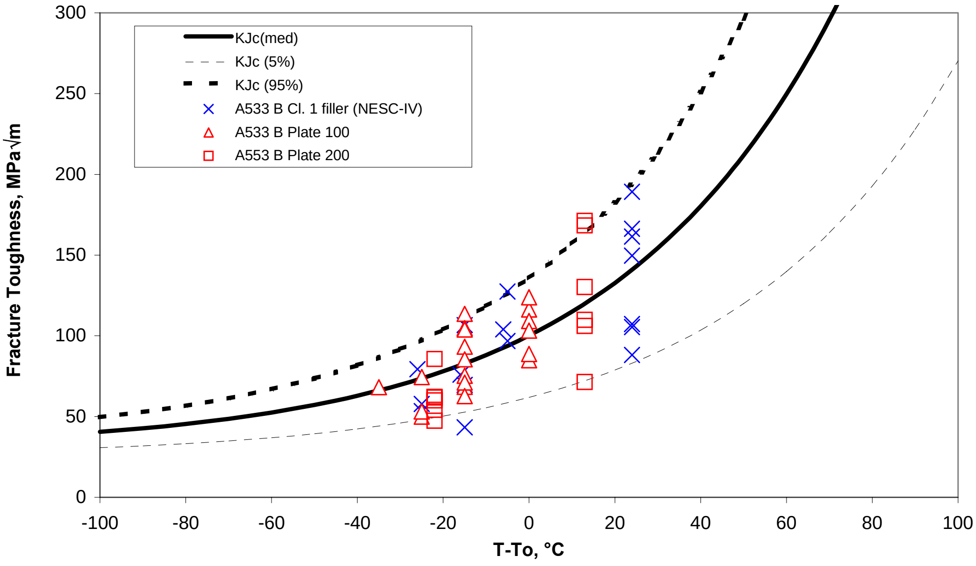

Fig. 6.1 Fit of the Master Curve to the high constraint fracture data for PVRUF weld, Plate 100 and Plate 200.

It is noted that the reference temperature RT_{To} values determined from the T_o estimates for the weld, Plate 100 and Plate 200 materials is consistently lower than the corresponding RT_{NDT} value. This trend is consistent with that observed in previous NESC projects on RPV steels [3, 4] and underlines the importance of using direct measurements of fracture toughness for best-estimate assessments.

A feature of the materials testing performed for the NESC projects has been the systemic inclusion of shallow-crack SE(B) specimens to quantify constraint loss effects and to provide a basis for calibration of constraint-based fracture mechanics models. Such tests are typically performed and evaluated according to the ASTM-E1921 procedure (substituting the $0.45 \leq a/W \leq 0.55$ requirement with a suitable crack front uniformity criterion, although this is not actually allowed in E1921). Fig. 6.2 compares the observed shift in T_o value for the weld and Plate 100 materials, together with results from similar test series performed in the NESC-I and NESC-II projects. For specimens with $a/W \approx 0.1$, it is seen that T_o is reduced by up to 40°C relative to that for deep flawed SENB specimens ($a/W \approx 0.5$). Here is important to note that such a comparison is best performed for specimens of same type, sampling location and test temperature range to minimize additional uncertainties as discussed above concerning the variability in T_o estimates for deep-flawed specimens. A further aspect concerns the validity range of a Master Curve determined for a specific shallow flaw geometry i.e. whether the valid temperature interval of $T_o \pm 50^{o}C$ for deeply cracked specimens is applicable. In the case of Plate 100 the shallow flaw tests performed over the range -80° to -130°C support such an assumption. A further aspect concerns the data scatter for low constraint specimens. For Plate 100 the lower bound toughness for the high and low constraint SE(B) tests was similar, although the mean toughness for a/W=0.1 is higher than for a/W=0.5. The Master Curve assumes that scatter in transition toughness is a function only of temperature. If scatter in the a/W=0.1 data is intrinsically greater than in deep cracked data, then caution is needed in using the Master Curve to extrapolate the low constraint data to other (higher) temperatures. In summary it would be useful to develop specific guidance for evaluation of shallow flaw test data in relation to appropriate selection of test temperatures and specimen measurement capacity.

The constraint loss effect reported above for standard and sub-size fracture mechanics specimens is compatible with the predictions of engineering methods such as those of Wallin [46], Sherry et al [28] and Gao et al [29]. The Wallin model assumes a universal 1:10 dependence between To and T-stress and hence requires no calibration. However the linear relationship means that the constraint loss effect may be overestimated for intermediate a/W values. In NESC-IV, tests with intermediate a/W values were only made for the Plate 100 material and the results could not be statistically differentiated from those for high constraint specimens, implying that the relationship between constraint loss and T-stress is indeed non-linear. In the case of the Sherry et al and Gao et al approaches, the magnitude of the T_o shift depends on the flow properties (E, σ_y) and the Weibull modulus, m. Determining m can be complex and for simplicity here a typical value 10 for brittle fracture of RPV steels is assumed (higher values in the range of 20 are more typical if prior ductile tearing is present). Both models provide very similar results, with a T_o in the range -35 to -40°C for the SE(B) a/W configuration. They also predict a non-linear decrease in T_o for decreasing T-stress, a feature which appears to correspond better with the a/W=0.2 experimental data for Plate 100, for instance. A point to note with all three models is that they are indexed to a “standard” high constraint T_o value. As discussed above, different deep flaw specimen geometries may provide lead to some variance in the T_o estimates and hence for any subsequent application to integrity assessment it should be ensured that the data most appropriate to the foreseen fracture conditions are used.

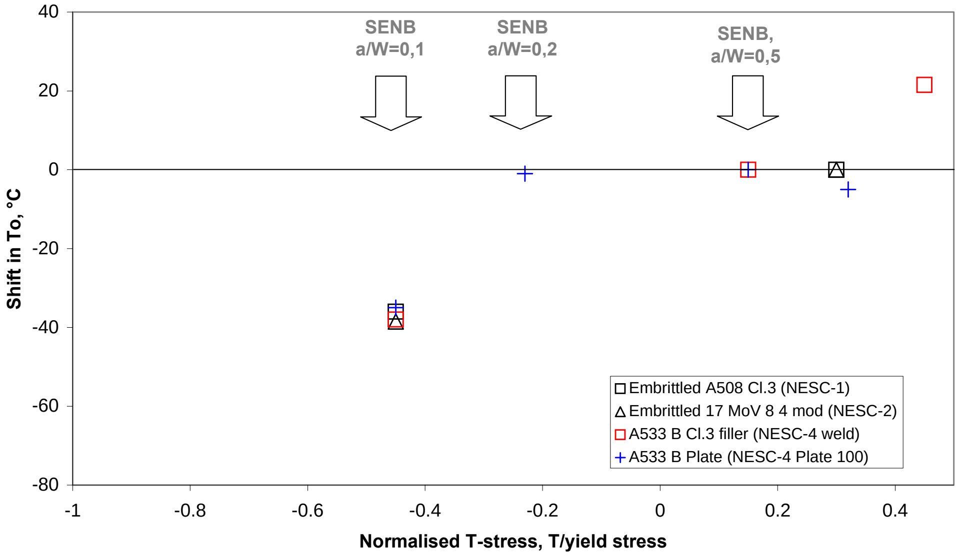

Fig. 6.2 Comparison of shift in T_o evidenced in tests on low constraint fracture mechanics specimens.

6.2 Experimental Evidence for Constraint Loss, Biaxial and Crack Front Length Effects

The NESC-IV project considered two specific situations in which very different constraint conditions arise. In the case of the clad cruciform specimens, the testing conditions covered a relatively shallow-flaw with biaxial bending load. For the embedded flaw beams, although the global loading was uniaxial, the situation of sub-surface crack tip at a highly loaded ligament was simulated. The influence of these features on the fracture behavior has been assessed in the first instance by comparison of the computed crack tip stress intensity values with the transition fracture behavior as represented by the Master Curve.

Considering firstly the biaxial beam tests, the tests results fell within the standard high-constraint 5% and 95% Master Curves for the weld material (with T_0 determined from C(T) specimens tested at a similar temperature). Since no uniaxial tests were performed, it is not possible to explicitly quantify the separate biaxial and shallow flaw effects). However it is clear that the results do not provide evidence of a substantial constraint loss effect and this leads to the hypothesis that the biaxial loading suppressed such effects, in particular at lower load levels. The results are therefore consistent with those from other biaxial test series reported in the literature (mostly also from the HSST program). Fig. 6.3 compares data from the NESC-IV biaxial tests with those from HSST Plate 14 [12], on an ORNL 533B weld [57], the so-called European reference material [58] and VVER-440 steel [59]. All the data points fall within the 5% and 95% bounds and are reasonably distributed about the mean (50%) curve. As to whether biaxial loading can actually reduce the fracture toughness below that predicted by a standard high constraint Master Curve, the limited NESC-IV biaxial data set is insufficient to allow conclusions to be drawn in this respect.

In the case of the embedded flaw beam tests conducted under uniaxial bending, the three tests conducted in the transition range (an initial test was performed in the lower shelf where no constraint effects occur) fractured at considerably higher crack driving force than would be predicted by the Master Curve approach. This effect can be directly attributed to constraint loss effects.

Lastly, in relation to crack front size effects, both the surface flaws in the biaxial beam test pieces and the embedded flaws had crack front lengths longer (60 and 101 mm respectively) than the standard 25 mm length used as a reference for the Master Curve. For comparing the experimental data with the Master Curve as described above, crack front length corrections based on the $(B/B_o)^{1/4}$ relationship used in the ASTM E1921 standard, where B is the crack front length of the geometry in questions and B_o is the reference value i.e. 25 mm. This procedure was elementary to apply for the embedded flaw beams, since the crack driving force is essentially uniform over the whole crack front. Since the latter is four times the reference value, so the effect of applying the correction is to raise the estimated K_J value. If uncorrected i.e. lower K_Js were used, the apparent constraint loss effect would be reduced but still evident. The situation for the semi-elliptic surface flaws is more complex since K_J varies over the crack front. Effective i.e. crack front size-corrected values of K_J, can be calculated by an integral procedure, providing the K_J distribution as a function of increasing applied load is known. In the present case applying this correction reduced the overall spread of K_{Jc} values and improved the correlation of the experimental data with the standard Master Curve. In summary, while the NESC-IV experiments did not explicitly test the Master Curve crack-front size dependence, however application of the standard correction produces consistent agreement between the experimental results and the constraint-based Master Curve models.

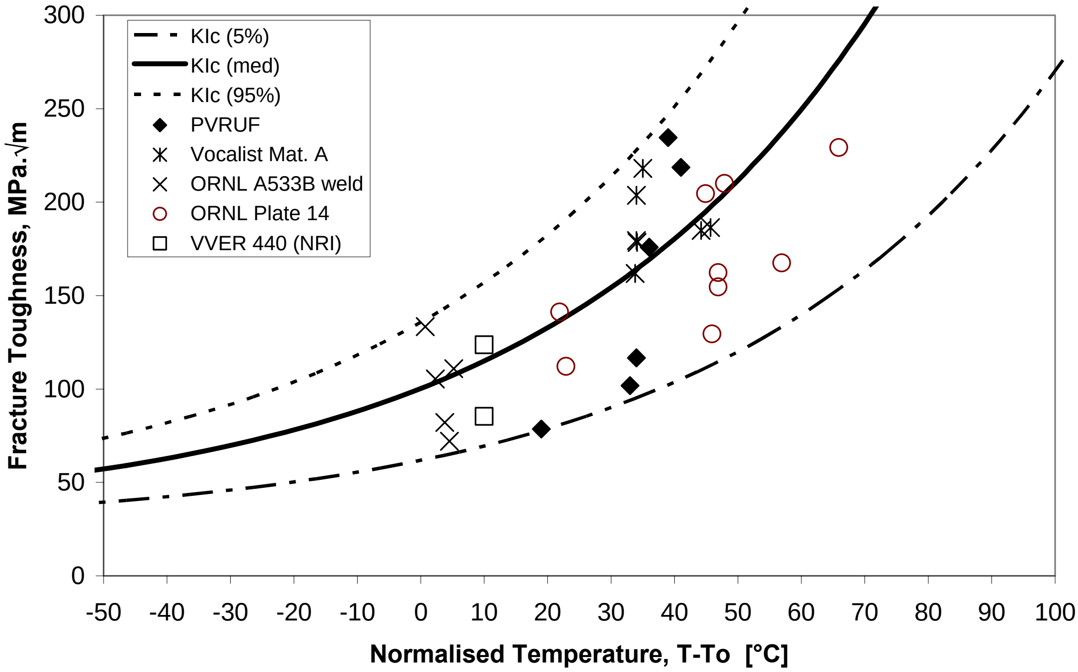

Fig. 6.3 Comparison of the results of the NESC-IV biaxial tests on shallow flaw test pieces with the standard Master Curve; the T_o values correspond to that determined from standard high constraint tests for the relevant material.

6.3 Constraint Parameters

The NESC-IV tests have provided a basis for investigating different aspects of several constraint-based facture mechanics approaches for assessing the behavior of flaws in the transition regime. These rely in the first instance on determination of constraint parameters describing the crack-tip constraint; for non-standard geometries such as the NESC-IV test pieces, these parameters need to be calculated from crack-body elasto-plastic finite element analyses. The post-test analyses focused largely on two parameters: T-stress and Q (defined in terms of σ_1). Other parameters considered were h, the stress triaxiality factor (σ_h/σ_e) and q, the quotient of multiaxiality.

In the case of the uniaxial embedded flaw beams, the situation is relatively straightforward since all three parameters predict increasing constraint loss with increasing load. For the biaxial tests with surface flaws, the situation is rather more complex since the level of constraint varies over the crack front and is potentially affected by the biaxial nature of the loading. Firstly, it is noted that under simulated uniaxial loading conditions for this flaw geometry, the T-stress and Q parameters predict constraint loss at both the HAZ and deepest point positions on the crack front. As discussed above, the experimental data do not provide any evidence of such predominant constraint loss effect, implying that the effect of the out-of-plane loading needs also to be considered. For the simulations with the biaxial loading, the predictions for the deepest point are the same as for uniaxial loading i.e. constraint loss is predicted. For the near-surface area where the crack driving force is at its maximum, the T-stress value indicates high constraint at all loads (the T-stress is always positive); Q predicts that high constraint is maintained up to a K_J value of 100 MPa.√m, after which it drops rapidly; h predicts some constraint loss in the HAZ and constraint increase (to the level typical of C(T) specimens) at the deepest point. It is also necessary to consider the fractographic evidence in combination with these predictions. The findings (see section 4.1.4 above) suggest that majority of the initiation sites occurred at or slightly below the HAZ, with only one instance of initiation close to the deepest point.

It appears, therefore, that the T-stress parameter provides the most consistent representation of the constraint observed for the NESC-IV test piece geometries, with the provisos that, when present, out-of-plane loading must be taken into consideration and that the T-stress variation over the full crack front needs to be checked to establish the most constrained location. It is however noted that for some other flaw geometries and loading combinations, for instance the straight-fronted flaws in the HSST-14 and Vocalist biaxial bend tests, the T-stress parameter can predict a constraint loss effect that is not supported by experimental results. Under such circumstances the so-called “hydrostatic Q” parameter may be preferable [60].

6.4 Engineering Assessment Methods

Two constraint-modified engineering approaches for fracture assessment were considered in the project: the R6 FAD methodology and the Wallin T-stress method. Attention was focused on the uniaxial bend tests on the embedded flaw test pieces, for which a marked constraint loss effect was obtained.

R6 FAD Assessment

From the analyses described in section 5.2 above, it is clear that the R6 constraint methodology can be very successful in predicting the observed behaviour during the embedded flaw beam tests, given appropriate material and structural constraint data. The non-conservatism in the prediction of the first test is not a serious concern. This test was performed under small scale yielding conditions where no constraint effects are expected, and would be conservatively predicted using the toughness at 5% failure probability irrespective of the size correction used.

However, the lack of fully representative fracture toughness data meant that relevant data have been inferred using the Master Curve methodology, in an attempt to include the effects of temperature, crack front length, constraint, and plate-to-plate variability. There are four key areas where its applicability was examined:

1. Does the Master Curve provide an adequate description of the effect of temperature on transition toughness under high constraint conditions, for the materials used? If it does, then the difference in test temperature between the embedded flaw beams and many of the fracture toughness specimens is not an insuperable problem.

The general ability of the Master Curve to match the temperature variation of transition toughness in RPV steels is well established. As discussed in section 6.1 above, the Master Curve is considered to provide a reasonable description of the effect of temperature on fracture toughness for Plate 200 material under high constraint conditions. Furthermore the test temperatures for Plate 200 at a/W=0.5 ranged from -70°C and -110°C, thus conveniently straddling the temperatures of three of the four embedded flaw beam tests.

2. Is its methodology for size-correction appropriate? Most of the test specimens were 10mm thick, and the fracture toughness data from these specimens were size-corrected to 25mm. The test beams were 100mm thick.

Size correction to B=25mm from a smaller test specimen thickness is a fundamental part of the Master Curve procedure, and must be considered reasonably well established over the modest corrections usually employed. Thus a further size correction from B=25mm to B= 100mm is not unreasonable. That said, there are no specific data available in this project to judge its validity, since no 100 mm thick deep-cracked specimens were tested. It is noted that the B=100mm i.e. size-corrected, assessments do provide a slightly better correlation with the test results.

3. Can the effect of constraint loss in fracture toughness specimens be adequately described by a shift in T_o?

The ability of the Master Curve to describe fully the effect of constraint loss on transition toughness over the relevant temperature range has also to be considered. During the post-test analyses, only fracture toughness data of a/W=0.1 specimens from plate 100 over a temperature range from -130°C to -110°C. Subsequent additional tests performed at -80°C towards the end of the project provided evidence that the T_o shift established for the lower temperatures was also valid for higher values.

4. Is it reasonable to use the Master Curve to transfer plate 100 data to plate 200?
Comparison of the fracture toughness data for Plates 100 and 200 at a/W=0.5 shows that there is very little difference between the two plates at this constraint level. It is thus reasonable to assume that the same will hold at other constraint levels.

Wallin T-stress Model

The second engineering approach examined in detail was the Wallin T-stress model, which prescribes a proportional relationship between the T-stress constraint parameter and a shift in T_o. As such, the points raised above concerning assumptions made in applying the Master Curve are relevant in this case also, and do not need to be repeated. The following comments are therefore focused on areas where the approaches differ. The simple linear form and prescribed slope of the Wallin T-stress constraint correction function (see eqn.(5.9)) has a considerable advantage in that no calibration is required. In contrast for the engineering models with non-linear constraint correction such as R6 or the local approach methods, the requirement of having access to fracture test data at two or more constraint conditions for a given material condition is frequently difficult to satisfy in practical situations.

Against this, the model predicts a constraint loss effect when the T_{stress} is only slightly negative. For example, in the case of the Plate 100 material the SE(B) tests with a/W=0.2 produced a T_o value equivalent to that obtained for fully constrained conditions, although the Wallin model predicted a shift of –15°C. Similarly, for the embedded flaw beam test conducted at -128°C and which failed under essentially elastic conditions, the model also predicts a slight loss of constraint, which was not observed experimentally. Some caution appears therefore appropriate if the T-stress/σ_y ratio lies in the range 0 to –0.25 for the flaw being assessed, but it should be noted that only a limited number of tests were performed using a geometry expected to show a small loss of constraint and the results obtained were within the scatter band of the standard a/W=0.5 specimens. It is noted that this effect is somewhat offset by the upwards shift implicit in eqn.(5.9).

Lastly, the apparent discrepancy between the representation of the constraint loss functions in Figs. 5.29 (ΔT_o vs. T-stress/σ_y) and 5.31 (K^c_{mat}/K_{mat} vs. -βL_r) deserves some comment. In the former the Wallin model is shown to slightly underestimate the T_o shift observed in the SE(B) a/W=0.1 tests, whereas in the latter R6 representation, it apparently overestimates the constraint loss effect. This effect is attributed to fact that in Fig. 5.31 the -βL_r term is defined in terms of Q rather than T-stress. If the latter parameter is used, then -βL_r ~ T-stress/σ_y, and the SE(B) data points for a/W = 0.2 and 0.1 would be shifted leftwards to values of approximately 0.25 and 0.5 respectively, in better correspondence with the Wallin model curve. Under these circumstances, the predictions of the R6 approach would be expected to lead to results consistent with those obtained from direct application of the Wallin model.

6.5 Feature Test Design

In designing the NESC-IV tests, the major objective was to produce brittle cleavage fracture under constrained yielding conditions. Once the overall test piece geometry had been decided, the selection of the test temperature was the critical issue. Too low a temperature would result in failure under lower shelf conditions, for which no constraint loss effect occurs. Too high a temperature risked producing failures under large scale yielding conditions, which are not relevant to practical flaw assessment conditions and could risk ductile tearing prior to cleavage. In terms of the R6 methodology, the aim was to achieve failure in the absence of constraint effects at L_r between 0.6 and 0.7. Since most assessment procedures contain in-built conservatism, producing accurate best-estimates for tests in which ±10°C can make a considerable difference to the fracture behavior is a challenge. In fact the pre-test fracture analyses produced initial test temperature recommendations for the both the biaxial bend and embedded flaw beams that proved too low. This was attributed to a number of factors, including differences of opinion on crack front size correction, some over-estimation of constraint loss for the embedded flaw beam and the fact that the K_J values for both geometries were calculated using “nominal” temperature-independent stress-strain properties. With the benefit of the test results themselves, more materials data and the detailed post-test analyses, some recommendations for future feature testing can be given.

a) Biaxial bend tests: the tests results add further weight to the ORNL experience that such tests be performed at a temperature of at least T_o+20°C. Since no constraint loss is expected it is important that the T_o estimate was based on high constraint C(T) specimens. While the Master Curve provides a valid means of predicting the dependence of mean fracture toughness on temperature, uncertainty should be minimized by performing the fracture tests at a temperature close to that envisaged for the biaxial tests.

b) Embedded flaw uniaxial bend tests: in this case successful tests were performed in the range T_o to T_o+20°C. The selection of test temperature was complicated by the unique embedded flaw geometry adopted. Under the test conditions used, the near-surface tip experiences unconstrained yielding, with $L_r \sim 1$. This means that substantial constraint loss occurred and indeed it is unclear whether fracture initiated at this tip or at the deep tip (although it must also be borne in mind that the deep tip was not pre-cracked). Hence for further tests on this geometry (for which specimens have now been fabricated), it could be argued that some reduction of the test temperature from -93°C would favour fracture at the near-surface tip. However such a reduction would have to be modest, since i.e. <10°C, to avoid lower shelf behaviour for which there are no constraint loss effects. A further aspect concerns the flaw geometry; for instance blunting the deep tip (by drilling a hole through the beam for instance) or extending the flaw to the neutral axis of the beam could suppress fracture initiation at that location, thus removing any ambiguity concerning the fracture initiation location. However this would require new FE analysis to quantify the crack tip loading parameters.

7 CONCLUSIONS AND RECOMMENDATIONS

The NESC-IV project has addressed the transferability of fracture toughness data from laboratory specimens to its use in integrity assessment methods for reactor pressure vessels subject to upset and normal loading transients, considering in particular the Master Curve approach for describing the temperature dependence of toughness in the transition regime. The main experimental focus was on two series of large-scale features tests performed at ORNL under the HSST program. To complement these extensive materials testing and fracture analyses were performed by a group of twenty European organizations, coordinated by the Network for Evaluating Structural Components (NESC). The main conclusions are as follows:

- A series of six biaxial bend feature tests on weld material specimens containing a shallow semi-elliptical surface flaw were successfully conducted, producing cleavage fracture. Since the calculated K_{Jc} values are consistent with the standard Master Curve, no constraint loss effect is considered to have occurred; this is attributed to the out-of-plane loading.

- The feasibility of generating fracture data for simulated embedded flaws was successfully demonstrated in a demonstration series of four uniaxial bend beam tests on plate material. All the tests ended in a brittle fracture event and it proved impossible to determine experimentally whether initiation had occurred first at the near surface tip or the deep tip. The calculated K_{Jc} values lay well above the relevant Master Curve, indicating a substantial constraint loss effect.

- A substantial database of mechanical and fracture properties data has been established for the PVRUF weld and plate materials and is available as an Excel workbook file.

- Concerning the application of the Master Curve, the following aspects are noted:
  - The Master Curve provided an adequate description of the transition toughness under high constraint conditions for the materials used. In the case of the weld material, the bias in the T_o estimates between SE(B) and C(T) specimens, albeit tested at temperatures 50°C apart, was somewhat greater than expected. This underlines the desirability of having fracture data as close as possible to the assessment conditions for best-estimates analyses.
  - Size correction to B=25mm from a smaller test specimen thickness is a well established part of the Master Curve procedure. While NESC-IV did not produce specific data to judge the validity of applying the same correction procedure to longer crack lengths, it is noted the size-corrected assessments (both for the 60 mm semi-elliptical crack front with non-uniform loading and for the straight 100 mm crack front of the embedded flaw) are in good agreement with standard fracture test results.
  - The data from shallow-flaw SE(B) specimens indicate effect of constraint loss in fracture toughness specimens can be described by a shift in $T_{o.}$ The extent to which this effect is valid over a wider temperature range than that used in the tests themselves was shown in the case of the Plate 100 material to span a temperature range of T_o-35°C to T_o+15°C.
  - The RT_{To} reference temperature was found to be 10°C or more lower than the RT_{NDT} value for all the materials considered and underlines the benefits of using direct measurement of fracture toughness for best-estimate analyses.

- Detailed finite element analysis proved essential to analyzing both the feature tests. With measured stress-strain curves for the relevant materials over the relevant temperature range, it was possible to accurately predict the overall force-deformation of the test pieces. The estimates of K_{Jc} were generally within ±10%, which is similar to the inter-team consistency observed in previous NESC projects. In those cases in which constraint related parameters were calculated, the teams also produced comparable results and trends.

- Quantification of crack-tip constraint loss was studied principally via the T-stress and Q parameters. In the case of the uniaxial embedded flaw beams, both parameters predict increasing constraint loss with increasing load. For the biaxial tests with surface flaws, the level of constraint varies over the crack front and is affected by the biaxial nature of the loading. Overall the T-stress parameter provided the most consistent representation of the constraint effects observed for the NESC-IV test piece geometries, with the provisos that, when present, out-of-plane loading must be taken into consideration and that the T-stress variation over the full crack front needs to be checked to establish the most constrained location. In general, caution is essential before applying any constraint effect model to a geometry/loading regime for which its applicability has not been satisfactorily established.

- The application of the R6 constraint modified procedure and the Wallin T-stress model were verified for the embedded flaw beam tests. The prediction that the load carrying capacity of at temperatures in the range of T_0 is increased by over >30% is supported by the experiment results. The Wallin model has a major advantage in the fact that no calibration data is needed; however its assumption that constraint loss is directly proportional to T-stress is not supported sufficiently by the NESC-IV data for conditions of only modest constraint loss.

- The local approach Beremin model using the Weibull stress was successfully calibrated from fracture data for the SE(B) a/W=0.5 and a/W=0.1 geometries by applying the G-R-D procedure, although the value of the Weibull parameter m proved sensitive to whether the Weibull stress term was defined in terms of the crack opening stress σ_1 or the hydrostatic stress σ_H. Both formulations proved capable of predicting the constraint-loss effects observed in the uniaxial bend tests on embedded flaw beams. The σ_H-based model was also shown to predict the effect of out-of-plane biaxial loading in suppressing constraint loss.

The following additional recommendations are made:

- The embedded flaw beam test series should be continued, using the specimens already fabricated, so as to provide a more statistically reliable data set for benchmarking the constraint loss assessment methods.
- Effort should be addressed to collating all available data on low constraint test specimens for reactor pressure vessel steels, with a view to confirming the validity of the Master Curve T_o shift approach and to providing guidelines for evaluating such tests.
- Further studies should be made on local approach methods, in particular to improve the reliability of the calibration of the Weibull shape parameter m and to extend their use for predicting the practical limits to application of engineering models, for instance concerning flaw geometry and out-of-plane loading.

REFERENCES

1. Rintamaa R., Taylor N., NESC Benchmark Tests to Support Improved Structural Integrity Assessment, SMiRT-17, August 2003
2. N. Taylor & D.P.G. Lidbury, Improving Structural Integrity Assessment Techniques, Proc. 1st Symposium - Nuclear Pressure Equipment Expertise and Regulation, Dijon, June 2005
3. Bass B.R, J. Wintle, R. Hurst and N. Taylor, NESC-1 Project Overview, European Commission, EN 19051
4. Stumpfrock, L., Swan, D.I., Siegele, D., Taylor, N., Nilsson, K.F., Minnebo, P., NESC-II Final Report - Brittle Crack Initiation, Propagation And Arrest Of Shallow Cracks In A Clad Vessel Under Pts Loading , NESCMAN (02) 07, EUR 20696 EN, March 2003
5. Theiss, T. J. and Shum, D. K. M., “Experimental and Analytical Investigation of the Shallow-Flaw Effect in Reactor Pressure Vessels,” USNRC Report NUREG/CR-5886 (ORNL/TM-12115), Oak Ridge National Laboratory, Oak Ridge, Tennessee/USA, July 1992.
6. Theiss, T. J., Bass, B. R., Bryson, Jr., J. W., McAfee, W. J., Nanstad, R. K., Pennell, W. E., and Rao, M. C., “Initial Results of the Influence of Biaxial Loading on Fracture Toughness,” USNRC Report NUREG/CR-6036 (ORNL/TM-12349), Oak Ridge National Laboratory, Oak Ridge, Tennessee/USA, June 1993.
7. McAfee, W. J., Bass, B. R., and Bryson, Jr., J. W., “Development of a Methodology for the Assessment of Shallow-Flaw Fracture in Nuclear Reactor Pressure Vessels,” *ASME Pressure Vessel and Piping Conference*, Orlando, Florida/USA, July 27-31, 1997, PVP Vol. 346, pp. 85-94.
8. Pennell, W. E., Bass, B. R., Bryson, Jr., J. W. , Dickson, T. L., and Merkle, J. G., “Preliminary Assessment of the Effects of Biaxial Loading on Reactor Pressure Vessel Structural-Integrity-Assessment Technology,” *Proceedings of 4th ASME/JSME International Conference in Nuclear Engineering*, New Orleans, Louisiana/USA, March 10-14, 1996.
9. McAfee, W. J., Bass, B. R., Bryson, Jr., J. W., and Pennell, W. E., “Biaxial Loading Effects on Fracture Toughness of Reactor Pressure Vessel Steel,” USNRC Report NUREG/CR-6273 (ORNL/TM-12866), Oak Ridge National Laboratory, Oak Ridge, Tennessee/USA, March 1995.
10. Bass, B. R., Bryson, Jr., J. W., Theiss, T. J. and Rao, M. C., “Biaxial Loading and Shallow-Flaw Effects on Crack-Tip Constraint and Fracture Toughness,” USNRC Report NUREG/CR-6132 (ORNL/TM-12498), Oak Ridge National Laboratory, Oak Ridge, Tennessee/USA, January 1994.
11. Bass, B. R., McAfee, W. J., Bryson, Jr., J. W., and Pennell, W. E. “Determination of Cladding Effects on Shallow-Flaw Fracture Toughness of Reactor Pressure Vessel Steel under Prototypic Biaxial Loading,” *5th International Conference on Nuclear Engineering*, Nice, France, May 26-30, 1997.
12. Bass, B. R., McAfee, W. J., Williams, P. T., and Pennell, W. E., “Evaluation of Constraint Methodologies Applied to a Shallow-Flaw Cruciform Bend Specimen tested under Biaxial Loading Conditions,” *Fatigue, Fracture, and High Temperature Design Methods in Pressure Vessels and Piping, ASME/JSME Joint Pressure Vessels and Piping Conference*, San Diego, California/USA, July 26-30, 1998, PVP-Vol. 365, pp. 11-25.

13. Bass, B. R., McAfee, W. J., Williams, P. T., and Pennell, W. E., "Fracture Assessment of Shallow-Flaw Cruciform Beams tested under Uniaxial and Biaxial Loading Conditions," *Nuclear Engineering and Design*, Vol. 188, No. 3, 1999, pp. 259-288.
14. ASTM E 1921-97, Test Method for the Determination of Reference Temperature, T_o, for Ferritic Steels in the Transition Region, American Society for Testing and Materials, West Conshohocken, PA, 1998.
15. NESC-IV Project Interim Report, Bas, B.R., W.J., McAfee, Williams, P.T, Swan, D.I, Taylor, N.G., Nilsson, K-F, Minnebo, P, NESCDOC MAN (02) 04
16. Lidbury, D.P.G, Validation of Constraint Based Methodology In Structural Integrity – Project Overview and Update, Proc. ASME PVP 2005, San Diego, USA
17. Bass, B. R. et al., "Development of a Weibull Model of Cleavage Fracture Toughness for Shallow Flaws in Reactor Pressure Vessels," ICONE9 Paper No. ICONE9051, Nice, France, April 2001.
18. Williams, P.T., Bass, B.R., and McAfee, W.J., "Application of the Weibull Methodology to a Shallow-Flaw Cruciform Bend Specimen Tested under Biaxial Loading Conditions," *Fatigue and Fracture Mechanics*, STP 1389, American Society of Testing and Materials, West Conshohocken, PA, 2000.
19. NESC IV Project Work Programme, Biaxial Fracture Toughness Testing and Analysis of Shallow Flaws in RPV Materials, NESCDOC MAN (00) 08, October 2000.
20. Nilsson, K-F. and Bass R., (2001), NESC-IV Pre-Test Problem Definition Document, NESCDOC TG3 (2001) 01
21. Nilsson, K.-F. et al, NESC-IV Post-Test Problem Definition Document, NESCDOC TG3 (2002) 05, July 2002
22. NESC IV Project Work Programme, Biaxial Fracture Toughness Testing and Analysis of Shallow Flaws in RPV Materials, NESCDOC MAN (00) 08, October 2000.
23. NESC-IV Database Version 7.1 (September 2004)
24. W. Oldfield, in T. R. Mager ed., "Reference Fracture Toughness Procedures applied to Pressure Vessel Materials", MPC-24, ASME 1984, papers presented at the Winter 1984 annual meeting of the ASME, New Orleans, 1984.
25. J. D. G. Sumpter and A. T. Forbes. Constraint Based Analysis of Shallow Cracks in Mild Steels, Proc. Int. Conf., *Shallow Crack Fracture Mechanics, Toughness Tests and Applications*, TWI, 1992.
26. Y Kim and K-H Schwalbe. *ASTM Journal of Testing & Evaluation*, 2001.
27. R6 procedure rev 4, section 3.7, April 2001.
28. Sherry, M.A. Wilkes, D.W. Beardsmore and D.P.G. Lidbury, Material Constraint Parameters for the Assessment of Shallow Defects in Structural Components – Part 1: Parameter Solutions, Engineering Fracture Mechanics, 72 (2005), pp.2299-2426
29. X. Gao, R.H. Dodds, R.L.Tregoning and J.A. Joyce, Prediction of the T_o shift between specimens of different constraints using the T-stress based τ-functions, Int. J. Fracture 104; L3-L8, 2000
30. J. Mendes, N. Taylor, F. Hukelmann, L. Metten. Fabrication Report for the 2nd Series of Embedded Flaw Beams, NESCDOC (04) 08, April 2005

31. I. Sattari-Far, Study on Fracture Behaviour in Clad Cruciform Specimens under Biaxial Loading, Transactions of the 17th International Conference on Structural Mechanics in Reactor Technology (SMiRT 17), Prague, Czech Republic, August 17 –22, 2003, Paper # G02-11
32. I. Sattari-Far, Post-Test Analysis Of Uniaxial And Biaxial Tests Of NESC-IV (Final FEM and R6 analyses), Annex 1, Minutes of the NESC-IV Progress Meeting, Lymm (UK), January 2004, NESC DOC (04) 01
33. S. Yin et al, Application of a Weibull Stress Model to Predict the Failure of Surface And Embedded Cracks In Large Scale Beams Made of Clad And Unclad RPV Steel, Proc. ASME PVP-2004, San Diego, 2004
34. S. Yin et al, Effect of Shallow Flaws and Biaxial Loading on Transition Temperatures Using a Weibull Stress Model, Proc. ASME Int. Conf. PVP-2004, San Diego, USA, July 2004
35. Gao, X., Ruggieri, C. and Dodds, R. “Calibration of Weibull Stress Models Using Fracture Toughness Data” *Int. J. Frac.* **92**, (1998) 175-200.
36. L. Stumpfrock, MPA Report, October 2003
37. L. Stumpfrock, Minutes of the NESC-IV Progress Meeting, Lymm, UK, January 2004, NESC DOC (04) 01
38. A.H. Sherry et al, Compendium of T-Stress Solutions for Two and Three Dimensional Cracked Geometries, Fatigue Frac. Engng. Mater. Struct. Vol 18, No. 1, pp.141-155, 1995
39. I. Varfolomeyev & D. Siegele, Fraunhofer IWM, Germany), private communication, January 2005
40. V Radu, Finite element crack analyses: K, J and CMOD parameters & structural integrity analyses, received by email, Institute for Nuclear Research, Pitesti, Romania, September 2004.
41. K. Wallin and R. Rintamaa, Use of the Master Curve Methodology for Real Three Dimensional Cracks, Proc. 18th International Conference on Structural Mechanics in Reactor Technology (SMiRT 18), Paper G01-5, Beijing, China, August, 2005
42. C. Betegon and J.W. Hancock, Two parameter characterisation of elasto-plastic stress fields, J. Appl. Mech., 1991, 58(1), p.104-110.
43. J.D.G. Sumpter and J.W. Hancock, Status review of the J plus T stress fracture analysis method, Proc. European Conference on Fracture 10, EMAS, 1994
44. N P O’Dowd and C F Shih, “Family of crack tip fields characterised by a triaxiality parameter: part I – structure of fields", J. Mech. Phys. Solids, Vol. 39, pp. 989-1015, 1991.
45. N P O’Dowd and C F Shih, “Family of crack tip fields characterised by a triaxiality parameter: part II – fracture applications”, J. Mech. Phys. Solids, Vol. 40, pp. 939-963, 1992.
46. K. Wallin, Quantifying T_{stress} controlled constraint by the master curve transition temperature T_o, Eng. Frac. Mec., 68 (2001), 303-328
47. F M Beremin, "A local criterion for cleavage fracture of a nuclear pressure vessel steel", Met. Trans., Vol. 14A, pp. 2277-2287, 1983.
48. Margolin B.Z., Rivkin E. Yu., Karzov G.P., Kostylev V.I., Gulenko A.G., New approaches for evaluation of brittle strength of reactor pressure vessels., Trans. of SMiRT-17, Prague, Czech Republic, 2003.
49. Margolin B.Z., Kostylev V.I. Analysis of biaxial loading effect on fracture toughness of reactor pressure vessel steels, Int. J. Pres. Vess. Piping, v.75, 1998, pp.589-601

50. K-.F. Nilsson, N. Taylor , P. Minnebo, Analysis of Fracture Tests on Large Bend Beams Containing an Embedded Flaw, submitted to International Journal of Pressure Vessels and Piping, December 2004
51. D. Lauerova (Nuclear Research Institute Řež plc), FE Post-Test Analysis Of Clad 4.2.1, Minutes of the 6th NESC-IV Progress Meeting, December 2002, NESCDOC MAN (03) 02 Annex 5,
52. D. Lauerova (Nuclear Research Institute Řež plc), FE Post-Test Analysis Of Clad 4.2.1, Minutes of the 7th NESC-IV Progress Meeting, Erlangen (Germany), May 2003, NESC DOC (03) 03 Annex 7.
53. M. C. Smith, Constraint-based R6 assessments of NESC-4 uniaxial beam tests, British Energy Generation Limited, March 2004
54. D W Beardsmore R6 Assessments of the NESC IV buried defect experiments with allowance for reduced constraint, Serco Assurance Report SA/EIG/18507400/R001, August 2003.
55. M. Ludwig & E. Keim, FANP GmbH Report, November 2003.
56. O'Dowd: Applications of two parameter approaches in elastic-plastic fracture mechanics, Engng. Fract. Mech. 52 (1995), p. 445
57. B.R. Bass et al, An Investigation of cladding Effects on Shallow-Flaw Fracture toughness of Reactor Pressure Vessel Steel under Prototypic Biaxial Loading, ASME J. Press. Vessel. Tech., Vol. 121, p. 257, 1999
58. B R Bass, W J McAfee, P T Williams, D P G Lidbury, E Keim and N Taylor, "Biaxial bend fracture tests on a forged ferritic steel", Vocalist and NESC-IV Test Report, 2002
59. M. Brumovsky, D. Lauerova, J. Palysa, Testing of Fracture Toughness under Biaxial Conditions, to be published Proc. 18th International Conference on Structural Mechanics in Reactor Technology (SMiRT 18), Beijing, China, August, 2005
60. A. Sherry, D.Hooton and D. Lidbury, Engineering Assessment Of Constraint Effects On Cleavage Fracture, Proc. ASME PVP 2004, San Diego, USA

European Commission

EUR 21846 EN – DG JRC – Institute for Energy

NESC-IV PROJECT An investigation of the transferability of Master Curve technology to shallow flaws in reactor pressure vessel applications

Authors:

N.G. Taylor

K.-F. Nilsson

P. Minnebo

B.R.Bass

W.J. McAfee

P.T. Williams

D.I. Swan

D. Siegele

Abstract

The NESC– IV project addressed the transferability of fracture toughness data from laboratory specimens to applications that assess the integrity of reactor pressure vessels subjected to upset and normal loading transients. The main focus was six biaxial bend cruciform tests of surface-breaking semi-elliptic defects in a reactor pressure vessel longitudinal weld and four uniaxial tests on extended sub-clad defects in adjacent plate material. The experimental/analytical program drew from major elements of the US Heavy Steel Technology Program. Extensive materials testing and fracture analyses were performed by 20 European organisations, coordinated by the Network for Evaluating Structural Components (NESC).

The mission of the Joint Research Centre is to provide customer-driven scientific and technical support for the conception, development, implementation and monitoring of EU policies. As a service of the European Commission, the JRC functions as a reference centre of science and technology for the Union. Close to the policy-making process, it serves the common interest of the Member States, while being independent of special interests, whether private or national.

EUROPEAN COMMISSION
DIRECTORATE-GENERAL
Joint Research Centre